Sensing Gamma-Rays in Thick Pixelated Thallium Bromide Detectors with Application-Specific Integrated Circuits

by

Erik Hall

A dissertation submitted in partial fulfillment
of the requirements for the degree of
Doctor of Philosophy
(Nuclear Engineering and Radiological Sciences)
in the University of Michigan
2024

Doctoral Committee:

Professor Zhong He, Chair
Professor Igor Jovanovic
Professor Zetian Mi
Doctor Michael Streicher

Erik Hall
erikhall@umich.edu
ORCID iD: 0000-0001-6873-6573

Dedication

To my wife Jessica, who has supported me every step of the way, so that we can build safer and more fulfilling lives for our children Mirae and Gavin. To my parents and grandparents, who raised me and inspired my curiosity as well as my duty to make life at least a little bit better for everyone else.

Acknowledgments

Any success I have encountered on this path is due in large part to Professor Zhong He. My background was very unconventional compared to most students in our department, so I cannot thank him enough for bringing me into the Orion Radiation Measurements Group and educating me to be a contributing member. In my previous occupation, we would compliment a person with vast experience by saying that he or she "has forgotten more about a topic than I have learned". Well, Professor He has learned so much about radiation detection that he has forgotten more about it than I have yet learned, so he has inspired me to continually work to learn more.

All the members of the Orion Group, past and present, have had some impact on my development, but I would like to especially thank Doctors Jiawei Xia, Sean O'Neal, Daniel Shy, Charles Leak, Matthew Petryk, and Yuefeng Zhu. They helped me build the foundation of my knowledge in this Group's expertise and advised me along the way. And they are a great group of colleagues to spend time with. Additionally, I would like to thank James Berry for all of his advice. His experience and wisdom filled in numerous educational gaps left by my undergraduate background and graduate courses.

Lastly, I would like to thank Doctors Jim Christian, Hadong Kim, Len Cirignano, and Kanai Shah of RMD, Inc. for teaching me while I worked with them on this project. Dr. Shah was a great inspiration for this work and he will be missed, may he rest in peace.

This work has been conducted under the auspices of the U.S. Department of Homeland Security, Countering Weapons of Mass Destruction Office, under competitively awarded contract 70RDND18C00000019. This support does not constitute an express or implied endorsement on the part of the US Government.

Table of Contents

List of Figures

List of Tables

List of Acronyms

ADC analog-to-digital conversion.

ASIC Application-Specific Integrated Circuit.

CZT cadmium zinc telluride.

EMI electromagnetic interference.

FPGA Field-Programmable Gate Array.

FWHM full-width-at-half-maximum.

FWTM full-width-at-tenth-maximum.

HPGe high-purity germanium.

IDEAS Integrated Detector Electronics AS.

RMD, Inc. Radiation Monitoring Devices, Inc..

RTSD room-temperature semiconductor detector.

UM University of Michigan.

Abstract

Pixelated semiconductor gamma-ray detectors are uniquely suited to perform both gamma-ray spectrometry and imaging with the same device. These detectors can precisely record the energy deposited by an incident gamma ray and their planar-pixel electrode configuration enables three-dimensional position-sensing of the interaction. CZT has demonstrated great commercial success and research materials such as TlBr and Perovskites, such as cesium-lead bromide, have potential as alternatives to CZT. However, readout electronics and algorithms that can mate with these new materials are key components to their radiation detection capability. This work seeks to identify the gaps in the fabrication of pixelated TlBr gamma-ray detectors, using current readout technology and techniques, and suggests areas for further development.

Electrodes made from various combinations of materials to include chromium, gold, palladium, and platinum provided the best spectroscopic performance. However, their performance generally worsened over time. Some samples showed a small improvement later, but not enough for their further use as gamma-ray detectors. Electrode refabrication failed to provide good results later, so electrode materials are likely diffusing into the detector bulk. Additionally, a small detector with thallium electrodes provided similarly good performance until failure, then was operated with a reverse-polarity positive bias for a similar time period. When tested again with a negative bias, it showed good performance again similar to its operation before failure.

In larger detectors bonded to a carrier board, over days of operation, some event waveform tails show an increasing amount of extra signal, which degrades spectroscopic resolution. Events occurring near the pixel edges tend to show this extra tail signal while event waveforms in the pixel center tend to have a more consistent shape. Increased electron de-trapping around the pixel edges is a possible cause. A pixel-like pattern has also been observed on their planar cathodes, where patches of the cathode have disintegrated. It is possible that the silver epoxy used to bond the pixelated anode of

the detectors to their carrier board is reacting with the planar cathode and causing the separation.

The VAD-UMv2.2 ASIC is failing to record many events at its smallest dynamic range. This problem is exacerbated for detectors with greater electron trapping. Failure to record events in sub-optimal detectors makes characterization difficult or impossible. Increasing the preamplifier feedback resistance enabled the recording of more events in the middle depths, but events near the planar cathode were still missing. When using the smallest dynamic range, this ASIC's trigger shaper likely has a time constant that is too short for slow-rising waveforms in lower-mobility materials like TlBr. However, this ASIC's second-smallest dynamic range seemed to be better able to record more bulk events, even near the planar cathode. Another disadvantage is that its sampling window at a 2.5 MHz sampling rate is barely long enough to fully record events in TlBr at more sustainable operating biases like 1 kV/cm. The slowest sampling rate of 1.25 MHz would be beneficial for recording complete event waveforms but was not functioning.

The H3DD-UMv4 ASIC is more suitable than the VAD-UMv2.2 ASIC for slower materials such as TlBr. It has more reliable slow sampling rates, a longer sampling window, and a wider span of trigger shaping times. It's slower trigger shaper time constant enables the recording of more low-amplitude events, which helps correctly categorize multi-pixel events and thus improves the energy resolution for single-pixel events.

One detector showed consistent performance when operated from 0°C to +30°C. However, and extra signal loss was observed repeatedly at +40°C. Faster preamplifier decay at +40°C played a role in that signal loss.

Chapter 1

Introduction

1.1 Wide Uses of Gamma-Ray Detectors

The underlying reason for this entire work is the measurement of radioactive decay. Many isotope decay schemes are well-known and characterized, especially those involving the emission of gamma rays.[1] Blood will flow with more volume through healthy heart tissue than damaged heart tissue, so when a radiotracer like technetium-99m-tetrofosmin is injected into a patient, measuring its decay can show where the patient's heart has impaired function.[2] The more precisely a radiotracer can be measured, the less of it has to be used, reducing the radiation dose to the patient. Comparing the ratio of characteristic gamma rays of uranium-238 and uranium-235 emitted from the decays in a uranium sample can reveal its enrichment level.[3] This enrichment level must be below certain limits to ensure confidence that a state is not attempting to proliferate components for nuclear weapons. Since gamma rays and X rays are almost always present in everyday items, spectroscopic portal monitors can measure their energy to determine the isotopic composition of cargo. This can help border officers more expediently decide whether to grant immediate entry to routine cargo or conduct further inspection on suspicious cargo.[4] The ability to detect and characterize gamma rays has many uses in keeping people healthy and safe.

1.2 Gamma-Ray Interactions

Gamma rays primarily interact with matter in three different ways: photoelectric absorption, Compton scattering, and pair production. Due to these different mechanisms, a detector may not always record the full energy of gamma rays emitted by an isotope. Understanding these interactions helps an observer interpret the energy spectrum that a detection system produces. The most probable interaction mechanism is dependent on the energy of the gamma ray and the atomic number of the interaction medium, as seen in Figure 1.1. The simplest interaction is photoelectric absorption because all of the incoming gamma-ray energy is absorbed into a detecting medium's atom, which subsequently ejects a photoelectron.

The second type of interaction is the Compton scatter. In this interaction, a gamma ray scatters off at an angle from its incident direction as well as recoils an electron in another direction. The scattering angle will depend on how much energy is transferred to the recoil electron. The greater the scattering angle, the greater the amount of energy was transferred. The electron will be collected by the detector and the scattered photon will either escape the detector or interact again. If this second interaction is fully captured through photoelectric absorption, the full energy of the gamma ray will still be recorded, despite the longer chain of interactions.

The third type of interaction is pair production. Gamma rays must have at least 1.022 MeV to interact this way, due to the conservation of energy. This is because they must have enough energy to create an electron-positron pair, where each particle has 0.511 MeV of mass energy. The electron will be collected like those in the previous interactions. The positron will annihilate with another electron and create a pair of annihilation photons, each with an energy of 0.511 MeV. Those photons may then interact with the detector in one of the ways previously mentioned, if they don't escape the detector.

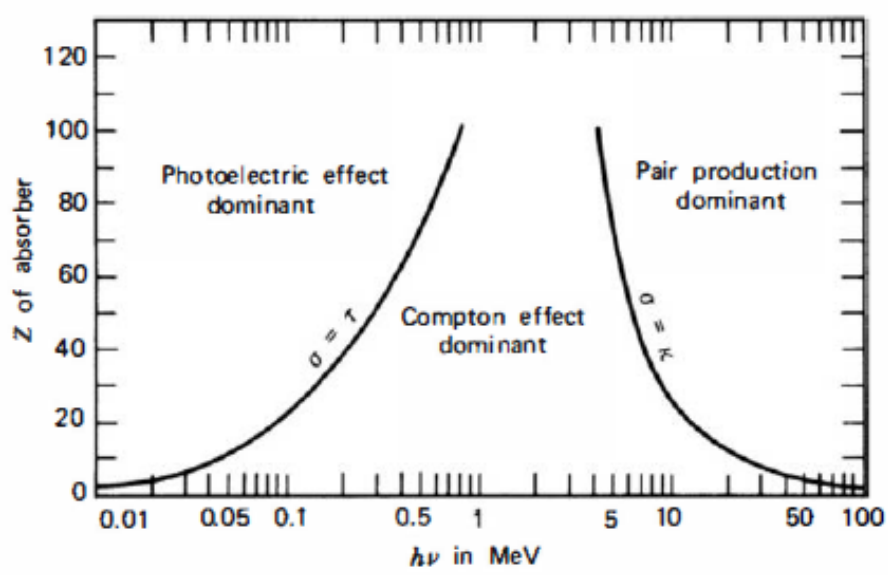

Figure 1.1: Dominant gamma-ray interaction mechanism for atomic number and gamma-ray energy.[5]

1.2.1 Characteristic X Rays

When an atom photoelectrically absorbs an incoming photon, it also emits an X ray equal to the binding energy of the recoil electron. If this interaction occurs near the edge of a detector, this characteristic X ray may escape the detector and subtract their binding energy from the recorded energy of the incoming photon. For thallium, K-shell transition energies range from 70 to 85 keV, so its characteristic x-ray escape peak will appear in an energy spectrum in energy bins 70 to 85 keV below the photopeak. Since there is a range of transition energies, this escape peak will have a poorer resolution than the photopeak, which is based on monoenergetic photons. In larger detectors, edge voxels will have a more prominent characteristic x-ray escape peak than inner voxels since edge voxels give the X rays a greater chance to escape the detector.[6]

1.3 Semiconductor Radiation Detectors

There is a wide selection of semiconductor radiation detectors that have existed in the past and present, but the following four will be highlighted for context: high purity germanium, cadmium zinc telluride, thallium bromide, and cesium lead bromide.

1.3.1 High-Purity Germanium

High-purity germanium is considered the "gold standard" in gamma-ray spectroscopy. It has been able to achieve an excellent energy resolution approaching 0.2% full-width-at-half-maximum (FWHM) at 662 keV.[7] This resolution means that it should provide the ability to resolve two photopeaks that are separated by at least 1.3 keV. These detectors are typically manufactured in a planar or coaxial configuration, as seen in Figure 1.2.[8] Germanium's atomic number is 32, and its density is 5.33 grams per cubic centimeter (g/cm^3), which are lower than the other detector materials discussed in this chapter. These attributes give high-purity germanium (HPGe) a lower "stopping power" for gamma rays than other materials with a higher atomic number and density. Despite these potential drawbacks, HPGe's primary strengths are its relatively large detection volume and its extremely good energy resolution, so it is the primary choice for gamma-ray spectroscopy.

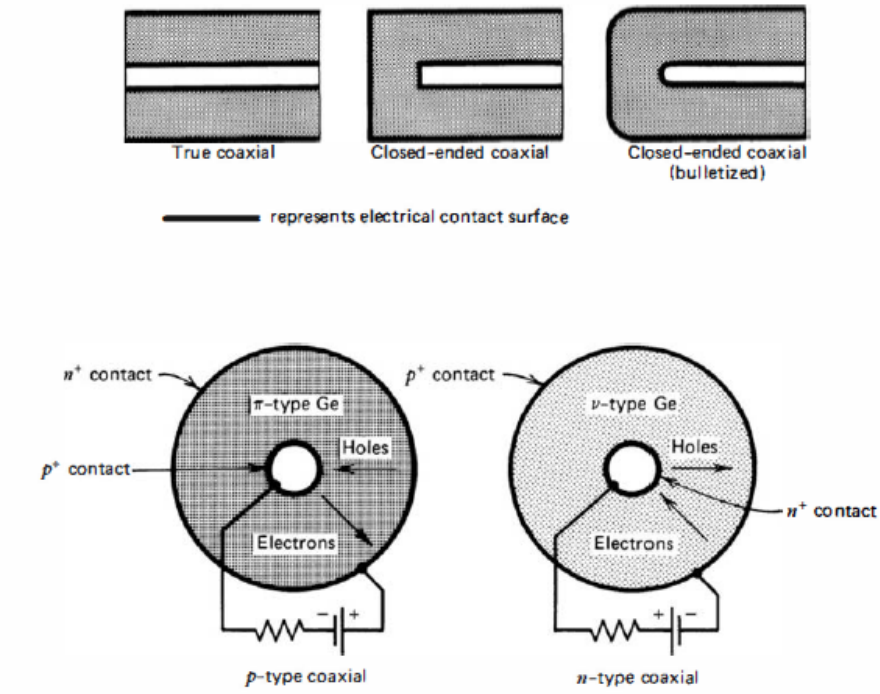

Figure 1.2: Example of HPGe in a coaxial geometry. Reprinted from Ref. [8]

HPGe's primary drawback is that it requires cryogenic cooling to be an effective gamma-ray spectrometer. This limitation is due to its smaller bandgap of 0.72 eV.[9]

This smaller bandgap necessitates cryogenic cooling to prevent valence electrons from being thermally excited to the conduction band. With thermally excited electrons suppressed, electrons excited from gamma-ray interactions become observable. This cooling requirement makes it significantly more difficult for HPGe to be used as part of a portable or quickly-deployable detection system.

HPGe's strength comes from its low ionization energy, also known as W-value, which is how much deposited energy is needed to generate an electron-hole pair. HPGe needs 2.98 eV per electron-hole pair.[9] The lower W-value means that HPGe creates more electron-hole pairs for a photon with a given energy, which reduces the influence of Poisson statistics on the measured energy. HPGe also has relatively high carrier mobility for both electrons and holes. Its electron mobility is 3.6×10^4 $cm^2/(V\cdot s)$ and its hole mobility is 4.2×10^4 $cm^2/(V\cdot s)$.[9] Due to the similar mobility and long lifetime of both charge carriers, the motion of both carriers in HPGe is used to measure interaction energy, unlike the other wide bandgap semiconductors discussed in this chapter.

1.3.2 Cadmium Zinc Telluride

Cadmium zinc telluride is a commonly-used room-temperature semiconductor detector (RTSD). In commercial applications, cadmium zinc telluride (CZT) can achieve an energy resolution better than 1% FWHM at 662 keV[10], and in laboratory settings, can achieve close to 0.3% FWHM at 662 keV, using only single-pixel events.[11] CZT's effective atomic number is 50, assuming a 90%-10% ratio of Cd-Zn, and its density is 6 g/cm^3. The higher effective atomic number and density will give photons a higher probability of interacting within a given volume than HPGe. CZT has a bandgap of 1.6 eV.[12] Because this value is more than double the value of HPGe, CZT is better able to keep thermally excited electrons from entering the conduction band. This enables CZT to measure photon interactions at room temperature without cryogenic cooling. CZT has a melting point over 1000°C, so it generally costs more to manufacture than other materials with a lower melting point.[13] Special techniques must be applied to ensure that tellurium does not concentrate into inclusions during crystallization.[14] CZT's W-value is 5 eV per electron-hole pair, which is greater than HPGe but still more than adequate to achieve better than 1% FWHM energy resolution at 662 keV.[12]

However, CZT has dissimilar mobility between charge carriers: about 1350 $cm^2/(V\cdot s)$

for electrons and about 120 $cm^2/(V \cdot s)$ for holes.[12]. A smaller hole mobility-lifetime product relative to electrons means that holes will be subjected to more trapping in the detector than electrons.[15] At a fast enough sampling rate, the entire movement of the electron cloud through the detector bulk may be captured while the hole cloud will have no perceptible motion. This necessitates the use of other signal processing techniques such as "single-polarity charge-sensing" readout and more complex electrode configurations, such as coplanar, hemispherical, or pixelated. These changes also enable a better energy resolution that was not achievable with a planar configuration.

1.3.3 Thallium Bromide

Thallium bromide is an experimental RTSD. At 662 keV, it has achieved sub-1% FWHM resolution when cooled to -18°C and 1.8% FWHM resolution at room temperature.[16], [17] TlBr has an effective atomic number of 72, based on molar fraction, and its density is 7.56 g/cm^3, which is greater than CZT and good for gamma-ray detection. It has a bandgap of 2.68 eV, which is 63% greater than CZT and should enable TlBr to continue operating at higher ambient temperatures.[18] TlBr's W-value is 6.5 eV per electron-hole pair, which is greater than CZT but still adequate for sub-1% FWHM energy resolution at 662 keV.[19] Its mean free path, calculated from NIST's elemental mass attenuation coefficients, at various energies is shown in Table 1.1.[20] Another advantage is its lower melting point of 480 °C, which, when coupled with its simpler chemical formula and structure, enables its manufacturing through horizontal zone refinement.[21]

Photon Energy [keV]	59.5	187	250	511	662	1173	1333	2614
CZT (90/10 Cd/Zn) [cm]	0.023	0.37	0.58	1.43	1.70	2.42	2.60	3.36
TlBr [cm]	0.031	0.14	0.25	0.99	1.32	2.23	2.44	3.16

Table 1.1: Photon mean free path at various energies for any interaction method.

TlBr has lower carrier mobility than CZT, around 20-40 $cm^2/(V \cdot s)$ for electrons and around 1-12 $cm^2/(V \cdot s)$ for holes.[22], [23] Electron mobility-lifetime products are around 10^{-3} while hole mobility-lifetime products are around 10^{-4} to 10^{-6}.[16] This difference also requires TlBr to be operated as a "single-polarity charge-sensing" detector. However, the lower charge carrier mobility requires readout electronics, particularly those

designed primarily for CZT, to accommodate this slower charge drift.

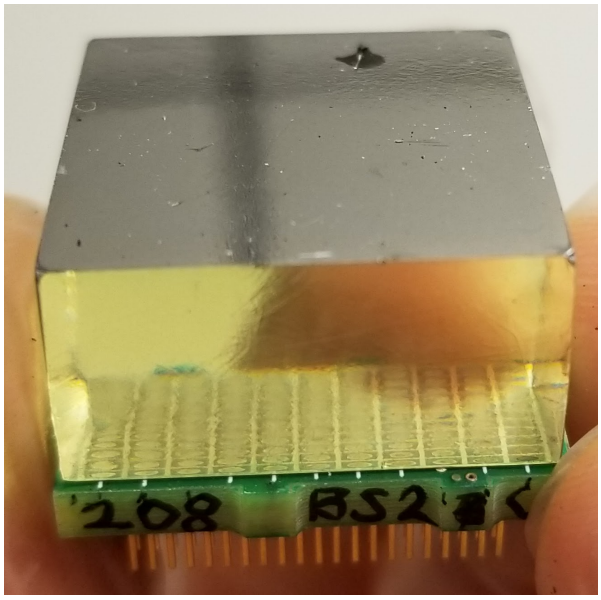

Figure 1.3: TlBr Detector 208BS2(R) with an 11×11-pixel array electrode.

For Radiation Monitoring Devices, Inc. (RMD, Inc.)'s detector naming convention, the first number is the ingot number from which the detector was made.[24] The next one or two letters "A" through "D" describe the one quarter section, or two neighboring quarter sections, from which the detector was made. Section "A" is at the "seed" end and section "D" is at the tail end. The letter "S" describes the orientation of the crystal relative to the center axis of the ingot, i.e. "S" is a slice that is perpendicular to the axis of the ingot. All detectors used in this work were cut in this manner, so that the surfaces with the electrodes were perpendicular to the ingot center axis, or growth direction. The next one or two digits reference the number of detectors from that quarter section. If there is an "R" in parentheses at the end, the number of "R"s describes how many times the electrodes have been refabricated.

1.3.4 Perovskites

Perovskites (any material with a crystal structure of ABX_3), such as $CsPbBr_3$, have been gaining interest as a photovoltaic cell and now as a gamma-ray detector.[25], [26] In a laboratory setting, $CsPbBr_3$ has achieved 1.4% FWHM resolution at 662 keV at

room temperature.[27] Its effective atomic number is 56, it has a density of 4.86 g/cm^3, and it has a bandgap of 2.25 eV; which make it suitable for gamma-ray detection.[28]

μ_e [cm^2/(V·s)]	$(\mu\tau)_e$ [cm^2/V]	μ_h [cm^2/(V·s)]	$(\mu\tau)_h$ [cm^2/V]
63	4.5×10^{-4}	49	9.5×10^{-4}

Table 1.2: $CsPbBr_3$ charge carrier characteristics [29]

Since the carrier mobilities are similar, event signals could simultaneously record the movement of both carriers. This could make single-polarity charge-sensing more difficult as each carrier's signal would have to be separated with a shaper. Other Perovskite formulations may have different carrier mobilities. However, the larger in the $(\mu\tau)_h$ product mean that holes can be the primary information carrier. A potential advantage of this material is that it is possible to grow crystals in solution at a lower temperature than traveling heater method or horizontal zone refinement. Since growth cost correlates with melting temperature, this could reduce crystal growth cost.[30] However, achieving good performance as a radiation detector will require further research.[31]

1.4 Contributions of This Work

This is the first work to use a waveform-sampling digital Application-Specific Integrated Circuit (ASIC) to read out radiation interaction signals of gamma rays in thallium bromide detectors with 11 × 11 large-pixel arrays at room temperature. TlBr has been known as a potential radiation detector since 1947.[32] It has been explored more deeply as such in the last 40 years.[33] Takagi et al. designed and employed a photon-counting analog integrated circuit with TlBr as a flat-panel X-ray imager.[34] Vernon et al. designed an analog ASIC that could measure the event timing and amplitude from CZT, but included circuitry for slower materials like TlBr.[35] However, this is the first work to use the unique technology of waveform-sampling digital ASICs to reduce electronic noise and save whole event waveforms from TlBr. Two digital ASICs will be discussed: one designed by Integrated Detector Electronics AS (IDEAS) and another designed by Doctor Gianluigi De Geronimo.[36], [37]

Chapter 2

Theory

2.1 Shockley-Ramo Theorem

The Shockley-Ramo theorem explains how the induced charge on an electrode due to the drift through an electric field of a charge from an ionizing radiation interaction in a medium can be calculated. Before this theorem, the induced charge had to be calculated by a series of integrations from multiple points along the charge's drift path through the electric field between two electrodes, as shown in Eq. 2.1, where ε is the dielectric constant of the detector medium, $\overrightarrow{E}$ is the electric field at a specific point, and S is the surface of the electrode. Additionally, the operating electric field $\overrightarrow{E}$ depends on the space charge distribution in the medium, which is usually not possible to know or determine.

$$Q = \oint_S \varepsilon \overrightarrow{E} \cdot dS \tag{2.1}$$

However, if one electrode is selected to have a unit potential of one and all the other electrodes are set to a potential of zero, the induced charge Q can be calculated with Eq. 2.2. In Eq. 2.2, q is the charge of the carrier particles and $\Delta\phi_0$ is the change in weighting potential from the interaction position to the collection position.[38]

$$Q = -q \cdot \Delta\phi_0 \tag{2.2}$$

A planar detector will be used as an example to apply the Theorem. Fig 2.1a shows a planar detector with the cathode at ground and a positive bias applied to the anode.

The dot in the middle represents the interaction of an incoming gamma ray. From that point, the holes move towards the cathode and the electrons move towards the positively biased anode. Fig 2.1b shows how each carrier will contribute to the collected signal. As each carrier travels towards their respective electrode, they induce a signal corresponding to their traversed portion of the weighting potential profile. In other words, as the electrons travel towards the anode, they will induce a signal proportional to the change of the weighting potential from Z to 1. The holes will induce signal proportional to difference of the weighting potential from Z to 0. If incoming gamma rays are monoenergetic and the charge trapping is negligible, the charge carriers together will induce the same amount of signal, independent of the depth of interaction. This is how an HPGe detector works.

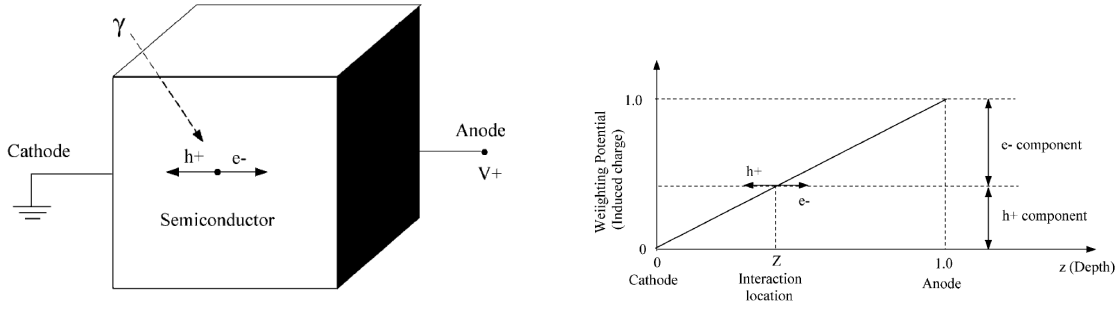

(a) Physical configuration. **(b) Weighting potential profile.**

Figure 2.1: Example of a planar detector. Reprinted from Ref. [38]

A pixelated detector with a planar electrode at depth 0 and a pixelated electrode at depth T is shown in Fig. 2.2a. Assuming the same bias configuration as Fig. 2.1a, holes will move towards the planar cathode and electrons will move towards the pixelated anode. The "collecting pixel" is the pixel at the end of the electric field lines from the point of interaction. In Fig. 2.2a, interaction C's collecting pixel is Pixel #2, while interaction A and B's collecting pixel is Pixel #1. All other pixels are "non-collecting pixels". In accordance with Fig. 2.2b, charge carriers will induce a signal on the pixel along the solid curved line. Simultaneously, they also induce a signal on the planar cathode along a straight-line weighting potential profile from (0,1) to (T,0). Just like in the planar example, as the electrons travel towards the pixelated anode, they will induce a signal proportional to the difference of the weighting potential from the interaction depth to depth T, and the holes will induce a signal proportional to

the change of the weighting potential of the distance traveled from interaction depth toward depth 0. Assuming that incoming gamma rays are monoenergetic and the hole mobility is much lower than the electron mobility, electrons will induce a similar signal that is nearly depth-independent at depths from 0 to about 0.7T on the pixel and a signal proportional to the depth of interaction on the planar cathode. The region from about 0.7T to T is considered the "near-pixel region", and the pixel signal will be very dependent on the depth of interaction in this region. This is how pixelated CZT and TlBr detectors work.

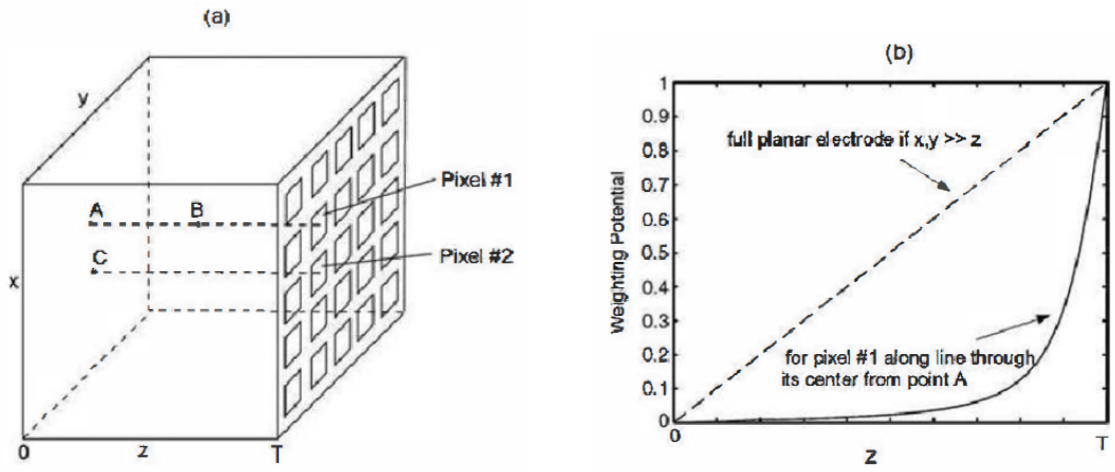

(a) Physical configuration. **(b) Weighting potential profile.**

Figure 2.2: Example of a pixelated detector. Reprinted from Ref. [8]

It is also beneficial to maximize the detector thickness relative to the pixel size. As the thickness is maximized, the pixel weighting potential becomes flatter through most of the depth and steeper in the "near-pixel" region, as seen in Fig. 2.3. This greatly reduces the dependence of pixel signal amplitude on the depth of interaction, which will enable processing techniques discussed in later chapters.

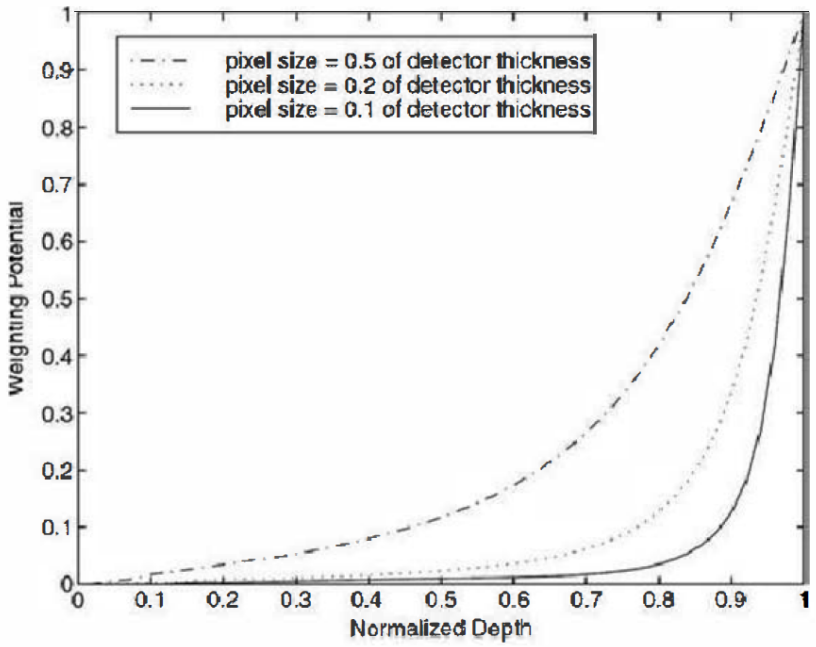

Figure 2.3: Weighting potential profiles for three different pixel sizes relative to detector thickness. Reprinted from Ref. [8].

2.2 Carrier Drift Parameters

2.2.1 Carrier Mobility

Carrier mobility μ is a measure of how quickly a charge carrier moves through a medium. It is the quotient of the carrier velocity and the electric field that it is traversing. This relationship is seen in Eq. 2.3. Carrier mobility units are typically in $\mathrm{cm}^2/(\mathrm{V{\cdot}s})$, carrier velocity v is in cm/s, and electric field E is in V/cm.

$$\mu = \frac{v}{E} \tag{2.3}$$

2.2.2 Carrier Lifetime

Carrier lifetime τ is a measure of the average time that charge carrier can move through a medium before it is trapped. The number of carriers moving through an electric field in a medium decreases along an exponential decay curve, assuming there is uniform

trapping throughout the medium. The Hecht relation is a well-known description of induced charge as a function of the interaction depth and the decrease in the number of carriers, as seen in Eq. 2.4.[8], [39], [40] Q is the induced charge on an electrode, q_0 is the initial charge generated by the radiation interaction, τ is the mean free drift time of the charge carrier, and t is the carrier drift time.

$$Q = Q_0 \frac{\tau}{t}(1 - exp(-\frac{t}{\tau})) \tag{2.4}$$

2.2.3 Mobility-Lifetime Product

The mobility-lifetime product is normally used to evaluate a sample's worthiness as a detector. The product must be sufficiently high enough so that the carriers can move far enough through the detector to contribute to the electrical current read out before those carriers can get trapped in the detector. In the typical detector sizes and operating biases used in this work, 10^{-3} to 10^{-2} is the minimum mobility-lifetime product observed for effective semiconductor detectors. When one carrier's product is much greater than the other carrier, that detector is well-suited for using "single-polarity charge sensing" techniques.

Chapter 3

Detector Readout Systems

3.1 Discrete Channel System

The following system, as seen in Fig. 3.1 was used to test wire-bonded detectors with an electrode that consisted of a 3×3-pixel array or less. A detector mounted on its carrier board was mounted on the readout board inside the readout box. The aluminum readout box served as a light-tight Faraday enclosure. A direct-current power supply (DCPS) provided power to the charge-sensitive preamplifiers. A high-voltage power supply (HVPS) provided the operating bias on the planar cathode. Signals from each pixel anode and the planar cathode were amplified and sent out on dedicated channels to the digitizer inputs. The data acquisition computer (DAQ CPU) saved the event waveforms for later processing.

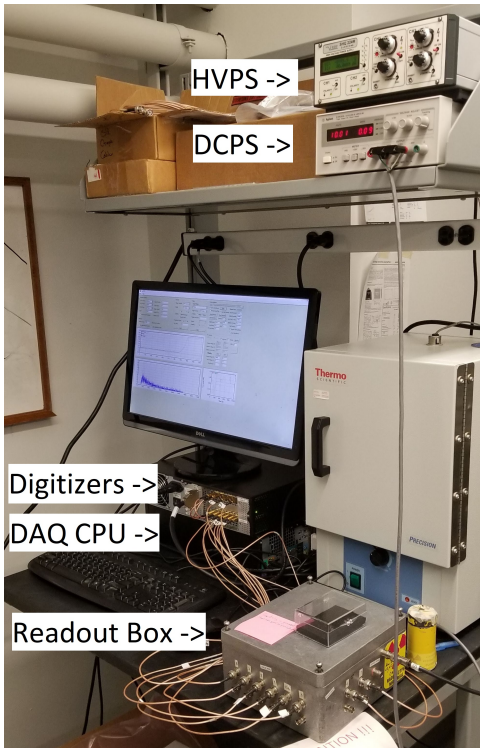

Figure 3.1: Discrete Channel System Setup

3.1.1 Charge-Sensitive Preamplifiers

The charge-sensitive preamplifiers were the Kromek eV-5093R2. They were mounted on a printed circuit readout board inside an aluminum box. Each pixel anode was either directly-coupled or capacitively-coupled, depending on the selected readout box, to a dedicated preamplifier. The planar cathode was also capacitively-coupled to a dedicated preamplifier. This particular model was selected because of its relatively long fixed fall time of over 1 millisecond, which gave event waveforms a relatively flat tail, and its high gain of 3.6 mV/fC, which amplifies interaction signals above electronic noise. It also has a low equivalent noise charge of around 166 e_0 FWHM in silicon with zero input capacitance.[41] The output channels were connected to the digitizer input channels.

3.1.2 PCI-based Digitizers

PCI-based digitizers manufactured by GaGe Applied Technologies were used to digitize event waveforms. The model was the Octopus CompuScope 8389 or 8349, and they were mounted on either a computer motherboard or in a PCI expansion box connected to a data acquisition computer. For TlBr, these 14-bit digitizers allowed measurements with a sampling window typically set between 128 and 1024 samples and a sampling rate typically set between 1 and 10 MHz.

3.2 Application-Specific Integrated Circuits

These systems were used to test flip-chip bonded samples, usually with a 6×6-pixel array or larger.

3.2.1 IDEAS VAD-UMv2.2

This ASIC, as seen in Fig. 3.2, was developed in a collaboration between IDEAS in Oslo, Norway, and the Orion Radiation Measurements Group at the University of Michigan.[36] Discrete digitizers work adequately for small samples, but larger samples that may have 36 or more pixels benefit from the reduced electronic noise of the compact architecture of an ASIC. This particular ASIC was designed primarily for use with CZT but also with some flexibility for other pixelated and coplanar-grid semiconductors. It has 130 inputs to charge-sensitive preamplifiers: 128 inputs for pixel electrodes and a guard ring electrode and 2 inputs for a planar electrode. Each input channel is continuously read out by a preamplifier with a user-programmable feedback component. This feedback component adjusts the waveform signal decay time, which should be long compared to the sampling pipeline so that waveform tails appear relatively flat to the user. Each preamplifier's output is sent to both a 160-cell (capacitor) pipeline and a shaping amplifier. The shaping amplifier's time constant is user-programmable between 400 to 500 nanoseconds. If the shaping amplifier's output exceeds the user-programmed threshold in the comparator, the pipeline will be read out with a user-programmed number of samples from before and after the moment of the trigger. This readout is the "event waveform." The sampling rate is designed to be user-programmable between 1.25 and 80 MHz. With TlBr, 2.5 MHz was typically used.

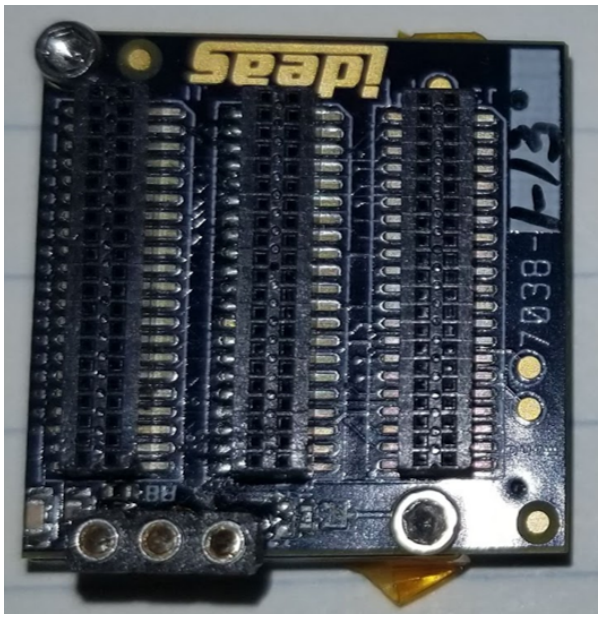

Figure 3.2: IDEAS VAD-UMv2.2 ASIC, top-down view

3.2.2 H3DD-UMv4

This ASIC was developed entirely within the Orion Radiation Measurements Group.[37] It has a similar physical configuration and capabilities to the VAD-UMv2.2, so it accepts many of the same detectors that are used with the VAD-UMv2.2 ASIC. However, it has two key advantages in the sampling pipeline and sampling rate. The pipeline can be configured up to 256 samples, which is 60% longer than the VAD-UMv2.2. The ASIC is also more reliable at slower sampling rates of 1.5625 and 3.125 MHz, which were used with TlBr. This ASIC's preamplifiers have a fixed decay time of around 8.7-9.1 μs, which can be deconvolved from waveforms before further data processing.

Chapter 4

Procedures

Previous ASICs used in this field were composed of analog circuitry that could only give the user event timing and signal amplitude.[42] The user could not see or save the waveforms for later analysis or processing. Event waveforms contain more information than just amplitude and timing. Digitizers, such as those shown in Chapter 3, can read out interaction event waveforms that will be processed later with user-defined algorithms to extract additional information.

4.1 Event Energy

4.1.1 Simple Subtraction

As the name implies, this technique is a simple way to extract the amplitude of the waveform. The "baseline" of a waveform is the mean of a set range of samples at the beginning of the waveform, where typically only some electronic noise is observed if the preamplifier is fully decayed. After the electron cloud has reached the anode, it will no longer induce any more signal on any electrode. This plateau of the signal is the "tail" of the waveform. These waveforms are depicted in Fig. 4.1. The tail value is also the mean of a set range of samples, but at or near the end of the event waveform. To calculate the amplitude, the baseline value is simply subtracted from the tail value. A drawback of this method is that the tail mean is usually calculated at the end of the waveform, long after electron cloud movement has ended. It there is significant signal decay, this gap between the end of electron cloud movement and the waveform tail causes a reduced

amplitude to be recorded for that event.

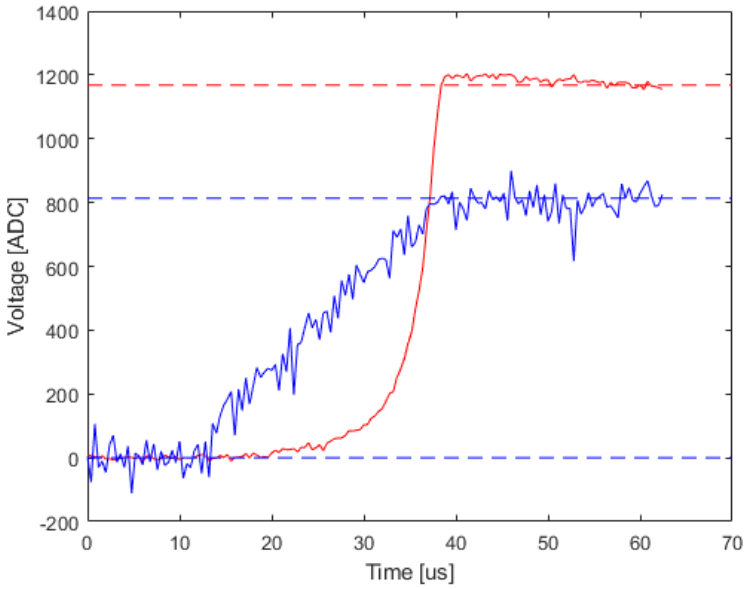

Figure 4.1: Event waveform with simple subtraction pickoffs. Red is the pixel waveform. Blue is the planar cathode waveform.

4.1.2 Trapezoidal Filtering

If anything causes the waveform tail to have a shape other than horizontal and flat, it could degrade the waveform amplitude calculated by simple subtraction. Trapezoidal filtering can solve this by calculating the amplitude closer to the moment of electron cloud collection. A simple trapezoidal waveform is set with flattop and rise/fall times based on expected event waveforms.[43] The flattop time should be at least as long as the event waveform takes to rise from baseline to full electron collection. Otherwise, the resulting waveform will not reach full amplitude. The rise and fall times, which are the same because of the trapezoidal shape, should generally be short, around 5-10% of the event waveform length. If the rise/fall time is longer than that, it will push the flattop later in time and potentially include extra signal rise or decay, which could degrade the extracted amplitude. The simple trapezoidal waveform is convolved with each event waveform and the maximum of the resulting convolved waveform is the extracted amplitude of the event waveform, as seen in Fig. 4.2. This is my primary

method for waveform amplitude calculation in this research, unless otherwise specified.

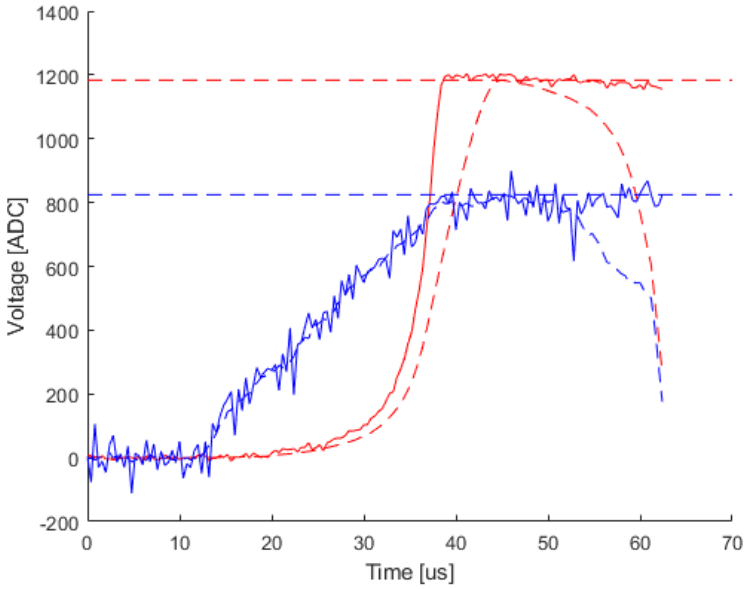

Figure 4.2: Event waveform with trapezoidal filtering pickoffs. Red is the pixel waveform. Blue is the planar cathode waveform.

4.2 Event Depth

4.2.1 Cathode-to-Anode Ratio

This method has been extensively used as an analog of the depth of interaction in pixelated detectors.[44] Because of the Shockley-Ramo theorem covered in Chapter 2, pixel waveform amplitudes are largely independent of depth of interaction, while planar cathode waveform amplitudes are depth-dependent. Therefore, the ratio of the absolute values of the planar cathode amplitude to the pixel anode amplitude will give the depth of interaction, although some precision is lost for events inside the near-pixel depths. At near-pixel depths, pixel waveform amplitudes also become depth-dependent, so the ratio becomes less analogous to interaction depth. The ratio values toward zero will be near the pixelated anode, while the ratio values toward one will be near the planar cathode, as seen in Fig. 4.3. There may be events with ratios over one; those events are typically a "charge-sharing" event. If an event loses some of the charge cloud to

the guard ring or another pixel, then the collecting pixel amplitude will be reduced. However, the planar cathode signal will be unaffected and collect the full amplitude. In addition, if there is inconsistency in the recorded amplitude of the event waveforms, it will affect the accuracy of this depth-reconstruction method.

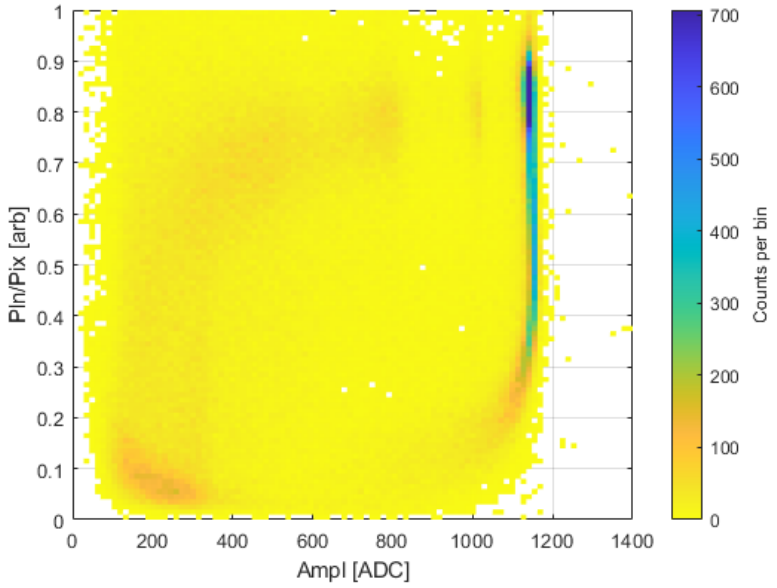

Figure 4.3: Depth using cathode-to-anode (planar-to-pixel) ratio versus pixel waveform amplitude for an inner pixel of TlBr Detector 212AS2(R). The source was Cs-137 so the vertical blue band around 1150 ADC is the 662 keV photopeak across the depth of the detector.

4.2.2 Carrier Drift Duration

Another method to find the depth of interaction is with carrier drift duration through CR-RC^4 filtering. The starting time of an event can be found from the planar cathode waveform, and the stop time of an event can be found from the pixel waveform.[42] The timing pick-off occurs when the filtered waveform signal first reaches 50% of the filtered waveform's maximum. This 50% method is known as the "constant fraction" technique. Fig. 4.4 shows that this method accurately picks off the event's stop time from the pixel waveform, but the start time from the planar cathode waveform is a bit late. With this method, pick-offs will generally be uniformly late, so this can be adjusted later if necessary by calibrating the lowest drift duration values to zero. This

is the primary method of event depth calculation unless otherwise specified because this depth-reconstruction method was much less sensitive to a varying amount of extra signal in the event waveform tail, which will be discussed later.

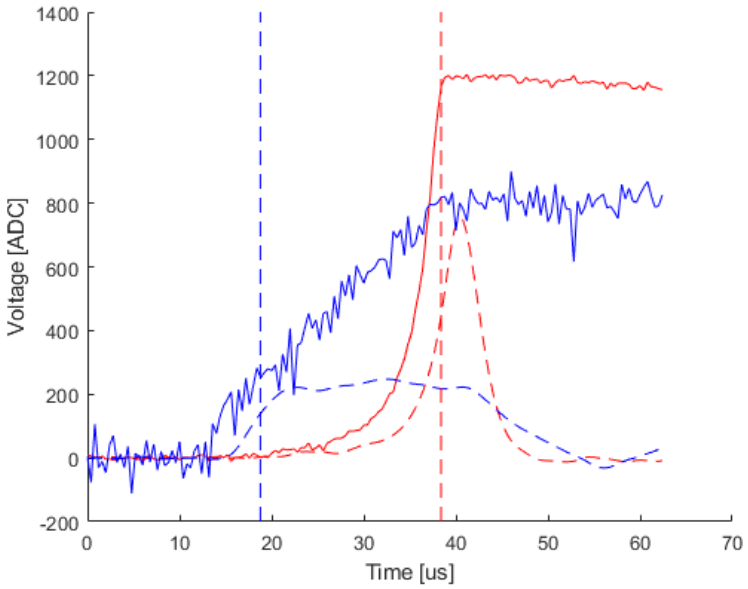

Figure 4.4: Event waveform with CR-RC^4 filtering pickoffs. Solid red is the pixel waveform. The dashed red waveform is the shaped pixel waveform and the vertical dashed red line is the stop time pick-off. Solid blue is the planar cathode waveform. The dashed blue waveform is the shaped planar waveform and the vertical dashed blue line is the start time pick-off.

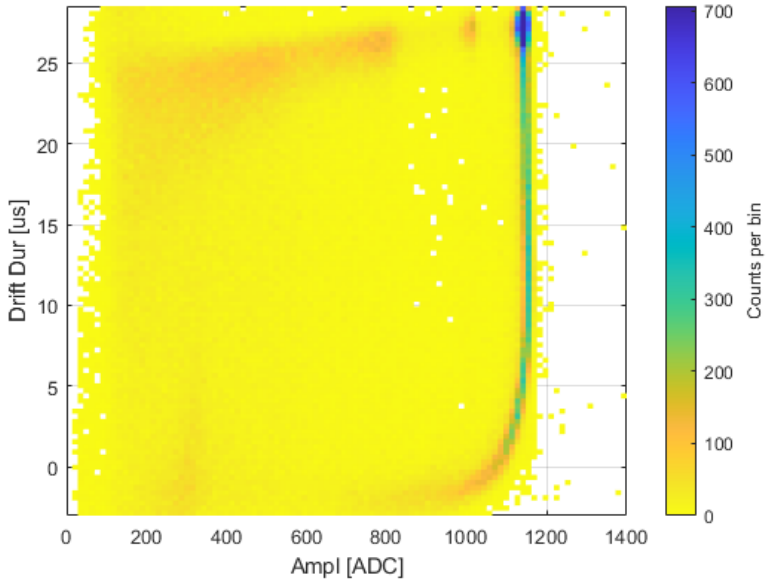

Figure 4.5: Depth using drift duration versus pixel waveform amplitude for an inner pixel of TlBr Detector 212AS2(R). High drift duration corresponds with planar cathode-side events while low or negative duration corresponds with pixel anode-side events. The source was Cs-137 so the vertical blue band around 1150 ADC is the 662 keV photopeak across the depth of the detector.

4.3 Depth Correction

Depth correction can improve the resolution of an energy spectrum, especially if event signal amplitude varies with depth in a detector. Fig. 4.5 shows a Cs-137 photopeak at nearly all depths. However, while the centroid of this photopeak might appear consistent at near-cathode depths, the photopeak centroid shifts downward in analog-to-digital conversion (ADC) voltage at depths towards the anode. Other detectors with significant trapping will have a photopeak centroid that shifts through the depth of the detector. Additionally, there is gain inconsistency from pixel to pixel due to the material and the ASIC preamplifiers. Any of these factors will cause broadening in the photopeak of the raw spectrum, which results in an energy resolution of 11% FWHM, as seen in Fig. 4.6a. Since the source's gamma-ray energy is known, all event energies at discrete depths can be calibrated from ADC voltage to keV. This sharpens the photopeak and results in a

better energy resolution of 2% FWHM, as seen in Fig. 4.6b.

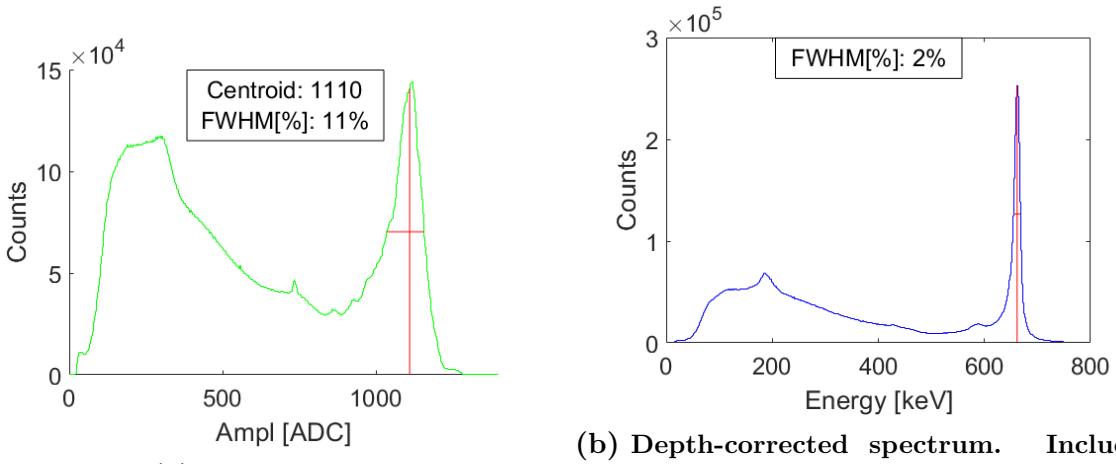

(a) Raw spectrum

(b) Depth-corrected spectrum. Includes by-pixel gain correction.

Figure 4.6: Depth correction of all single-pixel events in TlBr Detector 212AS2(R) with a Cs-137 source.

4.4 Subpixel Position

This technique determines where an event occurred laterally within a pixel column. At least four neighbor waveforms, also known as transient signals, are typically needed for the calculation, in reference to the collecting pixel: top, bottom, left, and right. With the amplitudes of these neighbor waveforms, the "opposing-neighboring ratio" method is used to calculate the position of the event within the pixel.[45] Similar methods also exist with all eight neighbor waveforms or other combinations of neighbor waveforms for edge and corner pixels with fewer than eight neighboring pixels. This method is based on the principle that an event will induce more signal on a certain neighbor if it occurs closer to that neighbor than the other neighbors, as seen in Fig. 4.7.

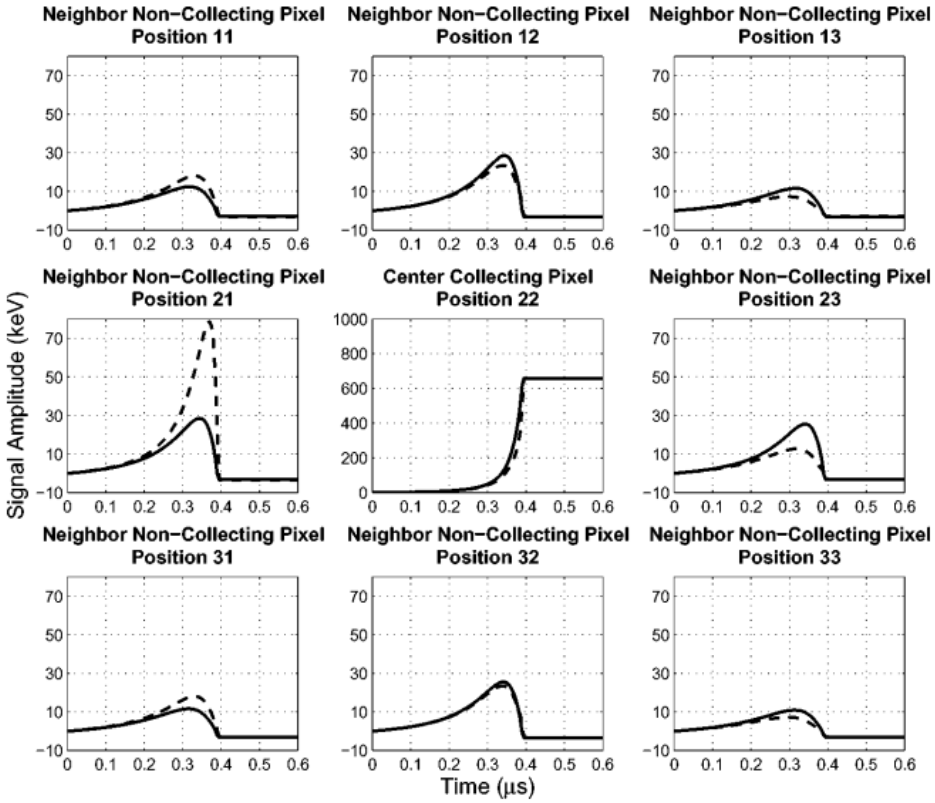

Figure 4.7: Simulated signals from a collecting pixel and its eight neighbors. Solid waveforms represent an interaction at the center of Pixel 22. Dashed waveforms represent an interaction in Pixel 22 that was closer to Pixel 21 than Pixel 23. Reprinted from Ref. [45]

The event shown in Fig. 4.8a will be used as an example. The time samples for the waveform maximums and minimums must be identified for each event. A rough amplitude was calculated for each waveform by tail-correcting it to the x-axis and summing the area underneath the waveform, as seen in Fig. 4.8b. The rough amplitudes were used to identify the two neighbor waveforms with the largest amplitudes, which in this example are the "x-1" and "y-1" neighbors, relative to the collecting pixel.

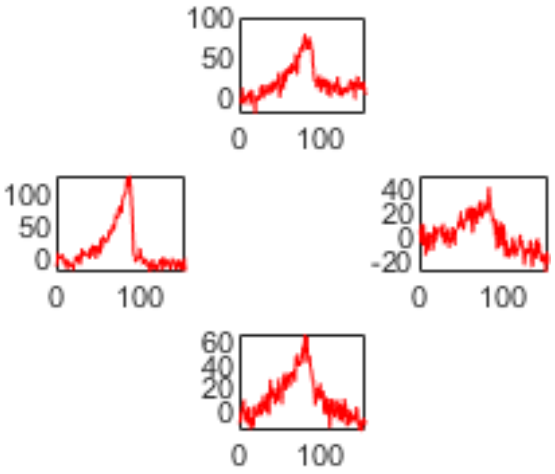

(a) **Four-neighbor pixel layout**

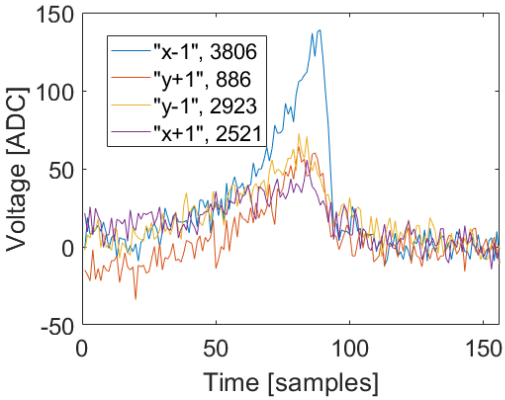

(b) **Together with tail-correction. Rough amplitudes in the legend.**

Figure 4.8: Four neighbor pixel waveforms from an event in an inner pixel in TlBr Detector 212AB1. X-axes are time in samples. Y-axes are voltage in ADC.

These two waveforms, without tail-correction, were summed and shaped with a digital 800 ns CR-RC^4 filter. The time samples at signal maximum and at signal mimum wered identified from this summed and shaped waveform, as seen in Fig. 4.9a, and were used with all neighbor waveforms of this event. Then each neighbor waveform is shaped individually with the same filter. Each neighbor's shaped waveform amplitude was the amplitude between the event's identified maximum and minimum time samples, as seen in Fig. 4.9b.

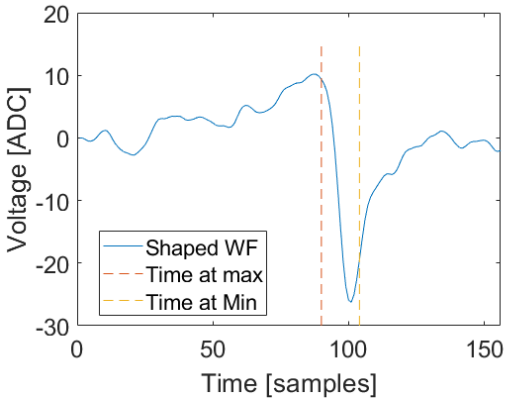

(a) Two highest-amplitude neighbor waveforms summed and shaped, with the time samples at maximum and minimum marked.

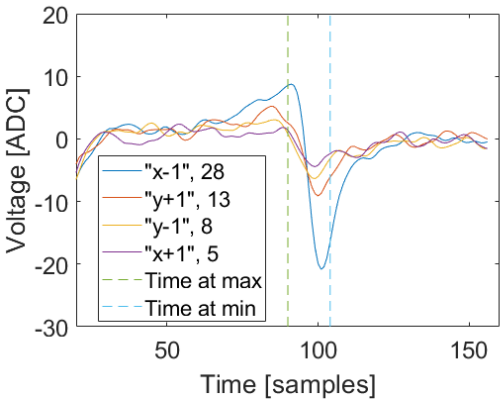

(b) All neighbor waveforms shaped individually. Calculated amplitudes in the legend.

Figure 4.9: Sub-pixel position processing technique example with TlBr Detector 212AB1.

With the amplitudes of each neighbor waveform, the x-axis sub-pixel position is calculated with Eq. 4.1, where R_x is the relative position of the event within the pixel from [-1,1], a_{top} is the amplitude of the top pixel's waveform, and a_{bottom} is the amplitude of the bottom pixel's waveform. Similarly, the y-axis sub-pixel position is calculated with Eq. 4.2, where R_y is the relative position of the event from [-1,1], a_{right} is the amplitude of the right pixel's waveform, and a_{left} is the amplitude of the left pixel's waveform. A position of [0,0] would be the center of the pixel.

$$R_x = \frac{a_{top} - a_{bottom}}{a_{top} + a_{bottom}} \tag{4.1}$$

$$R_y = \frac{a_{right} - a_{left}}{a_{right} + a_{left}} \tag{4.2}$$

Using the calculated amplitudes from the example, this event occurred at a relative position of [-0.69,0.22] within the voxel.

4.5 Carrier Mobility

Using Eq. 2.3 and event waveforms, velocity can be calculated by dividing the thickness of the detector with the drift duration of a charge carrier across that thickness. The drift duration can be calculated by the difference between the inflection points of a planar cathode waveform. These inflection points mark the "start" and "stop" times of charge carrier drift following an interaction event. The electric field can be calculated by dividing the applied bias by the thickness of the detector.

4.6 Carrier Lifetime

Event waveforms from measurements at two different biases and from the depth closest to the planar cathode must be used for the calculation. The different biases enable the lifetime to be calculated from the relative difference of the charge carriers collected at each bias, obviating the need to know the number of charge carriers produced at the interaction. Using Eq. 2.4 at two different biases and solving for τ results in Eq. 4.3. The drift time t, in seconds, can be determined from the planar cathode waveforms of those events and the photopeak centroid A, typically in ADC voltage, can be determined from the energy spectrum of those events.[39] The carrier lifetime τ is typically quoted in seconds or microseconds.

$$\tau = \frac{t_2 - t_1}{\ln(A_1/A_2)} \tag{4.3}$$

Chapter 5

Small Sample Detectors

The small sample detectors had 3×3-pixel arrays and a volume of 0.13 to 0.81 cm^3. They were used to verify that a pixelated TlBr gamma-ray detector was possible and to optimize fabrication techniques and dimensions for X-ray and gamma-ray detection. The signals from these samples were read out with the discrete channel system described in Chapter 3. All wire-bonding was done with conductive carbon paste.

5.1 Characterization

RMD, Inc. fabricated various electrode compositions in order to determine which combination produced the best spectroscopic performance and the longest operating life. The selected pixel pitch is the optimal size for later detectors to be used with the VAD-UMv2.2 ASIC, which was designed for CZT.

Detector	Thickness [mm]	Cross-section [mm]	Pixel Pitch [mm]	Planar	Pixel
128BAS3	10	10 × 10	1.72	Cr/Au	Cr/Au
171CS5-3	10	8 × 8	1.72	Pt	Pt
171BS5-1(R)	10.1	8 × 8	1.72	Cr/Au	Cr/Au
175CS5-1(R)	9.5	8 × 8	1.72	Cr/Au	Pt
171BS5-2(R)	10	8 × 8	1.72	Cr/Au	Cr/Pd
175CS5-1(RR)	9.5	8 × 8	1.72	Cr/Au	Cr/Pd
128BAS3(R)	10	10 × 10	1.72	Cr/Au	Cr/Pd
173BS5-2	10	8 × 8	1.72	Cr	Cr
171CS5-3(R)	10	8 × 8	1.72	Cr/Au	Cr/Pd
Hi2-T3	5.5	5.8 × 5.8	1.15	Tl	Tl

Table 5.1: Small sample configurations

The ideal operating bias was -1000 V/cm because it seemed to produce adequate spectroscopic performance for the longest operating life. Higher biases such as -2000 or -3000 V/cm were sometimes attempted to check for improved spectroscopic performance, which was usually true in the short term. However they seemed to cause poor energy resolution quicker than operating at -1000 V/cm. Biases less than -1000 V/cm were sometimes recorded during "burn-in", in case performance degraded during that time. RMD, Inc. prescribes a "burn-in" bias because the planar cathode of a freshly fabricated detector tends to be unable to produce event waveforms at first. They typically performed this before sending detectors to University of Michigan (UM). While unusable cathode waveforms were observed in some detectors after arrival at UM, this problem resolved within hours to days under bias whether or not a "burn-in" bias was performed at UM.

Detector	Operating Bias [V]	Best Depth-Corrected Resolution [FWHM %]	
		All Pixels	One Pixel
128BAS3	-1200	2.2	1.8
171CS5-3	-1000	2.9	1.9
171BS5-1(R)	-1000	2.3	2.1
175CS5-1(R)	-600	2.6	1.8
171BS5-2(R)	-1500	2	1.6
173BS5-2	-1000	5.4	3.6
Hi2-T3	-500	2.4	2.0

Table 5.2: Small sample performance with single-pixel events. Resolution is in FWHM % at 662 keV.

The electron characteristics found in Table 5.3, except for tests with 175CS5-1, are similar to other results.[16], [21], [46] Some detectors did not produce enough quality data to calculate their electron lifetime.

Detector	Operating Bias [V]	Mobility $[\frac{cm^2}{V \cdot s}]$	Lifetime [s]	Mobility-Lifetime Product $[\frac{cm^2}{V}]$	Trapping Length at Operating Bias [cm]
128BAS3	-1000	23.4±3.3	Not enough data to calculate		
171CS5-3	-1000	24.2±3.4	$2.81(8)\times10^{-4}$	$6.8(1)\times10^{-3}$	6.8±1.2
171BS5-1(R)	-1000	25.0±0.4	$1.08(3)\times10^{-4}$	$2.66(8)\times10^{-3}$	2.64±0.09
175CS5-1(R)	-600	13.0±0.2	Not enough data to calculate		
171BS5-2(R)	-1500	24.7±0.4	Not enough data to calculate		
175CS5-1(RR)	-1000	14.6±0.2	Not enough data to calculate		
173BS5-2	-1000	23.3±3.3	$1.60(4)\times10^{-4}$	$3.7(5)\times10^{-3}$	3.7±0.6
Hi2-T3	-500	25.0±0.7	$8.5(10)\times10^{-4}$	$2.1(3)\times10^{-2}$	19.3±2.4

Table 5.3: Small sample electron characteristics

5.2 Platinum and Gold Electrodes

These detectors were fabricated by RMD, Inc.

5.2.1 Most Consistent Good Performance: 171BS5-2(R)

One detector each from ingots 128, 173, and 175 were tested, as well as three detectors from ingot 171. The detector with the most consistently good performance was 171BS5-2(R), as seen in Fig 5.1, achieving a single-pixel-event energy resolution of 2% FWHM at 662 keV.

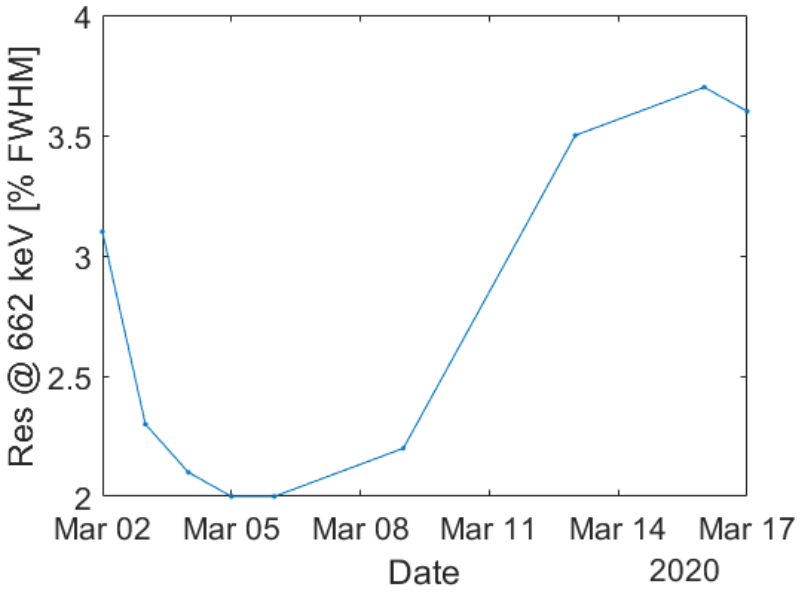

Figure 5.1: Detector 171BS5-2(R)'s single-pixel-event energy resolution at 662 keV and operated at -1500 V bias

RMD, Inc. operated this detector for more than 200 days, and they observed a promisingly consistent result of a raw energy resolution better than 4% at 662 keV before sending it to UM. At UM, it performed quite well from the beginning, improving until its best performance on the fourth day of operation, as seen in Table 5.2 and Fig. 5.2. By the eleventh day of operation, trapping had increased, which degraded the performance, as seen in Fig. 5.3. While some cathode-side photopeak events still remain at the centroid position as previous days, most of the photopeaks had a downward-

shifted centroid and had become broader towards the cathode side, which may have been from subpixel variance in trapping within each pixel. The cathode waveforms in Fig. 5.4a that are relatively linear during electron cloud movement at first versus the cathode waveforms in Fig. 5.4b that show a "slowing curve" later further demonstrate the increased trapping over time. It is possible that the time that the detector was not under bias during shipment allowed the bulk ions to recombine. This may explain the initially good performance after arrival at UM. The renewed reaction of bulk ions with the electrodes under when put into operation again may explain the quickly degraded performance at UM.

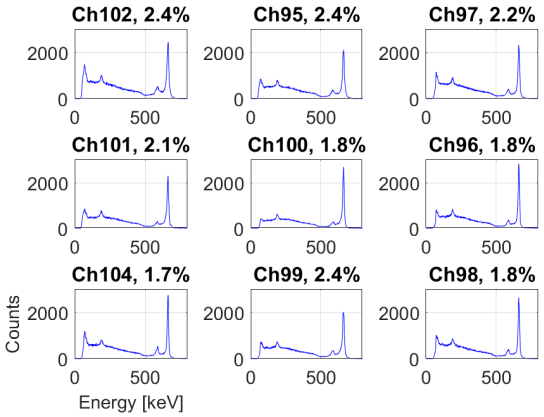

(a) **Corrected pixel energy spectra with resolution in FWHM %**

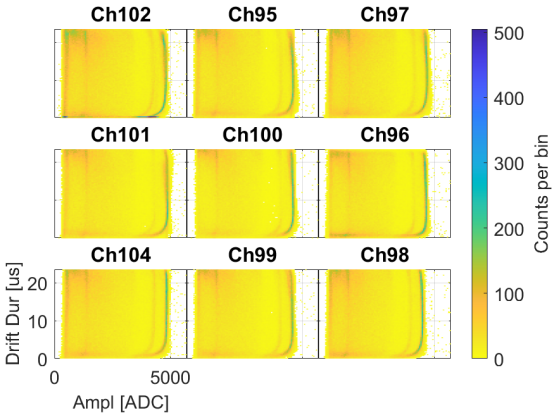

(b) **Pixel depth-gain curves**

Figure 5.2: Detector 171BS5-2(R) results at -1500 V bias with a Cs-137 check source on the 4th day of operation

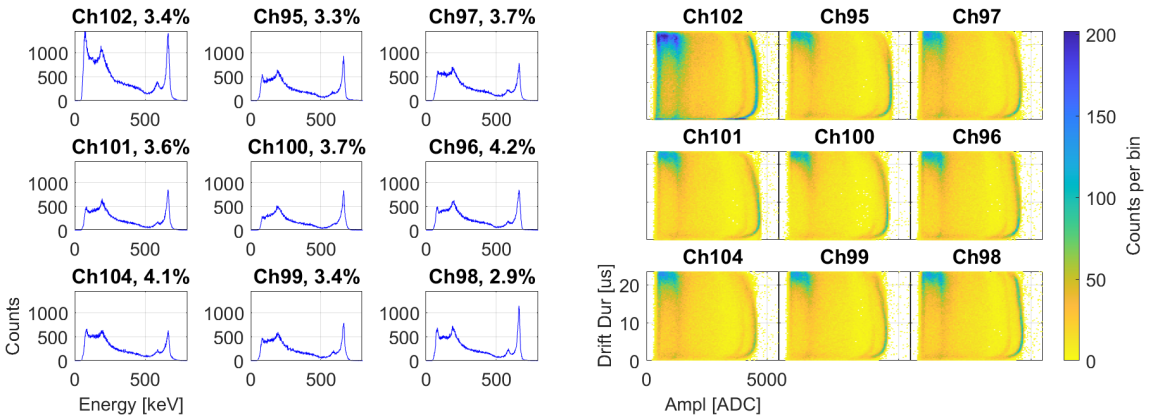

(a) Corrected pixel energy spectra. (b) Depth-gain curves.

Figure 5.3: Detector 171BS5-2(R) results at -1500 V bias with a Cs-137 check source on the 11th day of operation

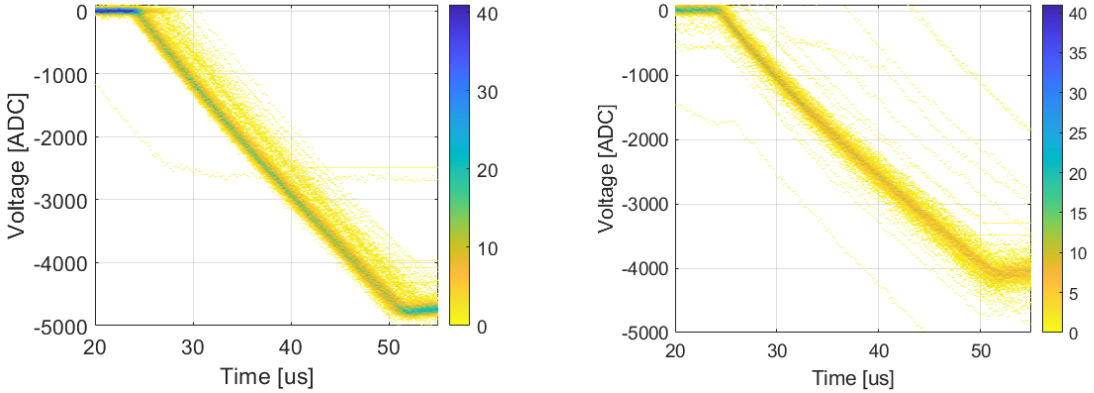

(a) First day (b) Last day

Figure 5.4: Detector 171BS5-2(R) photopeak event planar cathode waveforms from a middle-depth voxel (22.5-23.5 μs) of the center pixel

5.2.2 Long-Term Performance

All detectors that could produce a photopeak had worsening performance over time. The only exceptions were detectors with extreme trapping that showed decreasing trapping over time. Detectors 128BAS3 and 175CS5-1(R) achieved similarly good performance on their best days, but quickly developed significant trapping and lost their best performance.

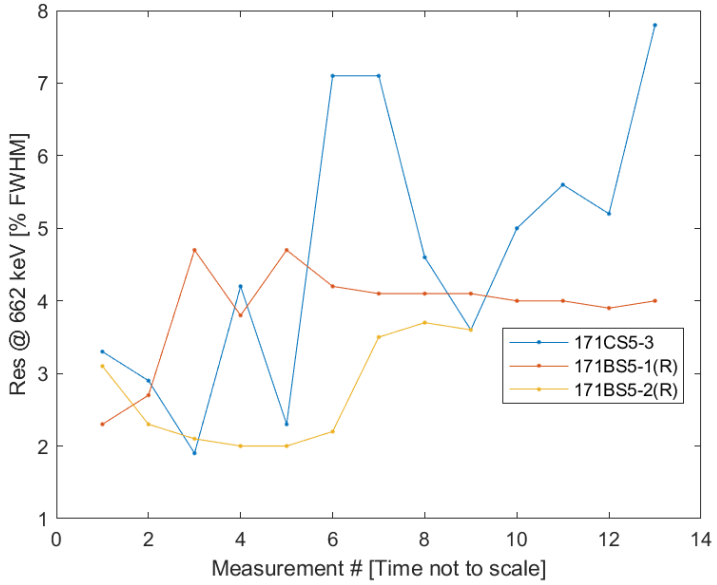

Figure 5.5: Total energy resolution at 662 keV over time of the three longest-lasting detectors. 171BS5-2(R) was operated at -1500 V while the other two were operated at -1000 V, which is contributed to it having the best performance

171CS5-3

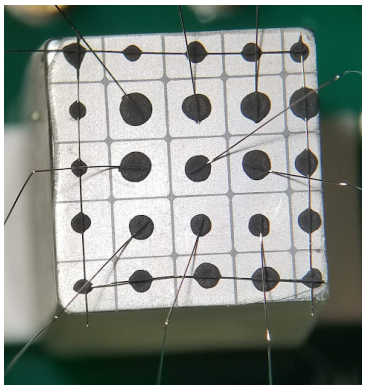

Figure 5.6: Detector 171CS5-3.

Electron characteristics were calculated using the average planar cathode waveforms, as mentioned in Ch. 2, for cathode-side events of Pixel 6 (the left-middle pixel) because that pixel was most consistently able to produce a photopeak. While Fig. 5.7 shows

Pixel 5 with best performance during that particular measurement, it was not sustained in that pixel.

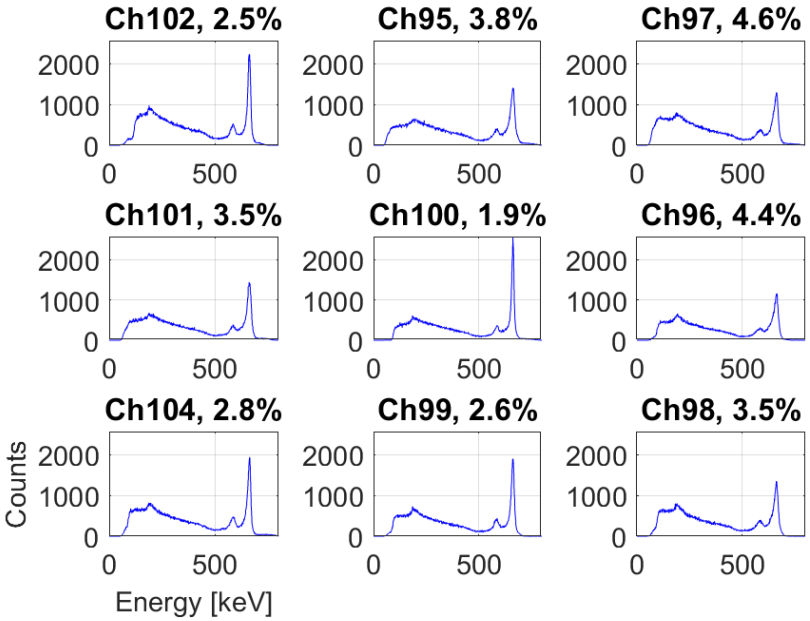

Figure 5.7: Detector 171CS5-3 depth-corrected pixel energy spectra and resolution [FWHM %] from a Cs-137 check source

Later results showed that full-energy events were not recorded in most pixels, particularly at depths toward the cathode, as seen in Fig. 5.8. Higher biases of -1500 V and -2000 V were able to record more events in this "dead" region. However, these higher biases showed unstable leakage current through the detector. Pixel 9 was able to perform as well as 1.5% FWHM during these later measurements, which was the best single-measurement pixel performance of all the small-sample detectors. "Good" pixels showed decreased trapping and increased electron lifetime, but overall detector performance had become poor. Since electron trapping seems to have decreased but fewer photopeak counts were observed in most pixels, as seen in Fig. 5.8b, there was likely a problem at the two surfaces between the electrodes and the bulk, such as a chemical reaction that created an insulating layer in some pixels.

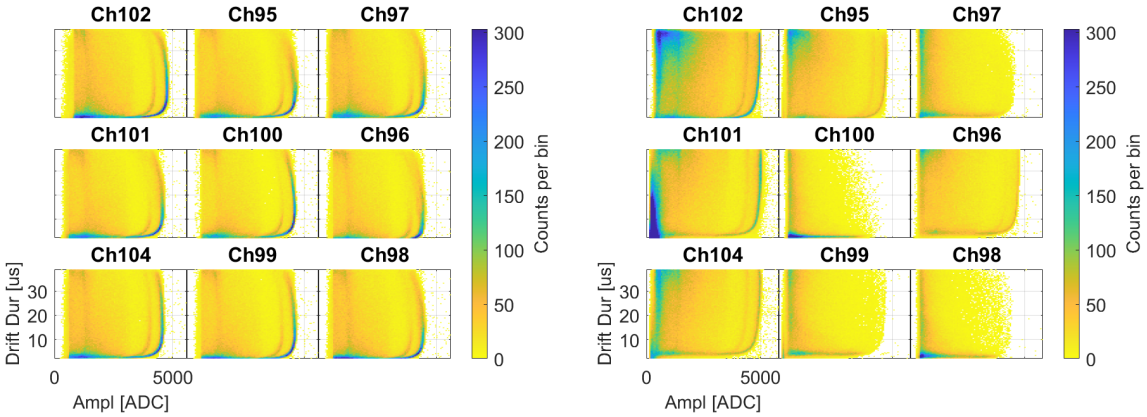

(a) Best performance, on the 3rd day of 34 days operation **(b) Final measurement of 34 days of operation**

Figure 5.8: Detector 171CS5-3 depth-gain curves with a Cs-137 check source

171BS5-1(R)

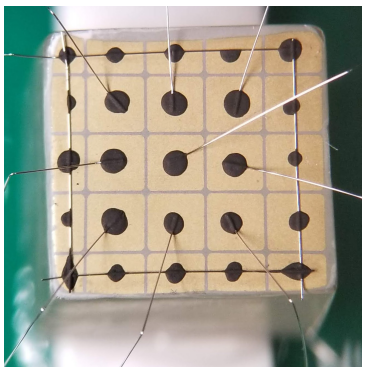

Figure 5.9: Detector 171BS5-1(R)

The event waveforms from the center pixel were used to calculate this sample's electron characteristics. A higher operating bias of -2000 V achieved better performance, but at the expense of a shorter detector operating life. The shortened operating life is most likely due to the conduction of electrode ions into the detector bulk. This detector's short trapping length, as seen in Table 5.3, is just over twice the thickness of the detector as well as lower than other detectors, which explains the increased trapping that developed while testing the detector.

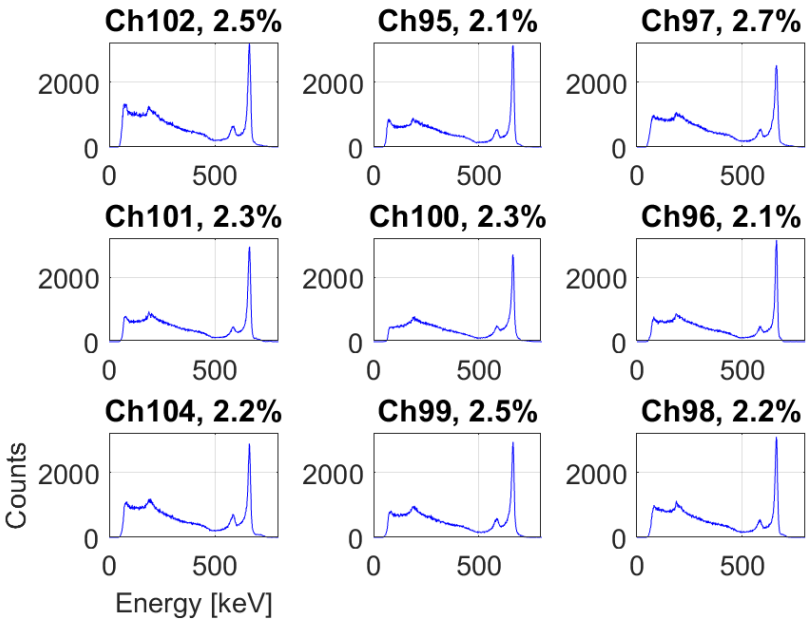

Figure 5.10: Detector 171BS5-1(R) depth-corrected pixel energy spectra and resolution [FWHM %] from a Cs-137 check source

Initial performance was good as shown in Fig. 5.10, but by the third day of 26 days of operation at -1000 V, overall corrected resolution had degraded to 4.7% FWHM at 662 keV and then remained around 3.8-4.2% FWHM. Trapping also increased, as shown by the decreasing amplitude in photopeak events towards the cathode side in Fig. 5.11b.

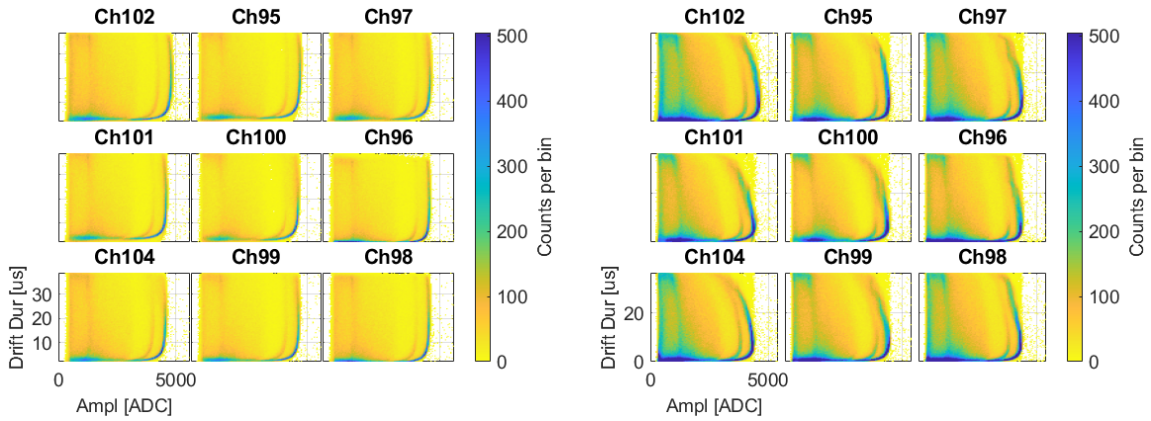

(a) First day **(b) Last day**

Figure 5.11: Detector 171BS5-1(R) depth-gain curves with a Cs-137 check source

In Fig. 5.11b, the photopeaks in Ch. 100 seems to separate into two peaks around the middle depths. When looking at the subpixel position of events from each peak, they occur in different areas of the pixel. Fig. 5.12a shows that events in a middle-depth voxel from the "lower-energy" photopeak occur mostly in the "southern" area of the voxel while Fig. 5.12b shows that "higher-energy" photopeak events occur mostly in the "northeastern" area of the voxel. Event cathode waveforms also show slightly more trapping in the "lower-energy" photopeak events. This shows that the amount of trapping is changing over time and location inside the pixel.

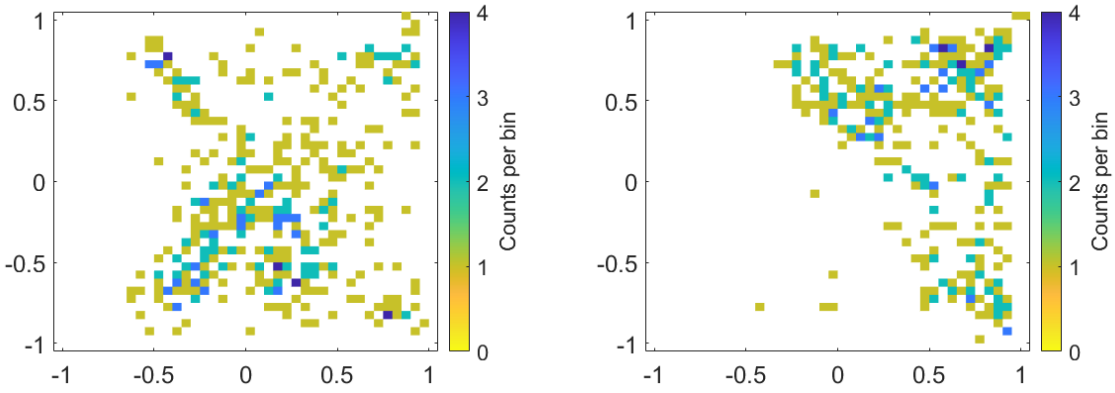

(a) Lower-energy **(b) Higher energy**

Figure 5.12: Detector 171BS5-1(R) subpixel position of middle-depth (22-23 μs drift duration) photopeak events in the center pixel

175CS5-1(R)

This detector was operated with a "burn-in" bias over four days, slowly ramping up from -100 V to -1000 V at regular intervals. This detector's best performance was during that series at -600 V, as seen in Table 5.2 and Fig. 5.13. During the first characterization measurement at -1000 V, the raw pixel spectra over time showed a diminishing photopeak while the low-energy counts increased, as seen in Fig. 5.14a. Bulk trapping had increased so much during the -1000 V measurement that during the second characterization measurement at -1425 V, events towards the cathode induced less charge, as seen in Fig. 5.14b. All subsequent measurements showed significant bulk trapping, similar to this figure. Later measurements at higher bias around -1500 V to -2000 V enabled some events to overcome trapping and measure closer to full energy

deposition, but not enough events to produce a usable photopeak.

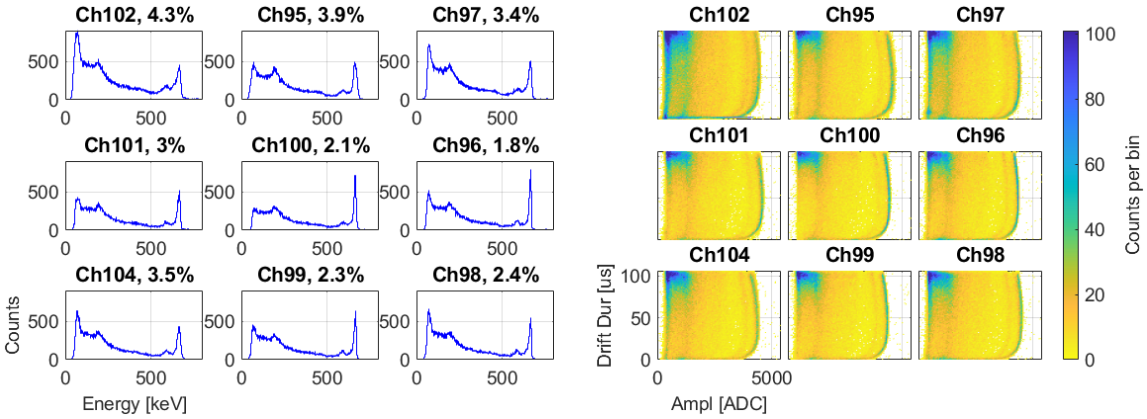

(a) Corrected pixel energy spectra **(b) Depth-gain curves**

Figure 5.13: Results at a -600 V bias with a Cs-137 check source

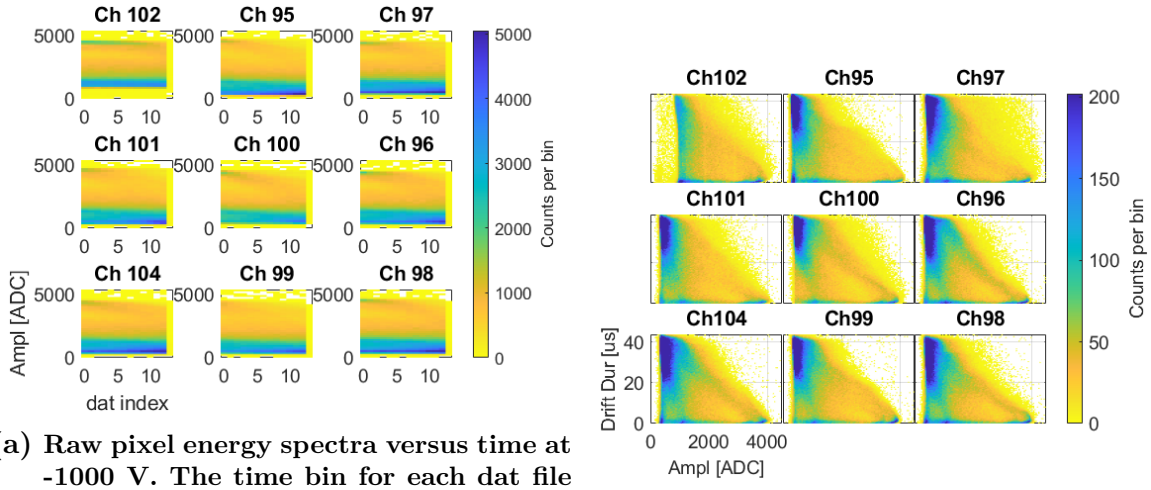

(a) Raw pixel energy spectra versus time at -1000 V. The time bin for each dat file was almost 2 hours.

(b) Depth-gain curves at -1425 V

Figure 5.14: Detector 175CS5-1(R)'s subsequent results at higher operating biases with a Cs-137 check source

173BS5-2

RMD, Inc. operated this detector for a month at -1000 V, then put it in storage for a month before sending it to UM for further testing. While its performance did improve over a week of operation at biases from -1000 V to -2000 V, no pixel could achieve an

energy resolution better than 3% FWHM at 662 keV. Fig. 5.15b shows how three pixels, channels 100, 95, and 102, seem to have a photopeak that diverges from the pixel side towards the cathode side. This divergence means that these pixels may have had two distinct regions with different amounts of trapping. In other words, events in one region of those pixels would have been subjected to more trapping and be recorded with less energy than events that occurred in the other region with less trapping.

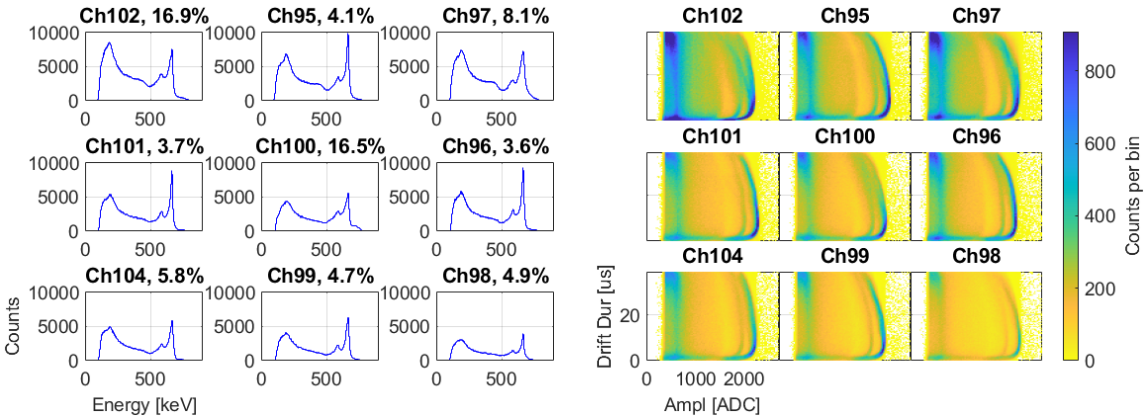

(a) Corrected pixel energy spectra **(b) Depth-gain curves**

Figure 5.15: Detector 173BS5-2 results at -1000 V bias with a Cs-137 check source

5.2.3 Electrode Refabrication

Electrode refabrication did not significantly improve performance. However, detectors 128BAS3(R) and 175CS5-1(RR) did show a slight decrease in trapping over time. All three detectors covered in this section had some combination of Pt and Cr/Au contacts before refabrication, but they were all refabricated so that their configuration from the planar cathode to the pixelated anode was Au-Cr-TlBr-Cr-Pd. Refabrication consisted of shaving off the previous electrodes as well as less than a millimeter of the bulk and then etching and applying new electrodes.

128BAS3

Dr. Charles Leak first tested this sample after its arrival from RMD, Inc., where he observed its best performance. When tested again after three months in storage at room temperature in a transparent cabinet, its overall depth-corrected performance had

degraded to over 4% FWHM at 662 keV. It was then operated at -1000 V for 42 days. After this period, bulk trapping had increased and overall depth-corrected performance had degraded to over 5% FWHM at 662 keV, as seen in Fig. 5.16.

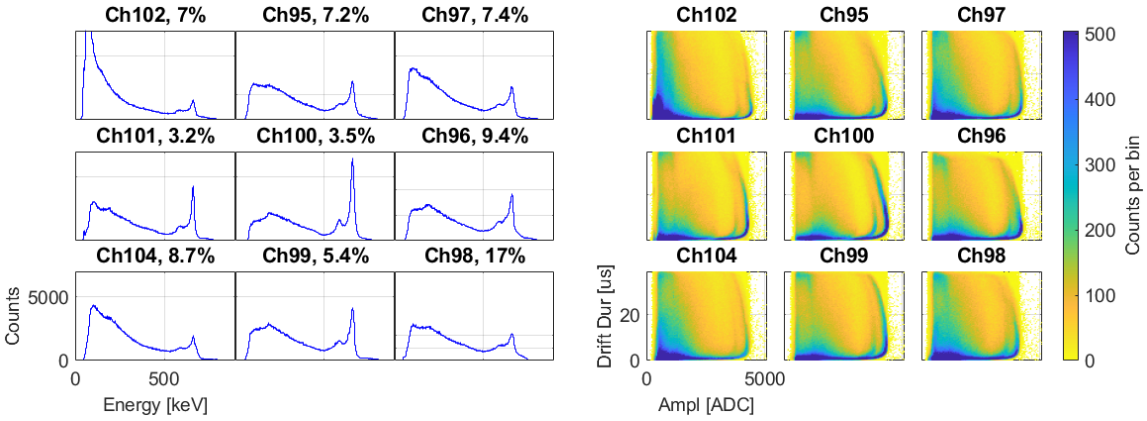

(a) Depth-corrected pixel energy spectra **(b) Depth-gain curves**

Figure 5.16: Detector 128BAS3 results with a Cs-137 check source

At the end of those 42 days of operation, it was found that the guard ring was mistakenly left electrically floating instead of grounded. The guard ring pixels appear physically unchanged, while the outer edges of the edge pixels appear to have reacted with the bulk material, as seen in Fig. 5.17. Had the guard ring been grounded as is usually the case with other samples, the physical change on the pixel anodes would have started on the guard ring instead.

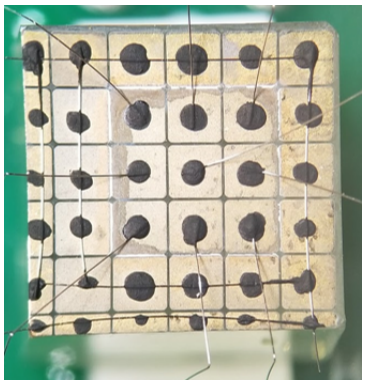

Figure 5.17: Detector 128BAS3.

128BAS3(R)

During the first measurement after refabrication, Fig. 5.18a shows that the depth-gain curves have a similar shape to those before refabrication. The high-energy edge, where the photopeak should be, decreased in energy at each depth towards the cathode side, indicating significant bulk trapping. However, trapping improved over about a month of operation and a month of rest, as seen in Fig. 5.18b, because high-energy events were recorded with a consistent energy at most depths. Even with the decreased trapping, this detector did not produce a usable photopeak again.

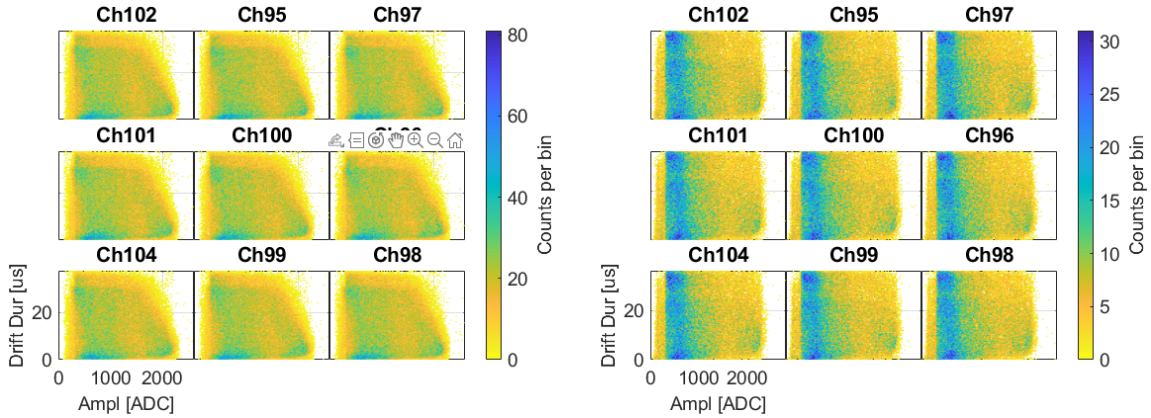

(a) First day **(b) Last day**

Figure 5.18: Detector 128BAS3(R) depth-gain curves at -1000 V with a Cs-137 check source

171CS5-3(R)

This detector was operated at biases from -1000 V to -2000 V and generally had an unstable leakage current. It did not produce a 662-keV photopeak during any measurement, as seen in Fig. 5.19a. Dr. Charles Leak showed in simulation that electron trapping will cause an event to have an elevated cathode-to-anode ratio.[47] The depth-gain curves in Fig. 5.19b show that many events had a reduced amplitude and an elevated cathode-to-anode ratio, supporting his simulated results.

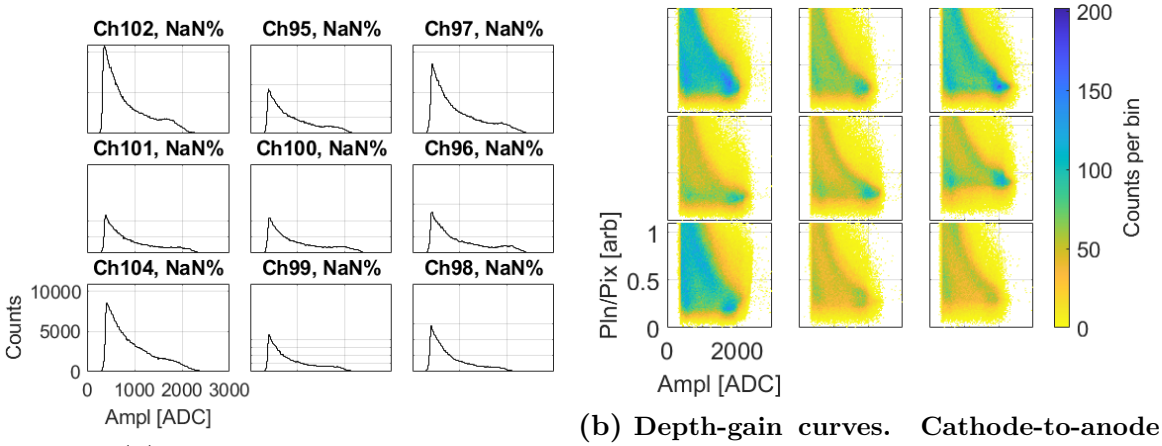

(a) Raw energy spectra

(b) Depth-gain curves. Cathode-to-anode ratio versus pixel amplitude.

Figure 5.19: Detector 171CS5-3(R) pixel results at -1000 V operating bias from a Cs-137 check source

This detector was operated with a "burn-in" bias from -100 V to -1000 V for three days prior to it's first measurement, which may have contributed to the detector's trapping and poor performance. During the "burn-in" biasing, leakage current peaked at about 40 nA during the step at -600 V, then gradually continued to decrease and settle at less than 10 nA when operated at -1000 V. Refabrication did not recover good performance in this detector, and the days-long "burn-in" bias may have contributed to the ionic conduction of electrode materials through the bulk. It would have been better to skip the "burn-in" and start measurements at -1000 V immediately after arrival to watch for a change in trapping in the initial hours or days. It is also notable that few events were recorded outside of the near-pixel depths, so it would have been better to conduct measurements immediately upon operation to attempt to observe events outside the near-pixel region.

175CS5-1(RR)

The first measurements with this sample showed a significant level of trapping, as seen in Fig. 5.20a, similar to the last operation before refabrication. The level of trapping appeared to fluctuate between measurements over the two months of operation. The last day of operation showed the least trapping of all measurements, as seen in Fig. 5.20b, but no usable photopeak was seen from any pixel's energy spectrum.

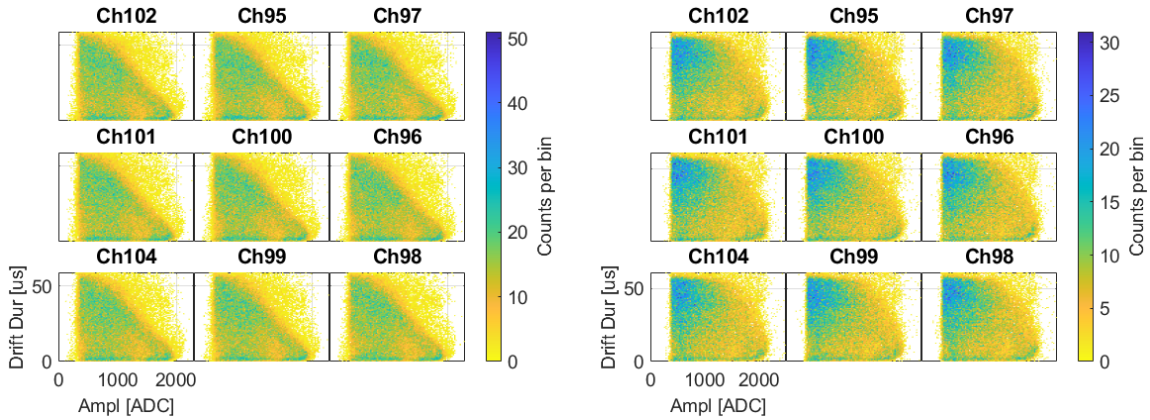

(a) First day of operation **(b) After over two months of operation**

Figure 5.20: Detector 175CS5-1(RR) depth-gain curves at -1000 V bias from a Cs-137 check source

5.3 Thallium Electrodes on Detector Hi2-T3

Detector Hi2-T3, as seen in Fig. 5.21, was fabricated by Professor Keitaro Hitomi of Tohoku University. Its electrodes were made of thallium to suppress polarization due to the chemical reaction of bulk ions with the electrodes.[48] Suppression is achieved through thallium ions reacting with the thallium electrodes, resulting in no perceptible change in performance. This is opposed to thallium ions reacting with a non-thallium electrode, like gold, which causes poorer resolution and can't be reversed with reversing bias polarity. After wire-bonding was completed, the entire sample was encapsulated to prevent reaction of the thallium electrodes with air. Electron characteristics were calculated using the average planar cathode waveforms for cathode-side events of the center pixel.

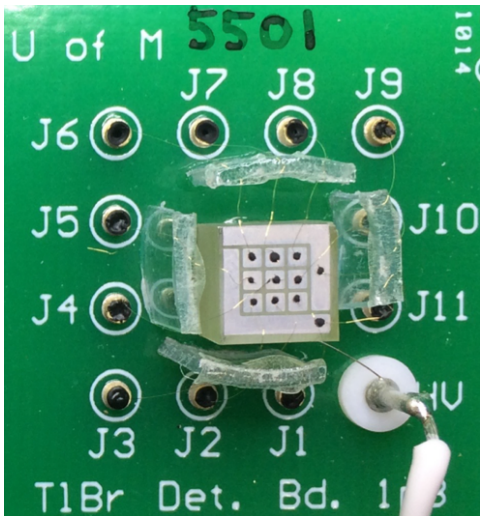

Figure 5.21: Detector Hi2-T3

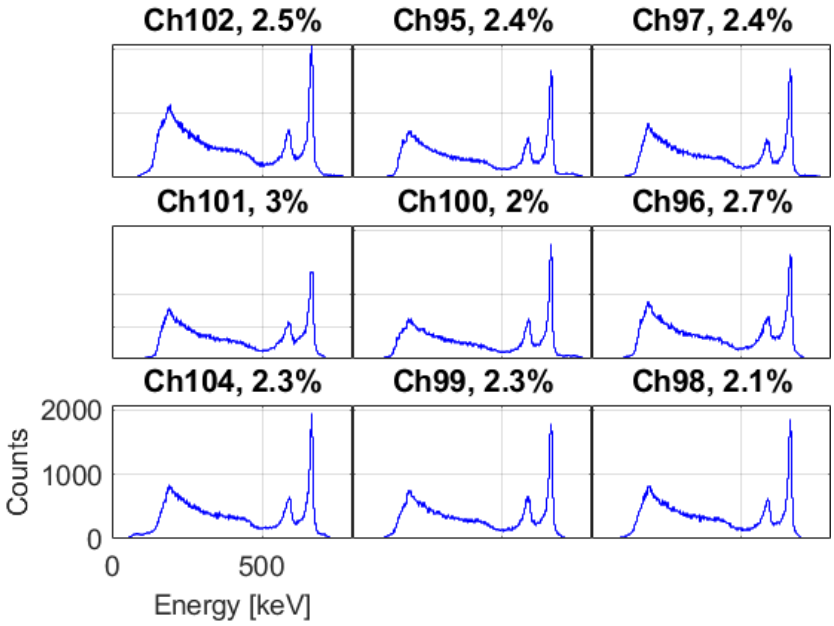

Figure 5.22: Detector Hi2-T3 depth-corrected pixel energy spectra and resolution at -500 V operating bias from a Cs-137 check source

Various works have shown that alternating the bias polarity on the planar electrode at regular intervals can extend the usable lifetime of the detector. Hitomi et al. found that switching every 24 hours caused minimal shift in a 662 keV photopeak over 600 operating

hours.[46] Datta et al. found that switching every 16 hours, or more frequently, caused minimal shift in a 662 keV photopeak and consistent photopeak energy resolution over at least 12,000 operating hours.[49]

In my experiment, Hi2-T3 was operated with a negative bias between -400 V and -1000 V on the planar electrode for a cumulative 35 days over a 6-month period from June to November 2018, averaging -558 V. This mimics a more realistic operating schedule as a field user will likely be turning the detector on and off for months a time before being able to put it into a sort of "maintenance" mode. It is must less likely that a field user will have the detector constantly under a regularly switching bias. Depth-corrected energy resolution steadily improved from 4.9% to 2.4% FWHM at 662 keV. Within one week in late November 2018, energy resolution worsened, back to 4.6% FWHM at 662 keV. This is likely due to the continuous operation as well as various higher bias measurements around -600 V to -1000 V. After that, the detector was operated for 35 days, from late November 2018 to early January 2019, with a positive bias between +200 and +500 V on the planar electrode, averaging +233 V. Readout was attempted a few times in this configuration, unsuccessfully, but it is worth exploring in the future. When operated again with a negative bias in February 2019, energy resolution returned to 2.5% FWHM at 662 keV.

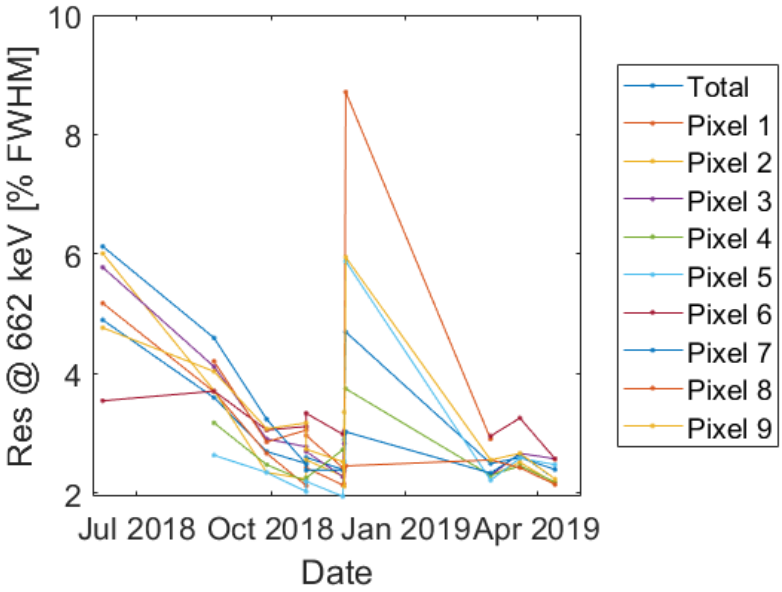

Figure 5.23: Detector Hi2-T3 depth-corrected energy resolutions in FWHM % at 662 keV at -500 V operating bias over time

The depth-gain curves in Fig. 5.24b show a photopeak at all depths with negligibly shifted centroids over time, which implies that the bulk material was not significantly changing over time. However, the photopeak blurring and degraded energy resolution at the end of the first negative bias period implies that a problem at the electrodes was negatively affecting the recorded energy. In this detector, it seems that about 35 operating days "consumed" or otherwise degraded the pixelated anodes to the point where a reverse polarity bias was needed to move thallium that had been accumulating on the planar electrode back to the pixelated electrodes.

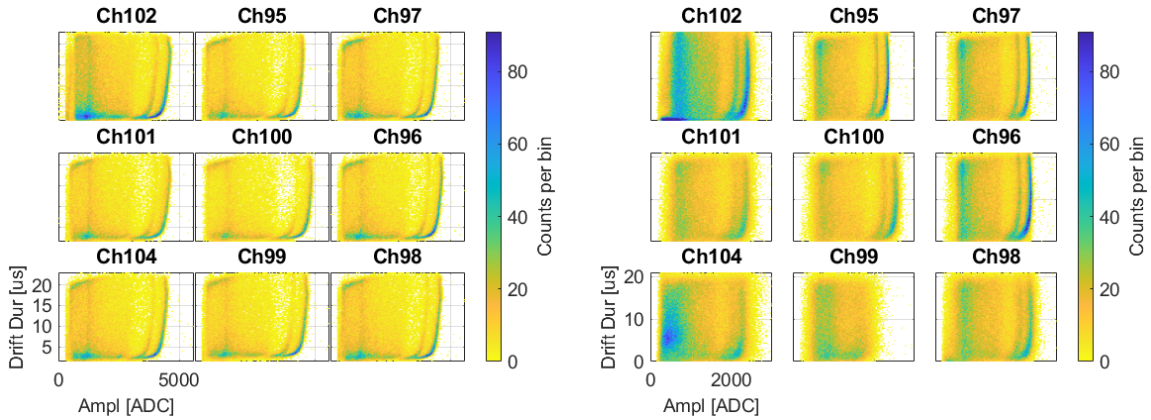

(a) At the start of the first negative bias **(b) At the end of the first negative bias**

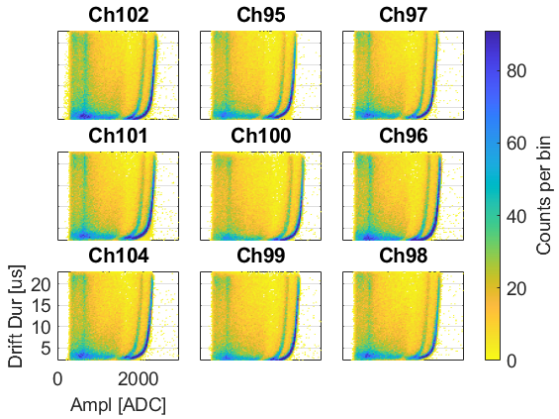

(c) At the start of the second negative bias

Figure 5.24: Detector Hi2-T3 depth-gain curves at-500 V operating bias from a Cs-137 check source

Pixel and planar waveforms from photopeak events in the near-cathode voxel of the center pixel were much more consistent before Hi2-T3 started to "fail". Fig. 5.25a shows relatively consistent waveforms within that voxel, but Fig. 5.25b shows some variation in the pixel waveforms and drastic inconsistency in the planar waveforms. Noise in some of the planar waveforms caused them to have an early and incorrect start time, which then caused them to be reconstructed at the incorrect depth, subsequently degrading energy resolution. Incorrect depth reconstruction might be mitigated with more robust event processing techniques. Fig. 5.25c shows that consistent performance returned after the positive bias period. As described by Hitomi et al., the inconsistent planar waveforms were likely due to chemical reactions degrading the electrodes, so the positive bias period

corrected those reactions and led to better performance during the subsequent negative bias period.

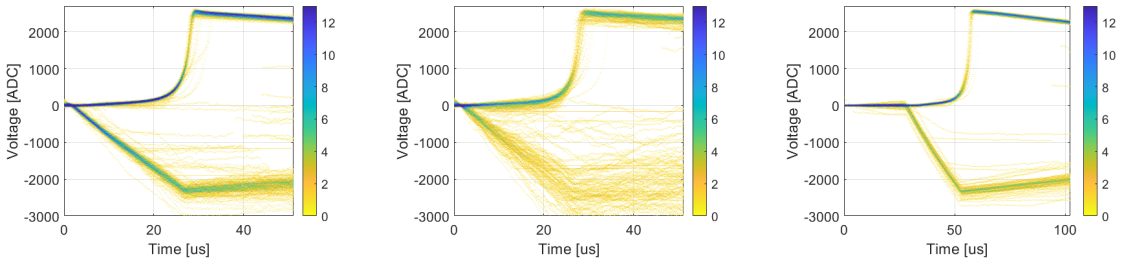

(a) Best performing date, 19 Nov 2018 **(b) End of the first negative bias, 21 Nov 2018** **(c) Start of the second negative bias, 28 Feb 2019**

Figure 5.25: Detector Hi2-T3 pixel and planar waveforms from events in the near-cathode voxel of the center pixel during -500 V operating bias

5.4 Conclusions

Movement of materials within the detector crystal bulk and from the electrodes is the main reason why these detectors lost reliability. Small changes in trapping can be corrected with depth-correction, but other factors are changing waveform shape and characteristics over time. This is the cause of degrading spectroscopic performance.

Due to the permutations of ingot chemistry, electrode composition, and operating histories, it is difficult to make many specific conclusions. The detector from ingot 175 seemed to develop extreme trapping very quickly while detectors from other ingots maintained better performance for longer operation. It also had an electron mobility that was about half that of detectors from other ingots. However, the refabricated detector from ingot 175 showed some decrease in electron trapping over time.

Of the various electrode materials that were tried by RMD, Inc., most had great performance initially, but would degrade after some varying period of time. No particular electrode configuration stood out as reliable in the long-term. Continued poor performance after electrode refabrication shows that electrode material has likely reacted with and diffused into the bulk. One exception might be the detectors that had a Cr/Pd pixel array; all but one of those detectors eventually showed some improvement in trapping. While spectroscopic performance will show some recovery after refabrication, it did not

recover to the previous best performance at the observed operating durations. Using a synchrotron light source to detect if certain electrode elements have traveled through the bulk and deposited on the opposite electrode would be helpful in this diagnosis.[50]

The thallium electrodes by Professor Hitomi did mostly recover performance after one long-term bias cycle. Multiple long-term bias cycles of this sample's configuration to check repeatability would be interesting to explore. In the future, it would also be good to mount detectors on their side in order to observe the planar cathode after operation to look for a "pixel pattern" effect that will be described in the next chapter.

Chapter 6

Flip-chip-bonded Detectors

These samples had 6×6-pixel to 11×11-pixel arrays and a volume of 0.8 to 4.4 cm^3. Signals from these samples were read out with the ASIC systems described in Chapter 3. Their name comes from how they are bonded to the carrier board with the pixelated electrode facing downwards, which is the opposite of the small 3×3-pixel array detectors.

6.1 Detector Characterization

For the same reasons as the small-sample detectors, RMD, Inc. fabricated various electrode compositions to determine which combination produced the best spectroscopic performance and the longest operating life. Older samples had a 1 mm pixel pitch, but detectors were later standardized with 1.72 mm pixel pitch, which is the optimal size for use with the VAD-UMv2.2 ASIC.

Detector	Thickness [mm]	Pixel Array	Pixel Pitch [mm]	Planar	Pixel
139BS9(R5)	6	11 × 11	1	Cr/Pd	Cr/Pd
171A3	5	11 × 11	1	Cr/Pd	Cr/Pd
935-38AS4	5	11 × 11	1	Cr/Au	Cr/Pd
185DS3	10	6 × 6	1.72	Pt	Pt
168CS2	10	6 × 6	1.72	Cr/Au	Cr/Pd
186BS5	10	6 × 6	1.72	Cr/Au	Cr/Pd
171AS5	10	9 × 9	1.72	Cr/Au	Cr/Pd
193BS4-1	10	6 × 6	1.72	Cr/Au	Cr/Pd
212BS2	10	6 × 6	1.72	Cr	Cr
212BS3	10	9 × 9	1.72	Cr	Cr
203BS2(R)	10	11 × 11	1.72	Cr	Cr
212BS2(R)	10	6 × 6	1.72	Cr	Cr
212AB1	10	11 × 11	1.72	Cr	Cr
212CS2	10	6 × 6	1.72	Cr	Cr
212AB2	10	11 × 11	1.72	Cr	Cr

Table 6.1: Flip-chip-bonded detector configurations.

Operating bias selection and "burn-in" bias were performed for the same reasons as the small-sample detectors.

Detector	Operating Bias [V]	Best Corrected Resolution [FWHM %]	
		All Pixels	Best Pixel
139BS9(R5)	-1800	3.8	1.6
171A3	-1500	1.7	1.2
935-38AS4	-1500	2.0	1.2
168CS2	-2500	4.1	2.1
186BS5	-1000	6.9	3.1
193BS4-1	-1000	3.1	2.0
171AS5	-1504	2.6	1.5
212BS2	-1000	5.4	3.3
212BS3	-2500	4.0	1.9
203BS2(R)	-1000	2.3	1.5
212BS2(R)	-1000	6.9	2.2
212AB1	-1000	1.8	1.4
212CS2	-1000	2.9	2.1
212AB2	-1000	3.2	1.8

Table 6.2: Flip-chip-bonded detector performance with single-pixel events. Resolution is in FWHM % at 662 keV.

The electron characteristics found in Table 6.3, are also similar to other results.[16], [21], [46] Three exceptions are the electron mobility and lifetime product of the detectors with a 1 mm pixel pitch, which may have been due to error with the sampling rate setting. It seems as though they were actually sampled at 5 MHz, which was twice the intended rate of 2.5 MHz. If their calculated mobility is doubled, the values are more similar to other results. Also, measurements at a second operating bias were not performed with two other detectors with a 1.72 mm pitch, so there was not enough data to calculate their electron lifetime.

Detector	Operating Bias [V]	Mobility $[\frac{cm^2}{V \cdot s}]$	Lifetime [s]	Mobility-Lifetime Product $[\frac{cm^2}{V}]$	Trapping Length at Operating Bias [cm]
139BS9(R5)	-1800	11.9 ± 2.8	1.08(5) $\times 10^{-4}$	1.3(3) $\times 10^{-3}$	3.9 ± 1.1
171A3	-1500	12.0 ± 1.7	2.07(6) $\times 10^{-4}$	2.5(4) $\times 10^{-3}$	4.8 ± 0.9
935-38AS4	-1500	10.1 ± 1.4	2.6(1) $\times 10^{-4}$	2.7(4) $\times 10^{-3}$	8.0 ± 1.4
193BS4-1	-2000	23.8 ± 3.4	8.2(12) $\times 10^{-5}$	2.0(4) $\times 10^{-3}$	3.9 ± 0.9
168CS2	-2500	21.9 ± 1.6	1.7(5)$\times 10^{-4}$	3.7(10)$\times 10^{-3}$	6.9 ± 1.8
186BS5	-1500	26.6 ± 3.8	1.8(1)$\times 10^{-4}$	4.4(7)$\times 10^{-3}$	6.6 ± 1.2
171AS5	-1500	25.3 ± 1.8	7.3(5) $\times 10^{-5}$	1.8(2) $\times 10^{-3}$	1.9 ± 0.2
212BS2	-1500	25.9 ± 1.9	2.9(18)$\times 10^{-4}$	7.5(46)$\times 10^{-3}$	13.2 ± 7.6
212BS3	-1500	24.2 ± 1.7	2.3(4) $\times 10^{-4}$	5.7(11) $\times 10^{-3}$	7.1 ± 1.6
212BS2(R)	-1500	27.1 ± 2.0	8.6(10) $\times 10^{-5}$	2.3(3)$\times 10^{-3}$	3.5 ± 0.5
212AB1	-1250	23.8 ± 1.7	Not enough data to calculate		
212CS2	-1000	25.5 ± 1.8	Not enough data to calculate		
212AB2	-1000	24.7 ± 1.8	2.43(8) $\times 10^{-3}$	6.0(5) $\times 10^{-3}$	6.0 ± 0.6

Table 6.3: Flip-chip-bonded detector electron characteristics.

6.2 Difficulties with the VAD-UMv2.2 ASIC

6.2.1 Sampling Rate

For all measurements with the Orion Solo readout system, the 2.5 MHz sampling rate was used. This is the second-slowest sampling rate designed in this ASIC. This sampling rate is achieved by inputting a 20 MHz square wave master clock to the ASIC from the Field-Programmable Gate Array (FPGA), and using the ASIC's internal settings to further divide that clock speed by eight. Fig. 6.1 is an example of event waveforms using the 2.5 MHz sampling rate and shows an event that is barely captured within the sampling window.

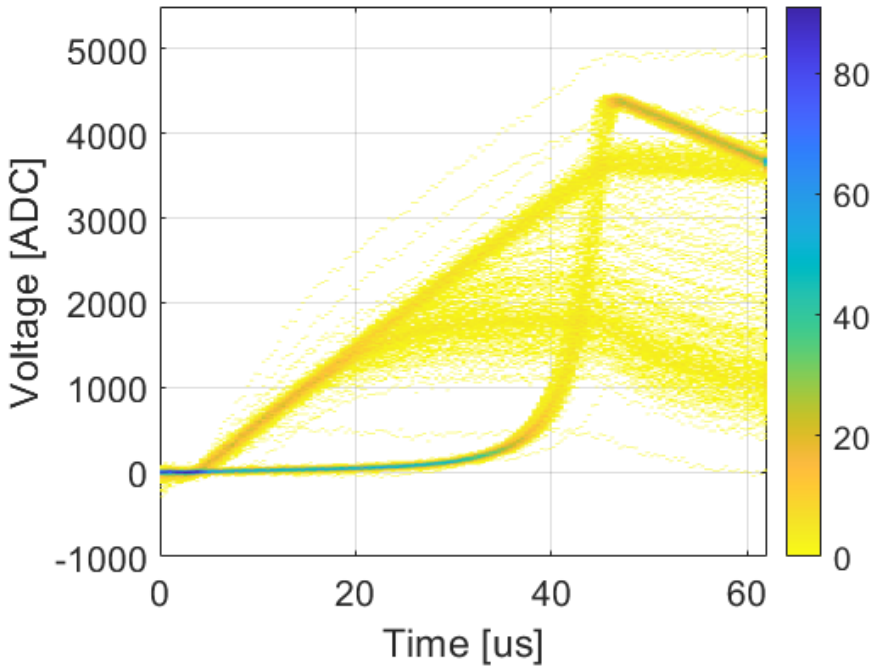

Figure 6.1: Photopeak-event pixel anode and planar cathode waveforms from a near-cathode voxel of an inner pixel of Detector 171A3 at -500 V operating bias

The most important portions of an interaction event waveform, which were covered in Chapter 4, must be captured within the sampling window. One solution is to simply use a higher operating bias to make the electron cloud drift quicker in order to make the drift duration as short as possible. However, a lower operating bias of 1000 V/cm is preferred in order to preserve a detector's operating lifetime. Another solution is to adjust the sample hold delay so that the triggered sample occurs later in the sampling window. Typically, the triggered sample is set in the middle of the sampling window to ensure that adequate lengths of the waveform baseline at the beginning and the waveform tail at the end are recorded. Adjusting the sample hold delay was generally enough to fully capture event waveforms by bringing the event start at the front of the cathode waveform into the sampling window, but longer waveform baselines and tails would have been ideal.

An even better solution would have been to use this ASIC's slowest sampling rate of 1.25 MHz. This sampling rate should be achievable by inputting a 10 MHz square wave

master clock into the ASIC and dividing that clock speed by 8. Two other researchers, Damon Anderson and Dr. Matthew Petryk, as well as myself confirmed that the FPGA was sending the 10 MHz square wave to the ASIC, but no outputs were observed from the ASIC whether the clock speed was divided by 1, 2, 4, or 8. Equivalent sampling rates could be achieved with various combinations. For example, 5 MHz could be achieved with a 40 MHz master clock divided by 8, a 20 MHz master clock divided by 4, or a 10 MHz master clock divided by 2. However, the ASIC failed to produce any output with a 10 MHz master clock. Matthew and Damon attempted various other settings but were also unable to observe outputs from the ASIC.

6.2.2 Trigger Shaper

Until March 2022, flip-chip-bonded detectors were tested with the VAD-UMv2.2 ASIC's "700 keV" dynamic range. This "700 keV" was derived from CZT's W-value of 5 eV per electron-hole pair. So this setting should allow measurement of photons up to 910 keV in TlBr, considering TlBr's W-value of 6.5 eV per electron-hole pair. This should not have been an issue to measure 662 keV gamma rays from Cs-137. However, at this dynamic range, and with a number of detectors, there were few events recorded from most depths of the bulk and most events were recorded from the near-pixel region, as seen in Fig. 6.4a. This makes depth correction difficult, if not impossible. The trigger shaper seemed to be preventing many bulk events from meeting the trigger threshold.

139BS9(R5)

This detector required a relatively high bias of -1200 V (2000 V/cm) before a photopeak was observed. Its best performance was at -1800 V (3000 V/cm), as seen in Figs. 6.2 and 6.3.

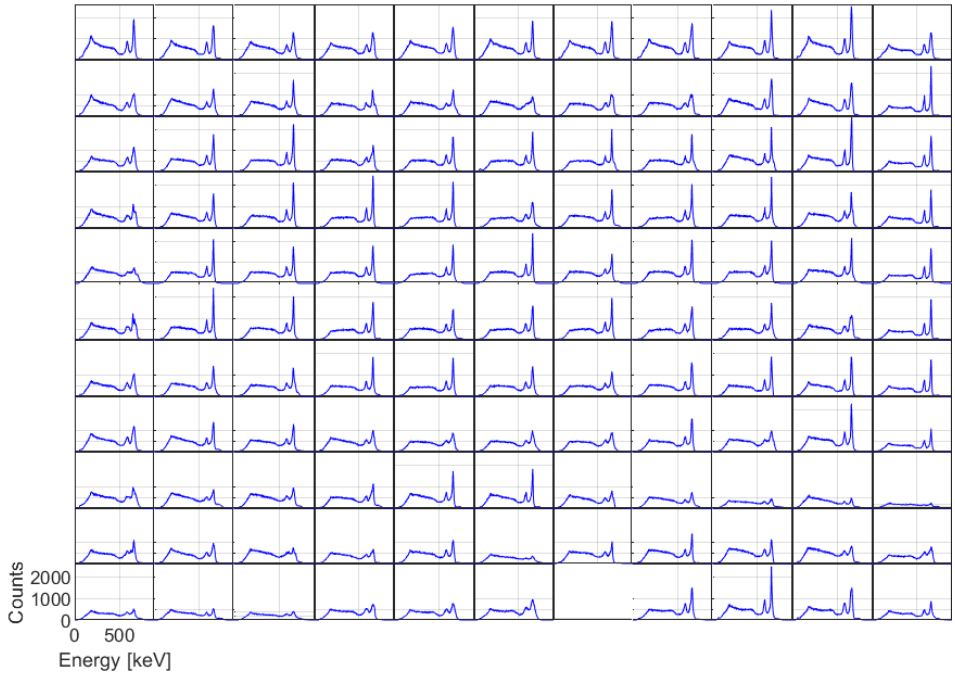

Figure 6.2: Detector 139BS9(R5) depth-corrected pixel spectra at -1800 V with a Cs-137 check source

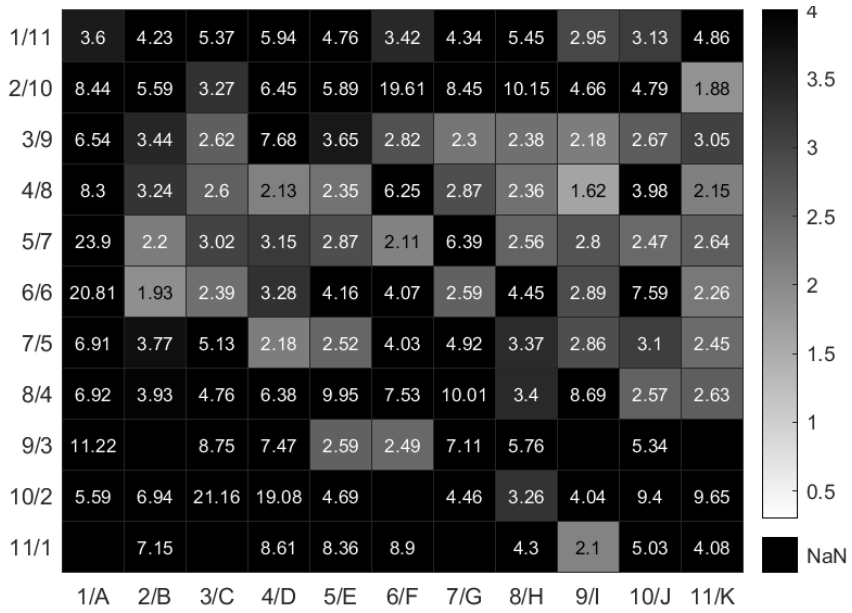

Figure 6.3: Detector 139BS9(R5) depth-corrected pixel resolution in FWHM percentage at -1800 V with a Cs-137 check source

Fig. 6.4a shows how this detector with significant trapping likely produced event waveforms that rose too slowly to meet the trigger threshold, so they were not recorded. At the lower -600 V bias, events were subjected to enough electron trapping that they could not meet trigger threshold. When the detector was operated at higher biases, as seen in Figs. 6.4b and 6.4c, the bias was high enough to overcome enough electron trapping that more photopeak events closer to the cathode were meeting the trigger threshold and being recorded.

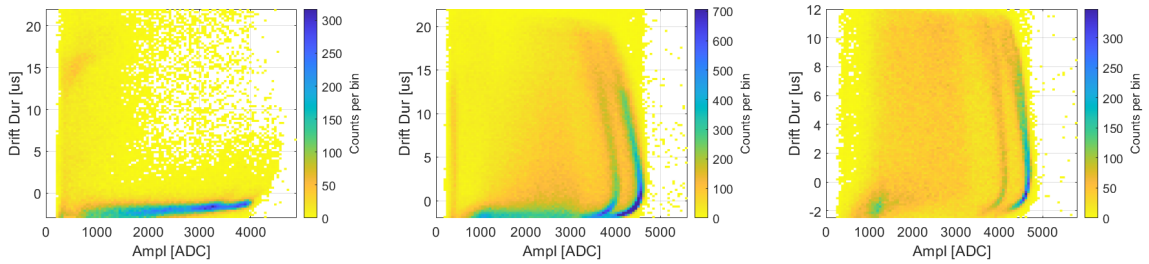

(a) -600 V **(b) -1200 V** **(c) -1800 V**

Figure 6.4: Depth-gain curves of the center pixel in Detector 139BS9(R5) at various operating biases with a Cs-137 source

.

171A3

This detector performed well, comparable to the small detectors from ingot 171. However, it also required a relatively high bias of -1500 V (3000 V/cm) to achieve its best performance, as seen in Figs. 6.5 and 6.6. When this detector with minimal trapping was tested, as seen in Fig. 6.7, photopeak events were recorded at all depths, even at the preferred lower bias of -500 V (1000 V/cm). Higher biases further counteracted the low electron trapping in the detector bulk and produced a better energy resolution as well.

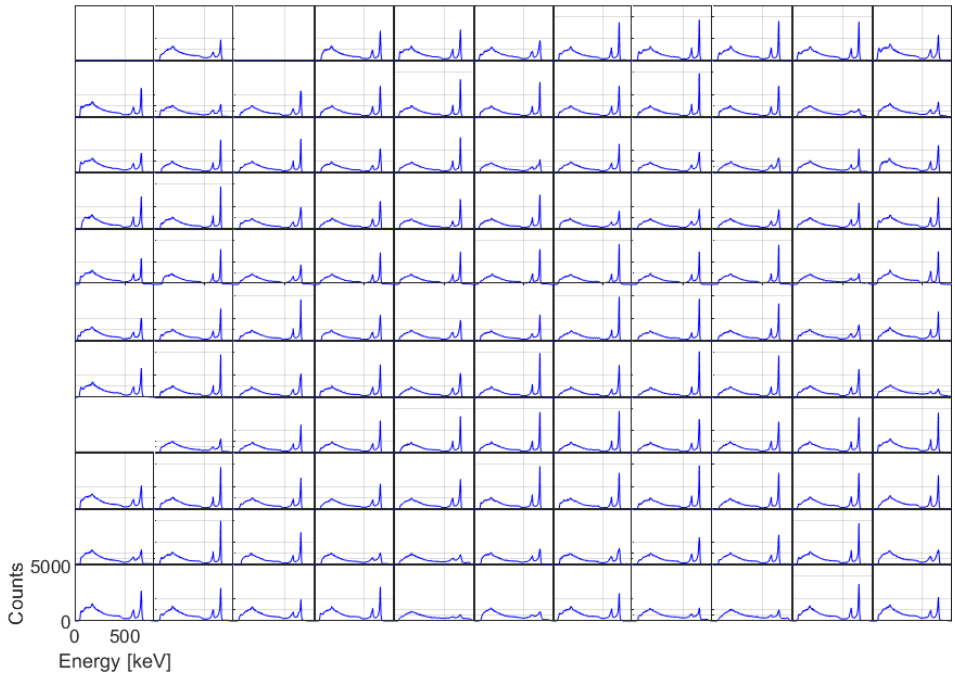

Figure 6.5: Detector 171A3 depth-corrected pixel spectra at -1500 V in an Orion Solo with a Cs-137 check source

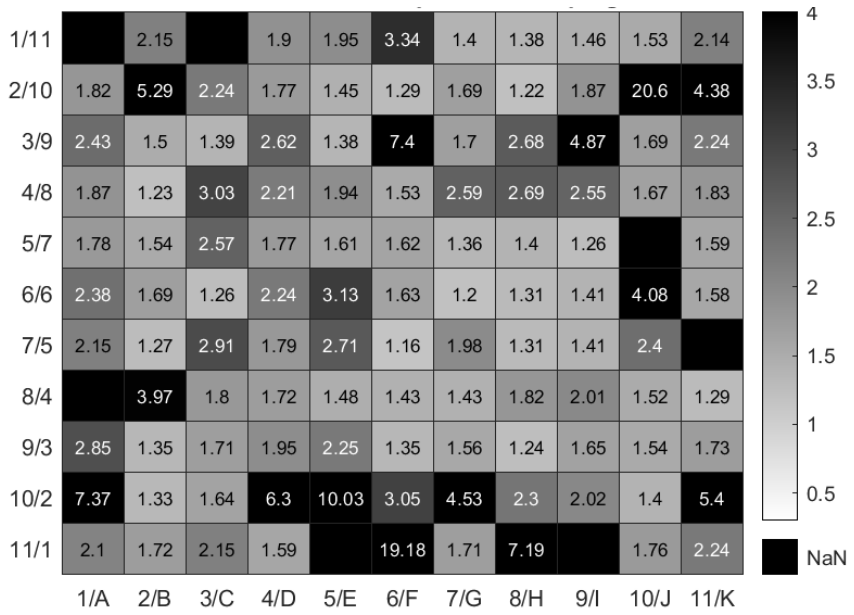

Figure 6.6: Detector 171A3 depth-corrected pixel resolution at -1500 V in an Orion Solo with a Cs-137 check source

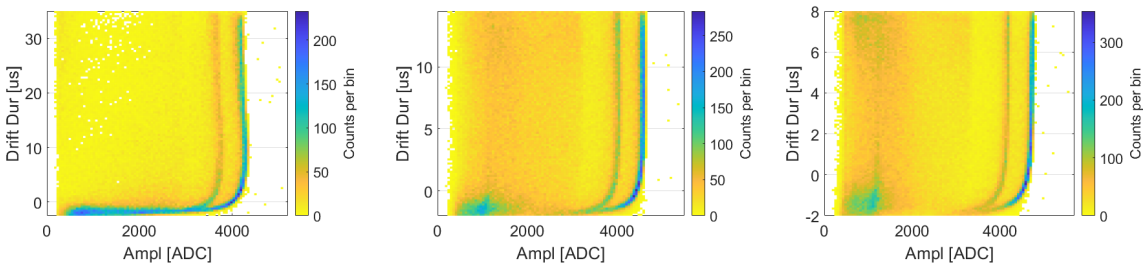

(a) -500 V **(b) -1000 V** **(c) -1500 V**

Figure 6.7: Depth-gain curves of an inner pixel in Detector 171A3 at various biases with a Cs-137 source

However, the results with the H3D S Series were not as good because something had changed in the detector. When it was removed and retested in an Orion Solo, the results looked similarly poor to the results in an H3D S Series rather the previous good results in an Orion Solo. Trapping had not increased, but photopeak energy resolution worsened at all depths. Fig. 6.8 shows that the photopeak and x-ray escape peak were both widening. With more operating time, this detector may have shown "double-peaking", which will be discussed later in this chapter.

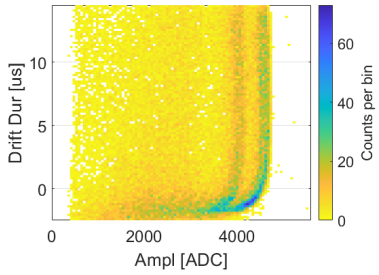

Figure 6.8: Detector 171A3 depth-gain curve of an inner pixel at an operating bias of -1000 V in an Orion Solo with a Cs-137 check source

193BS4-1

To further confirm that the trigger problem was dependent on the depth of interaction, this detector was irradiated with a Co-57 source from the pixelated anode side and then again from the planar cathode side. Co-57 was used because its lower-energy 122 keV gamma rays would primarily interact on the nearest surface of the detector rather than throughout the detector bulk. The results in Fig. 6.9 were expected when the detector

was irradiated from the pixelated anode side. The pixel waveforms show an abrupt rise from the baseline and the planar waveforms have minimal amplitude, which imply the recorded events are truly anode-side events.

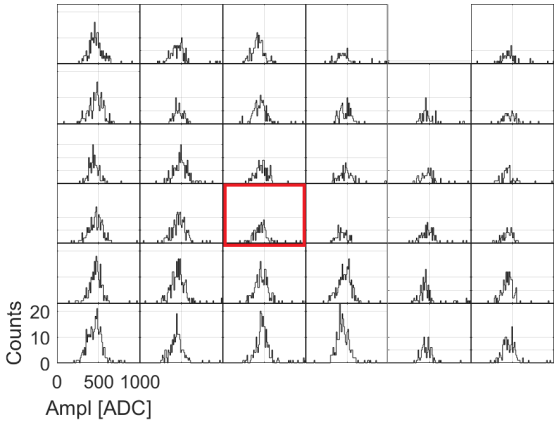

(a) Raw pixel spectra with Ch. 58 highlighted

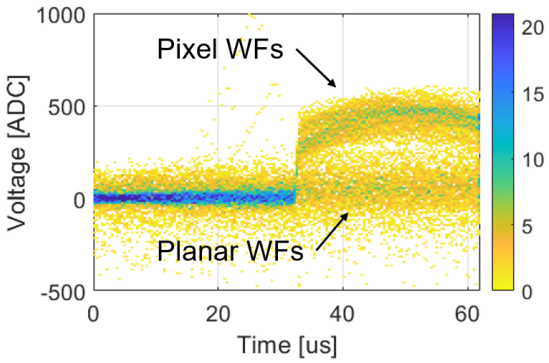

(b) Event waveforms from Ch. 58

Figure 6.9: Detector 193BS4-1 results with the VAD-UMv2.2 ASIC at -1000 V bias with a Co-57 check source irradiating the pixelated anode side.

When the detector was then irradiated from the planar cathode side, the results were unexpected. A total event count greater or at least similar to the anode-side test was expected, but Fig. 6.10a showed that far fewer events were recorded across all pixels. Cathode-side event waveforms where the pixel and planar waveforms have similar amplitudes were expected, but Fig. 6.10b showed event waveforms that more closely resemble anode-side events than cathode-side events. The cathode-side irradiation result showed that even with this source position, only near-pixel events were being recorded and near-cathode events were not being recorded.

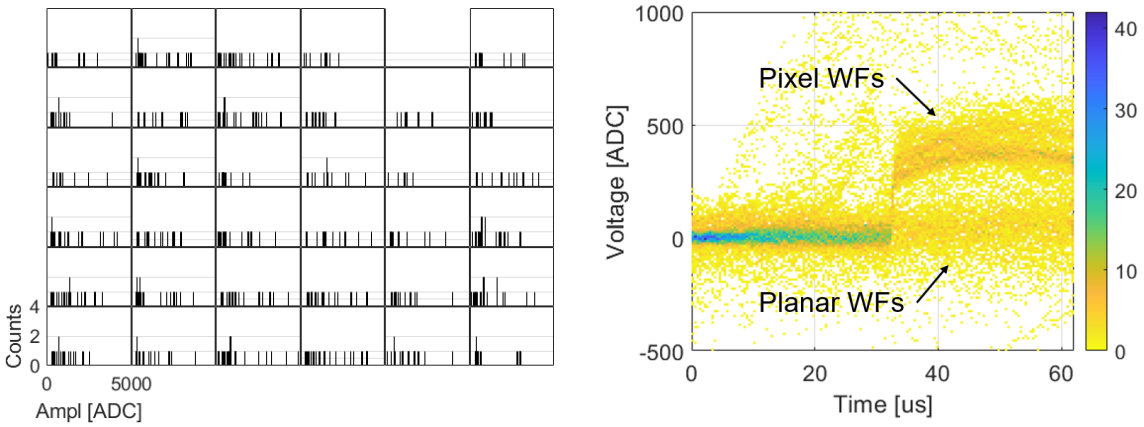

(a) Raw pixel spectra **(b) Event waveforms from all channels**

Figure 6.10: Detector 193BS4-1 results with the VAD-UMv2.2 ASIC at -1000 V bias with a Co-57 check source irradiating the planar cathode side.

To confirm that the detector was not preventing the recording of cathode-side events, it was also checked with an analog readout system. This system provided expected results in that, when irradiated from the cathode side, there were more counts and the 122 keV photopeak was observable, as seen in Fig. 6.11b. Pixel waveforms from this measurement also had the characteristics of true cathode-side events, as in the slow rise to a fast rise during electron cloud drift towards the pixel anode.

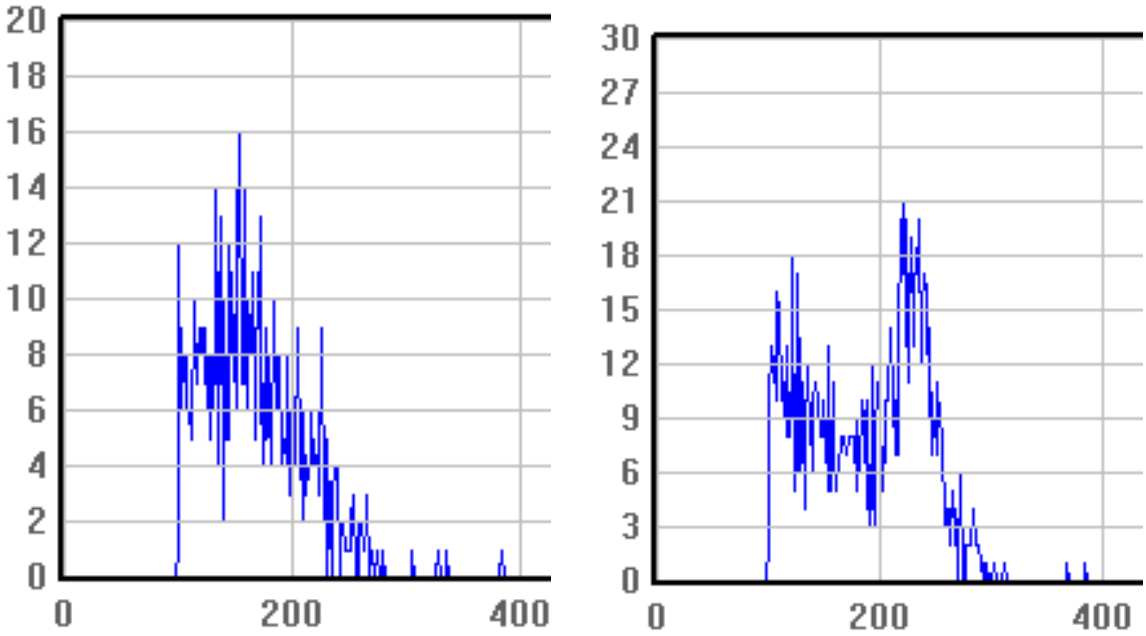

(a) Anode-side irradiation (b) Cathode-side irradiation

Figure 6.11: Detector 193BS4-1 total raw spectra for a subset of pixels in an analog readout system at -1000 V bias with a Co-57 check source. X-axes are pixel waveform amplitude in ADC by simple subtraction and y-axes are counts.

171AS5

This detector was tested quite extensively since it had a larger pixel array and had good performance, as seen in Fig. 6.12, like other detectors from ingot 171.

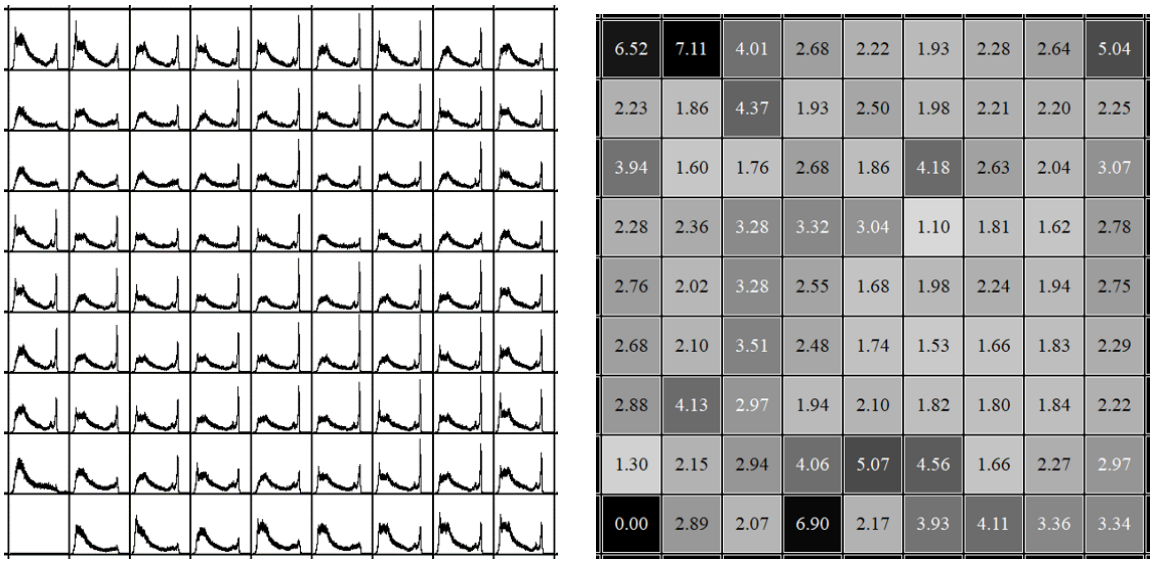

(a) Energy spectra **(b) Energy resolution**

Figure 6.12: Detector 171AS5 depth-corrected pixel results at -1504 V bias with a Cs-137 check source

The preamplifiers in the VAD-UMv2.2 ASIC were thought to have had a fixed shaping time of 500 ns, which could be too fast since pixel waveforms in TlBr could take as long as 10 μs to rise. In a conversation with Dr. Dirk Meier of IDEAS, it was found that the ASIC datasheets had some mislabels and that the preamplifiers were adjustable around 400 to 600 ns with a setting called "vfsf". Decreasing this value decreased the voltage at that input to the ASIC, which increased the preamplifier feedback resistance and increased the shaping time. An input of 1.5 V (of a 2.5 V maximum), had been used until this point, and photopeak counts increased from the anode towards the cathode as the input was decreased to 0.6 V, as seen in Fig. 6.13. No additional counts were gained at inputs below 0.6 V.

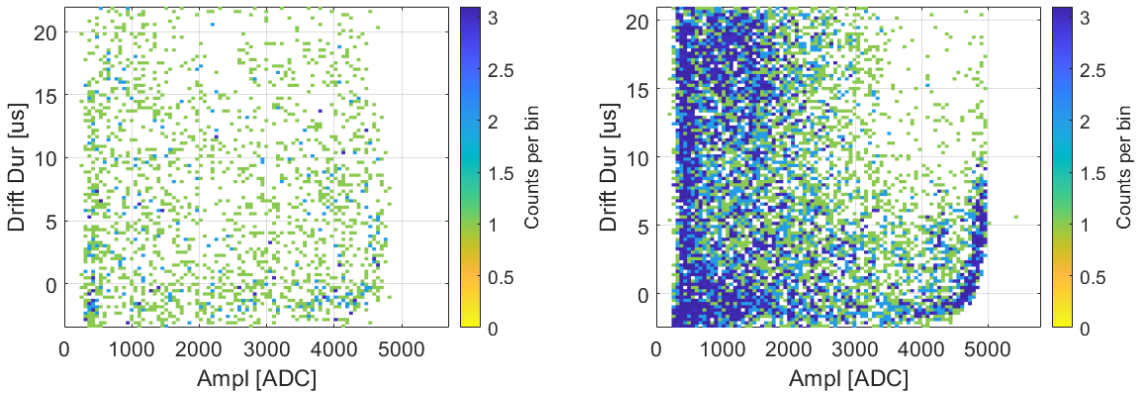

(a) Vfsf 2500, or 1.5 V **(b) Vfsf 1000, or 0.6 V**

Figure 6.13: Detector 171AS5 depth-gain curves results of an inner pixel (Ch 58) at -1500 V bias with a Cs-137 check source.

6.2.3 Dynamic Range

Once the "3 MeV" dynamic range setting started to be used after March 2022, trigger problems for events outside the near-pixel region were largely resolved and photopeak counts were observed throughout the bulk in good-performing pixels. Fig. 6.14 shows how changing only the dynamic range enabled better event data collection in some detectors. It is not understood how this change made such a difference and warrants further study.

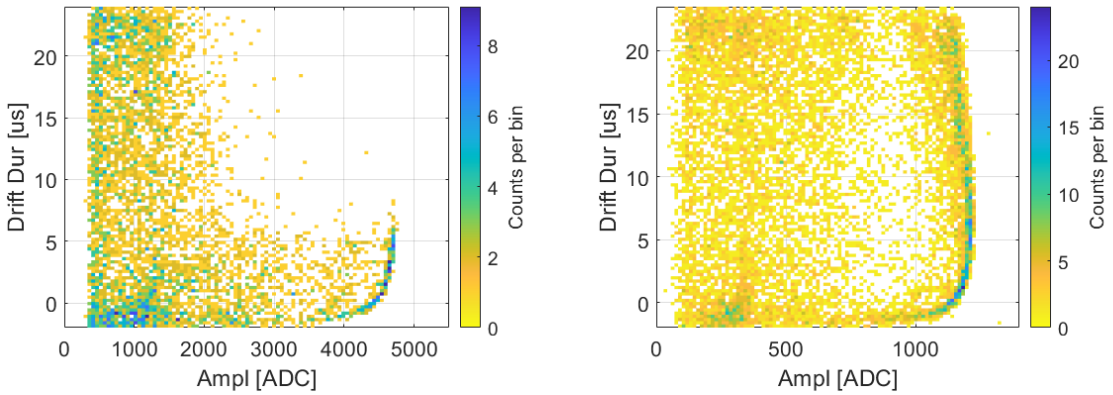

(a) "700 keV" **(b) "3 MeV"**

Figure 6.14: Detector 168CS2 depth-gain curves at different dynamic ranges from an inner pixel at -1500 V bias with a Cs-137 check source.

6.3 H3D S Series Systems

The H3D S Series is a commercially available gamma-ray spectrometer platform from H3D, Inc. While H3D manufactures it with CZT detectors, the platform is designed to be adaptable for use with any pixelated semiconductor detector with a similar physical footprint and characteristics.

6.3.1 935-38AS4 in S100X "Morrison"

This is one of the best performing detectors of all the detectors received from RMD, Inc.. All detectors made from this ingot seem to perform well. It also required a relatively high bias of -1500 V (3000 V/cm) to achieve its best performance, but its performance at -1000 V was still impressive, as seen in Figs. 6.15 and 6.16. Four pixels in the upper left corner were masked during measurement, and three pixels in the bottom center were masked during processing because they were dominating readout with electronic noise triggers. Although pixel masking decreases the efficiency of the detector, this shows how the detector can still be effective even if portions of the detector are not usable.

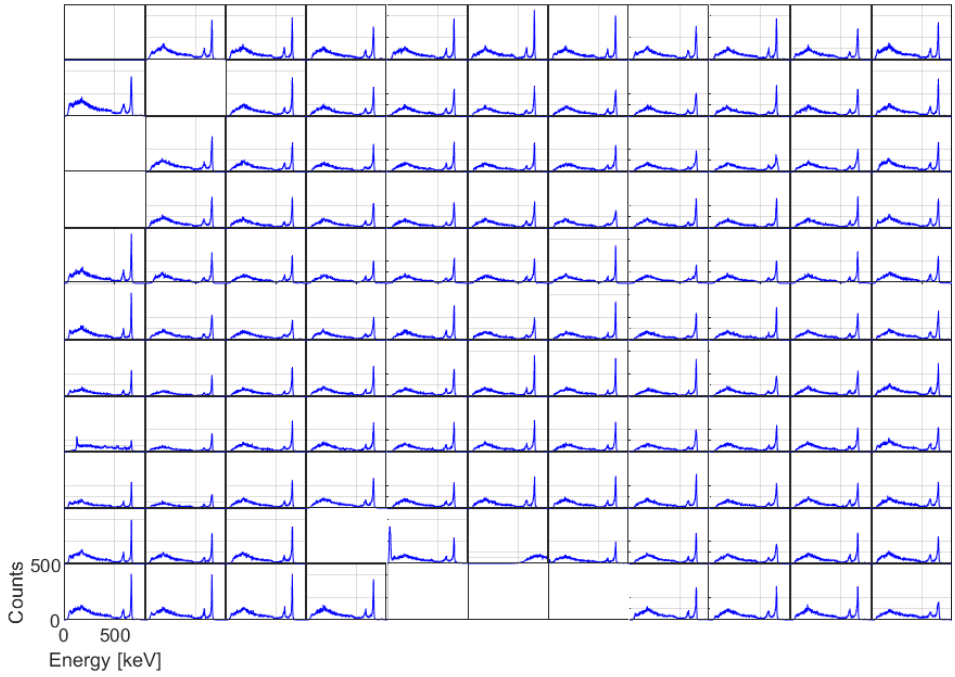

Figure 6.15: Detector 935-38AS4 depth-corrected pixel spectra with the Orion Solo at -1000 V with a Cs-137 check source

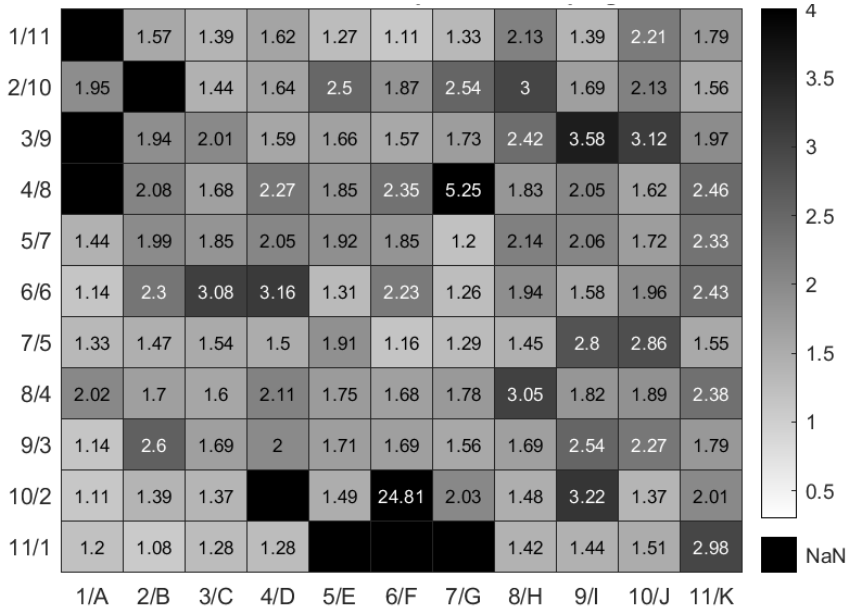

Figure 6.16: Detector 935-38AS4 depth-corrected pixel resolution [FWHM %] with the Orion Solo at -1000 V with a Cs-137 check source.

This detector was selected for further use in the H3D S100X "Morrison". Its performance was not as good, likely because settings in the S Series were not optimized for TlBr. The sampling rate was fixed at 5 MHz, which is too fast for this setup but could be adjusted later by H3D. The depth of interaction was calculated with the cathode-to-anode ratio, which gives a less precise waveform amplitude for these TlBr detectors. Despite these settings, it was still able to achieve 2.9% FWHM at 662 keV with a best pixel of 1.8% FWHM, as seen in Figs. 6.17 and 6.18.

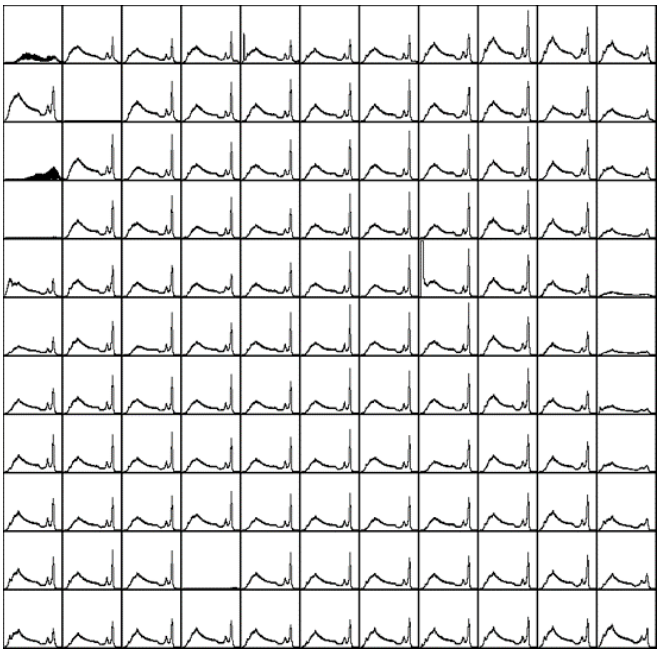

Figure 6.17: Detector 935-38AS4 depth-corrected pixel spectra with "Morrison" at -999 V with a Cs-137 check source

13.85	2.81	2.55	2.48	3.50	3.05	2.85	4.67	2.73	3.95	5.61
4.73	5.32	2.53	2.68	2.78	2.89	2.81	4.43	3.77	3.98	2.04
12.93	2.89	2.36	2.73	2.52	2.95	2.34	2.60	2.54	3.27	2.53
9.20	3.27	2.34	2.37	3.52	2.27	2.27	2.48	2.81	3.49	1.86
3.68	3.69	3.63	3.91	2.88	2.09	2.63	2.35	3.33	4.42	6.36
3.10	3.53	2.17	3.17	2.15	1.75	2.27	1.96	3.53	3.70	4.89
3.76	2.74	2.81	2.31	2.99	2.08	2.14	2.68	2.63	3.96	2.68
2.84	2.60	2.17	2.71	2.79	2.09	2.69	3.34	3.00	3.35	3.95
3.26	2.97	2.69	2.51	2.49	2.51	2.80	3.13	2.83	3.18	4.00
3.03	2.12	2.56	0.00	2.61	2.33	2.97	3.08	2.57	2.99	5.37
4.08	3.30	3.42	3.91	3.92	3.23	3.00	3.63	3.26	3.44	1.60

Figure 6.18: Detector 935-38AS4 depth-corrected pixel resolution [FWHM %] with "Morrison" at -999 V with a Cs-137 check source

6.3.2 Performance with Various Isotopes: S100X "Alger"

With minimal adjustment for TlBr, the S Series systems are able to produce recognizable spectra for photons from 59 keV to 2.6 MeV, as seen in Fig. 6.19. These spectra were produced with only single-pixel events, so the higher energy photopeaks like those from Co-60 and Th-228 would benefit from including multi-pixel events. Fully optimizing the system for TlBr may produce better results as well.

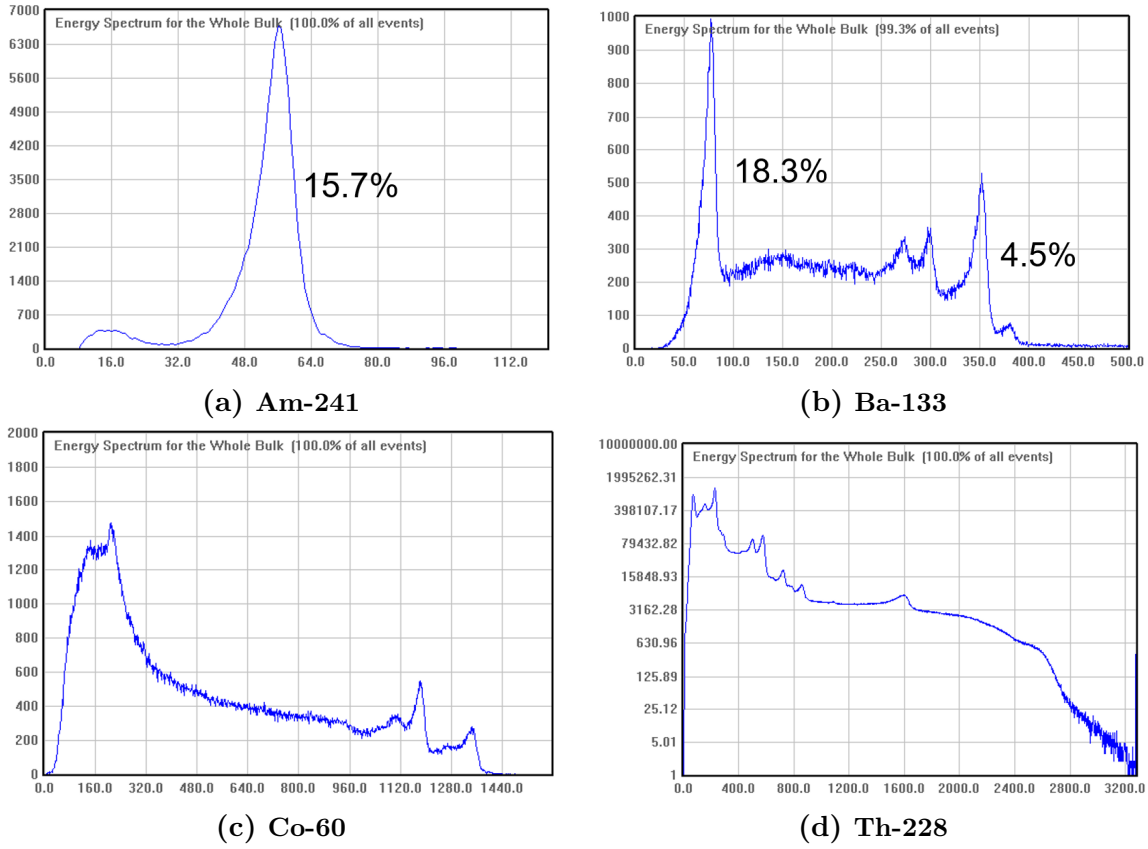

(a) Am-241

(b) Ba-133

(c) Co-60

(d) Th-228

Figure 6.19: Detector 171AS5 depth-corrected total spectra from H3D S Series "Alger" at -1504 V bias. X-axes are event energy in keV and y-axes are counts. All count axes are linear except for Th-288's which is logarithmic.

6.3.3 Detector 212AB1 and S200X "Allegan"

Detector 212AB1 was another large detector with great performance, as seen in Figs. 6.20 and 6.21.

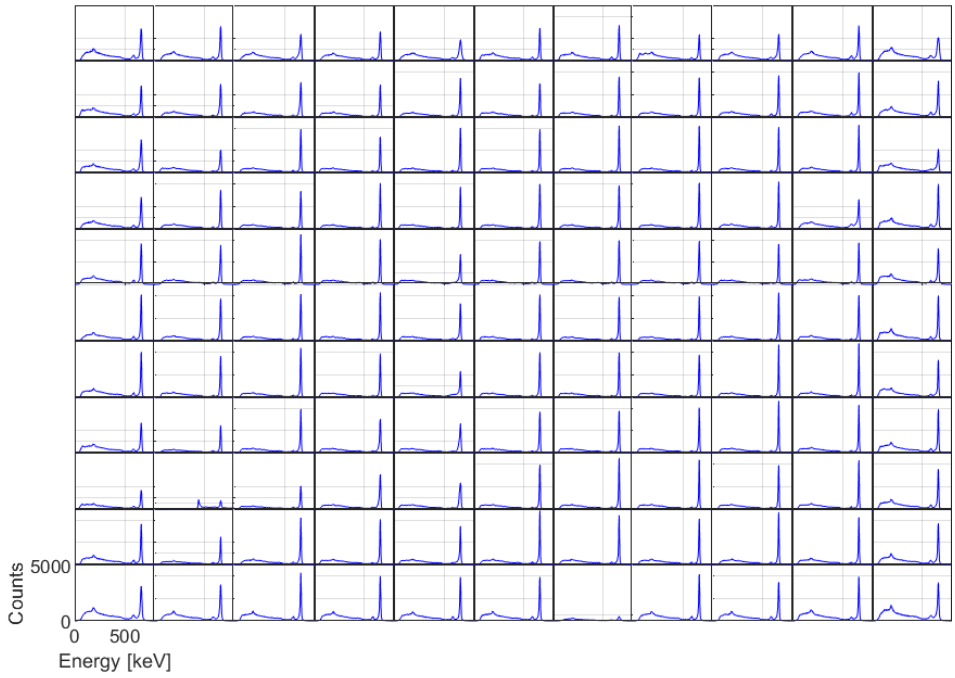

Figure 6.20: Detector 212AB1 depth-corrected pixel spectra with the Orion Solo at -1000 V with a Cs-137 check source

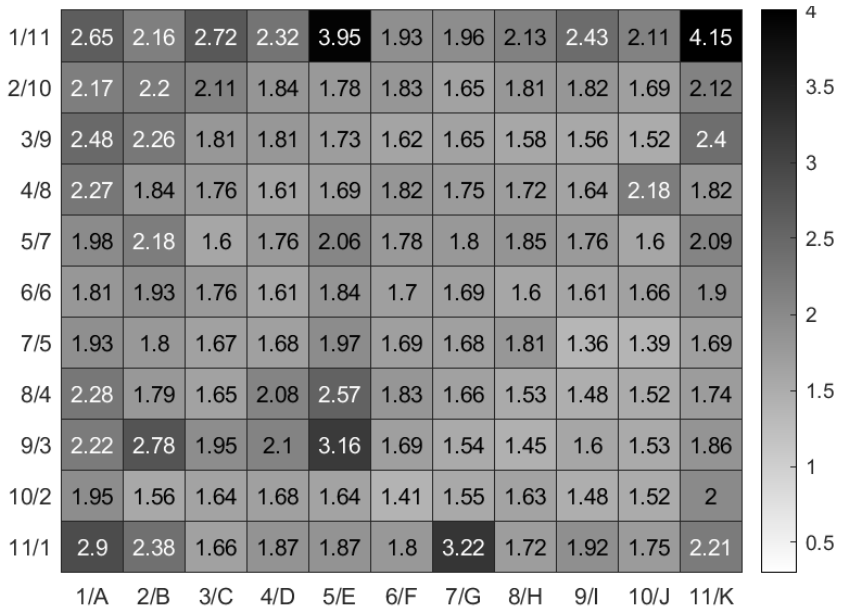

Figure 6.21: Detector 212AB1 depth-corrected pixel resolution [FWHM %] with the Orion Solo at -1000 V with a Cs-137 check source.

S200X "Allegan" was populated with Detector 212AB1 and another large detector, 203BS2(R). This system was tested with Ba-133, Cs-137, and Co-60 in order to have a range of photopeaks from 80 to 1332 keV. The response was found to be highly linear, as seen in Fig. 6.22.

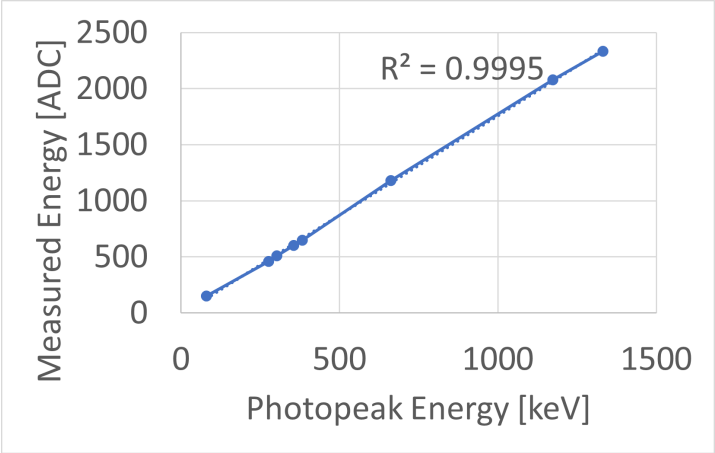

Figure 6.22: S200X Allegan energy response linearity

The intrinsic photopeak efficiency of Detector 212AB1 also agrees with the simulated findings by Hussain et al.[51]. Efficiency was measured using only single-pixel events, which may explain why the experimental result was lower than simulation. The 80 keV peak of Ba-133 was omitted because Allegan's hardware threshold was too high, so some peak counts were lost, affecting its efficiency calculation.

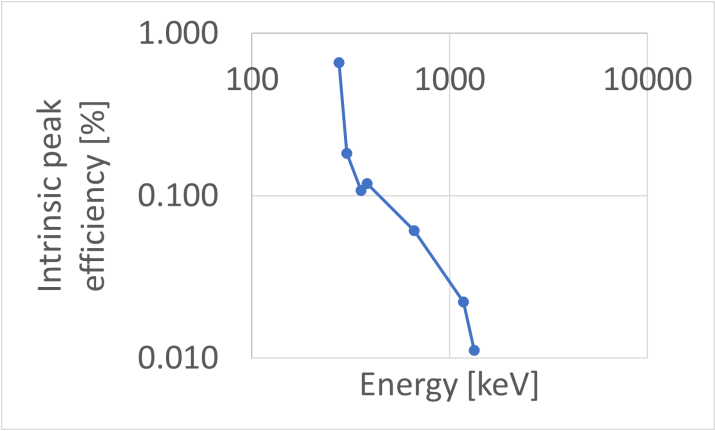

Figure 6.23: Detector 212AB1 intrinsic peak efficiency linearity

6.4 "Double-peaking" and the Cathode "Pixel" Pattern

6.4.1 212BS2(x)

212BS2

This detector had "double-peaking" in its spectra immediately upon arrival at UM. Fig. 6.24 shows how the Cs-137 photopeaks are broad with a poor resolution, or they seem to show a "double" photopeak, or the photopeak has a significant high-energy tail. Simple subtraction was used to determine the signal amplitude in order to make the "double-peaking" clearer.

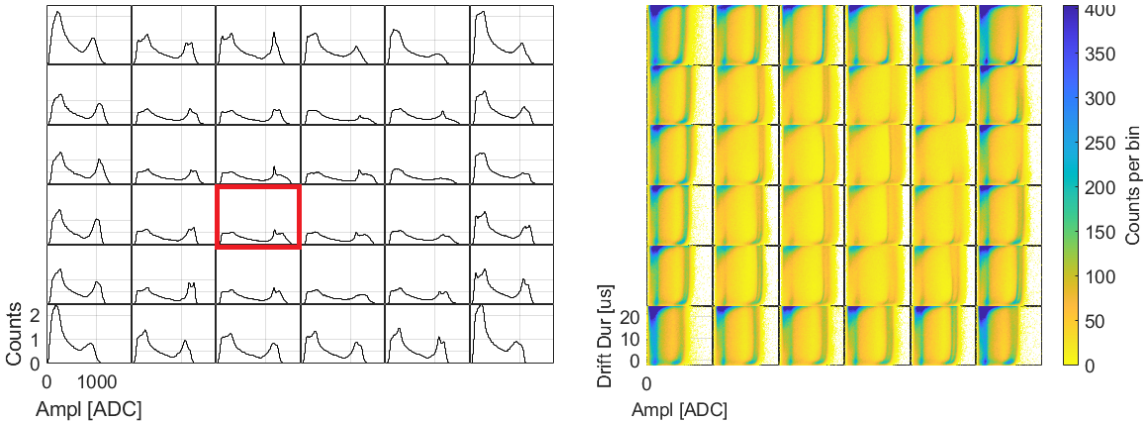

(a) Raw spectra, with Ch 58 highlighted. **(b) Depth-gain curves**

Figure 6.24: Detector 212BS2 results at -1000 V with a Cs-137 check source. Amplitude by simple subtraction.

The cause of counts in a second peak or high-energy tail are due to an event waveform tail that continues to slowly rise after electron cloud collection, as seen in Fig. 6.25. The cause of the events seem to be similar to the high-energy tailing observed by Dr. William Koehler.[52]

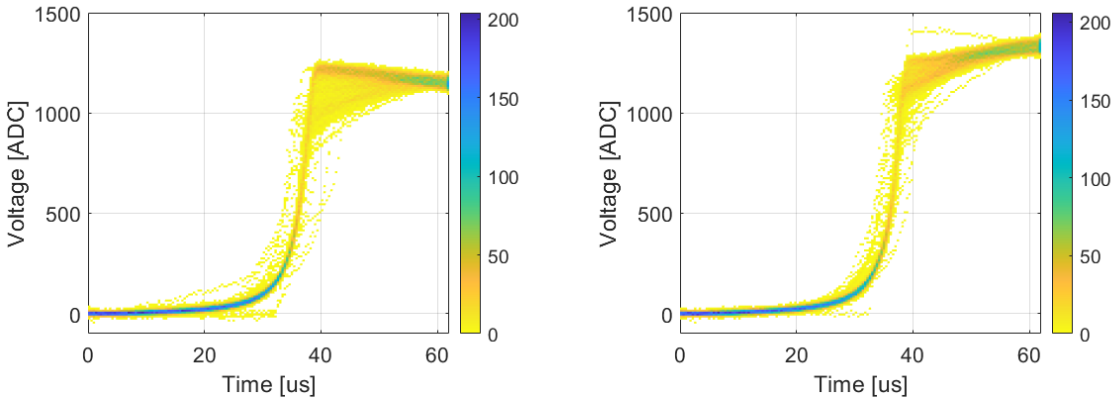

(a) From the low-energy peak **(b) From the high-energy peak**

Figure 6.25: Detector 212BS2 photopeak event pixel waveforms from Channel 58 at -1000 V with a Cs-137 check source

This detector developed the "cathode pixel pattern" during operation at UM, as seen in Fig. 6.26b.

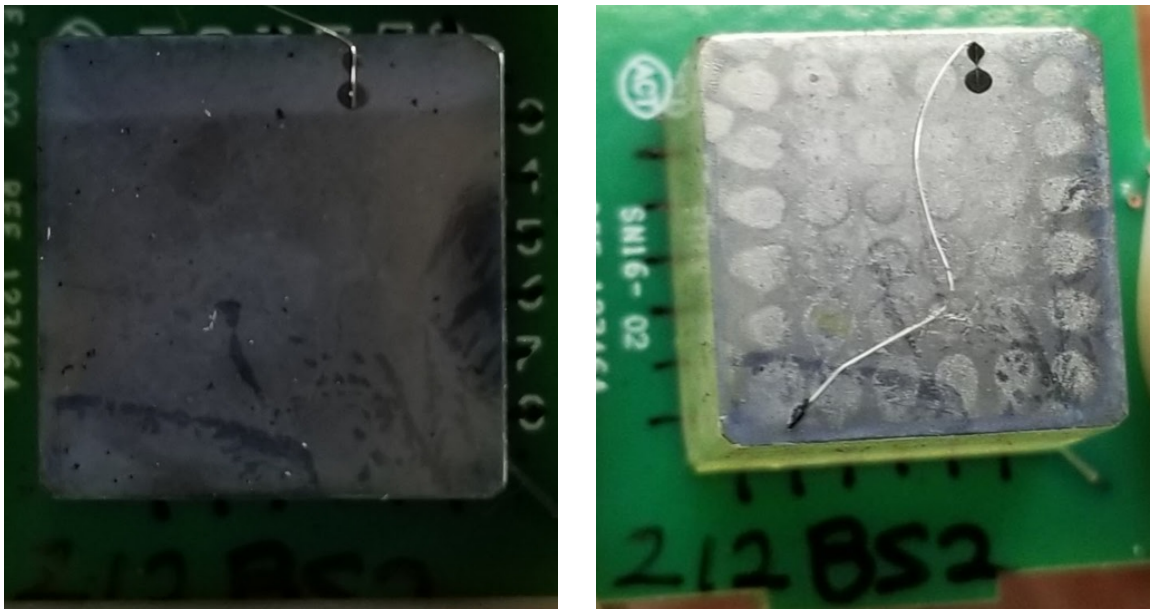

(a) March 3, 2022, after arrival at UM **(b) May 13, 2022**

Figure 6.26: Detector 212BS2 cathode

212BS2(R)

Electrodes were refabricated to attempt to stop the "double-peaking" phenomenon. Fig. 6.27b shows that "double-peaking" was reduced in most pixels. However, most pixels have a high-energy tail as well as a poor full-width-at-tenth-maximum (FWTM) resolution. The FWTM resolution is so poor that the thallium escape X-ray peak cannot be resolved from the photopeak. This shows that the "double-peaking" is likely caused by material diffusing into the detector crystal bulk. If this detector were operated longer, it would likely start to show "double-peaking" again.

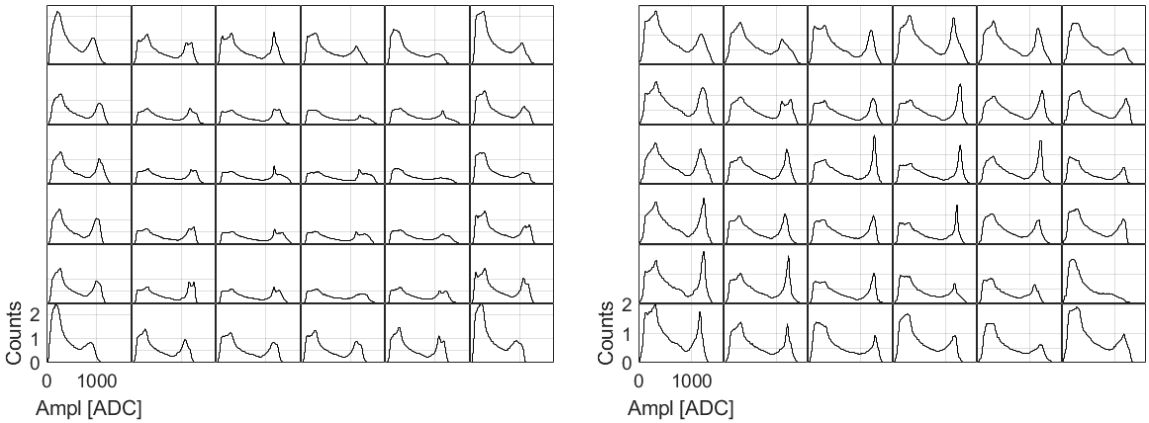

(a) 212BS2 **(b) 212BS2(R)**

Figure 6.27: Detector 212BS2(x) raw spectra at -1000 V with a Cs-137 check source. Amplitude by simple subtraction.

6.4.2 212BS3

This detector also showed "double-peaking" immediately upon arrival, as seen in Fig. 6.28, similar to Detector 212BS2. This phenomenon persisted during all measurements.

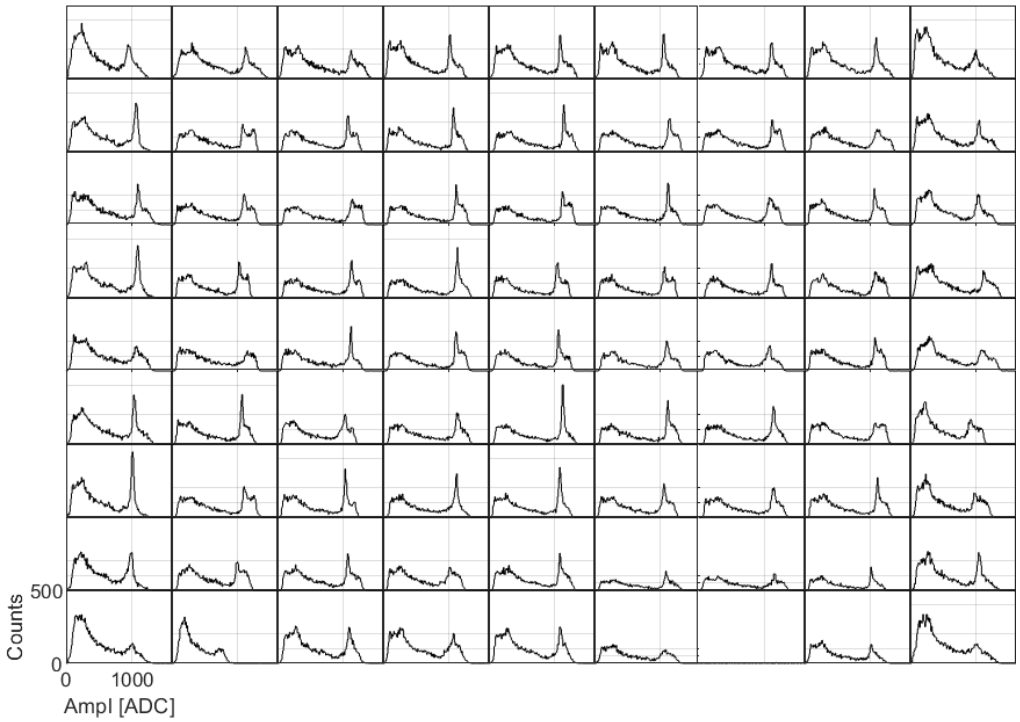

(a) Raw spectra

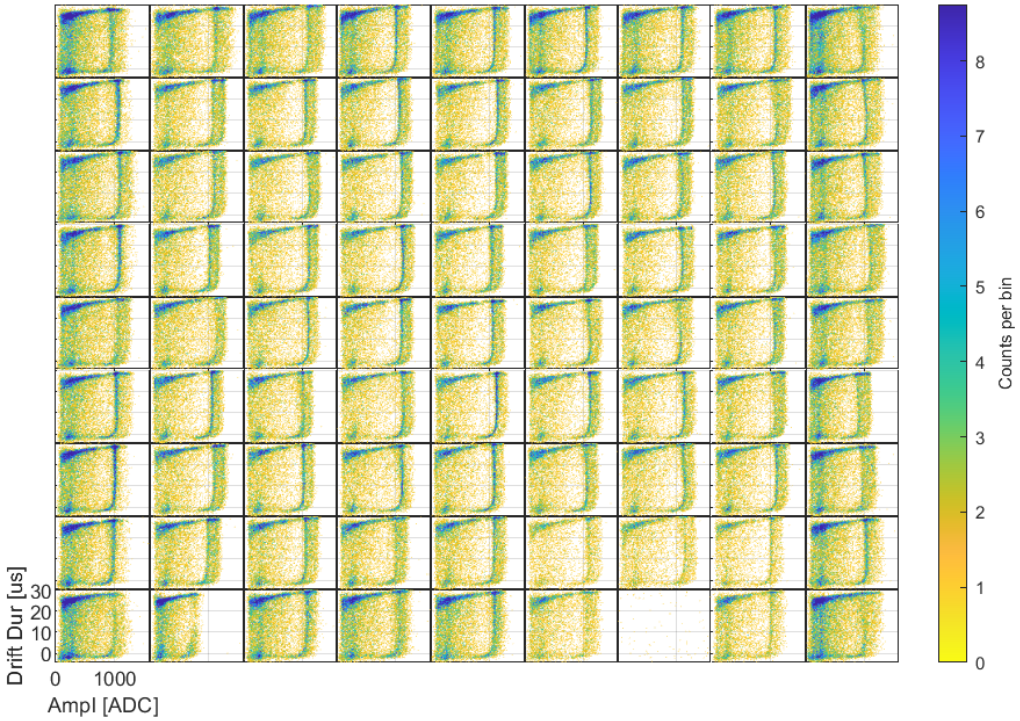

(b) Depth-gain curves

Figure 6.28: Detector 212BS3 results at -1000 V with a Cs-137 check source. Amplitude by simple subtraction.

On arrival, this detector had a clean, mirror-like cathode, as seen in Fig. 6.29a. A piece of electromagnetic interference (EMI) shielding was used to connect the readout system's high-voltage distribution board to the detector cathode. This EMI shielding consisted of foam surrounded by a conductive metal mesh and some conductive adhesive to affix the shielding. In Fig. 6.29b, a mesh-like pattern can be seen "burned" into the cathode. It is possible that natural finger oils from bare hands manipulating the foam may have contributed to this reaction. By the last measurement, the foam "burn" had mostly disappeared, although that area looked rough and weakened, and a pixel-like pattern had appeared, as seen in Fig. 6.29c. Examining the materials present on the electrodes at this point would help determine the cause.

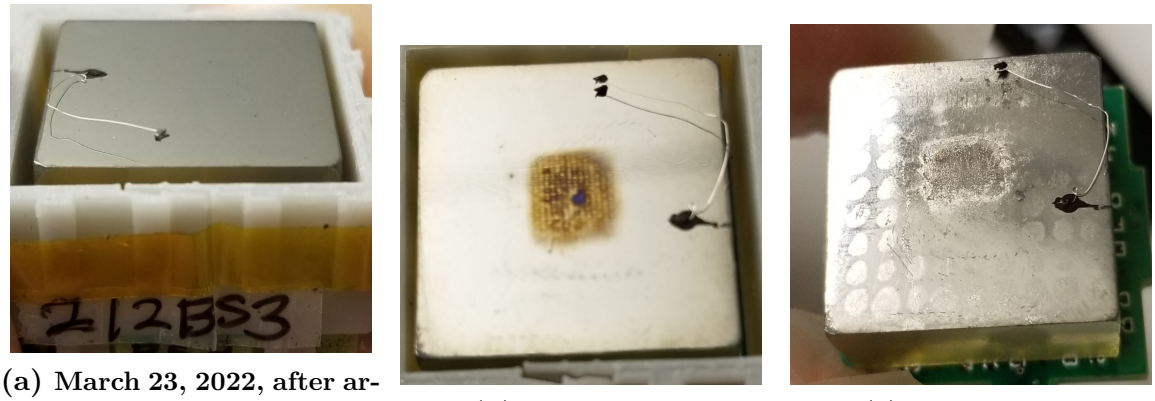

(a) March 23, 2022, after arrival at UM **(b) May 9, 2022** **(c) June 1, 2022**

Figure 6.29: Detector 212BS3 cathode

6.4.3 186BS5

This detector shows an interesting physical characteristic that was present in many, if not all, of the tested detectors. When observing the pixelated anode through the translucent bulk, it is possible to see a "dot" shape on each square pixel, as seen in Fig. 6.30. Each "dot" shape probably correlates with the silver epoxy used to bond the detector crystal's pixels to its carrier board. However, because the epoxy is between the carrier board and the pixel, it is not expected to see such a shape at the interface between the pixel and the detector bulk. This implies that either chemical reaction or material migration is happening between the carrier board's pixel pad and the detector bulk.

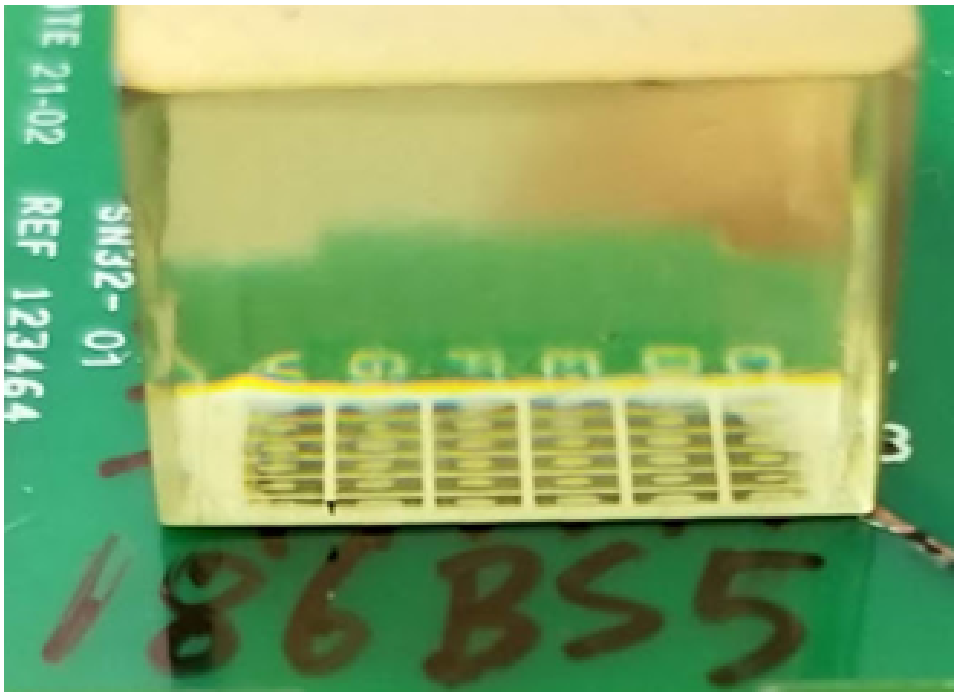

Figure 6.30: Detector 186BS5, with a "dot" shape on each pixel electrode, visible through the bulk

6.4.4 171AS5

This detector had the most extreme example of the cathode "pixel pattern". On arrival at UM, it had a generally smooth and even cathode, as seen in Fig. 6.31a. However, after 16 months of intermittent testing and study, the phenomenon that caused the pattern had completely separated the cathode material from the detector in a number of "pixel" spots, as seen in Fig. 6.31b. In this figure, the detector crystal is backlit, so that light is shining through detector bulk and the "pixel" holes in the cathode, towards the viewer.

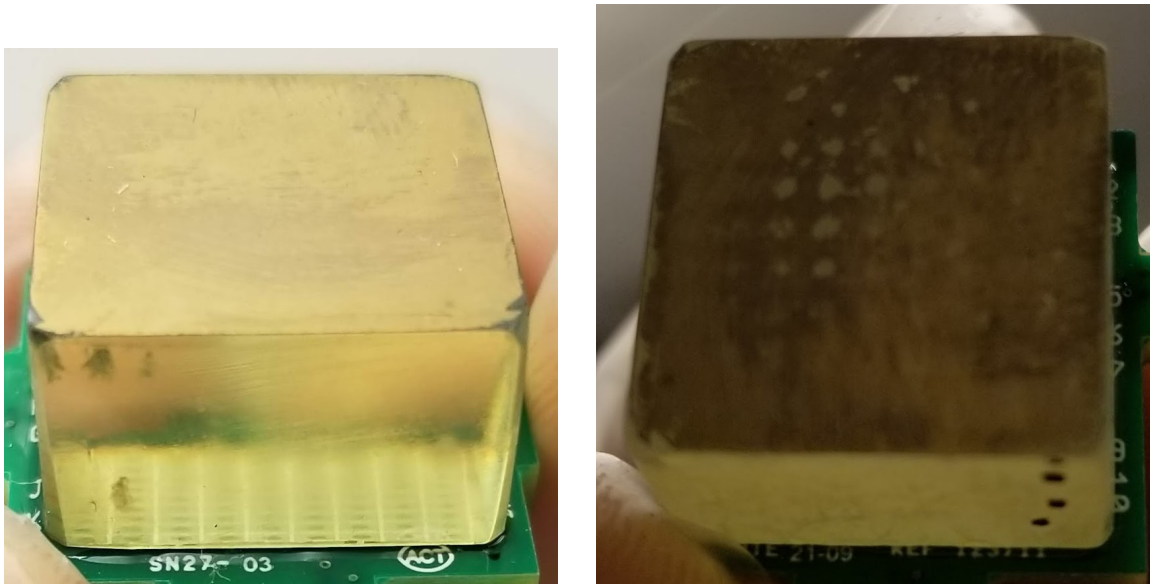

(a) October 1, 2021, after arrival at UM. **(b) February 1, 2023**

Figure 6.31: Detector 171AS5 cathode

6.4.5 185DS3

This detector was peculiar in that it never developed a pixel-like pattern on the planar cathode, as seen in Fig. 6.32, even though it had been operated for more than 50 cumulative days. It also had poor performance and noticeable trapping throughout the bulk. It would be interesting to determine if this detector's unique platinum electrodes were diffusing through the bulk due to operation. The consistent performance, although poor, warrants further investigation of this configuration.

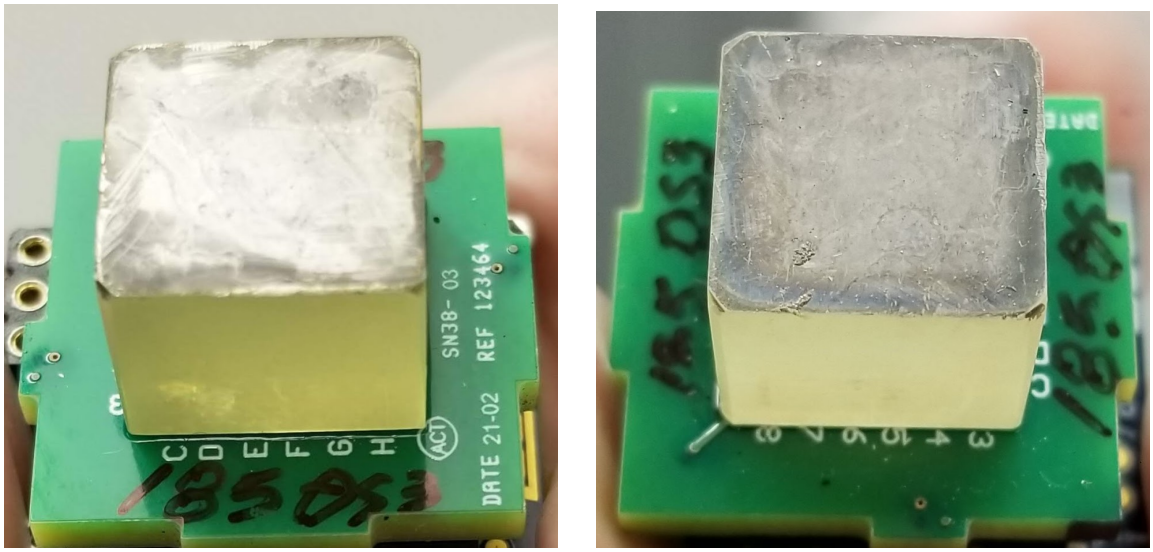

(a) Start of operation in Jun 2021 **(b) After last operation in July 2023**

Figure 6.32: Detector 185DS3 planar cathode

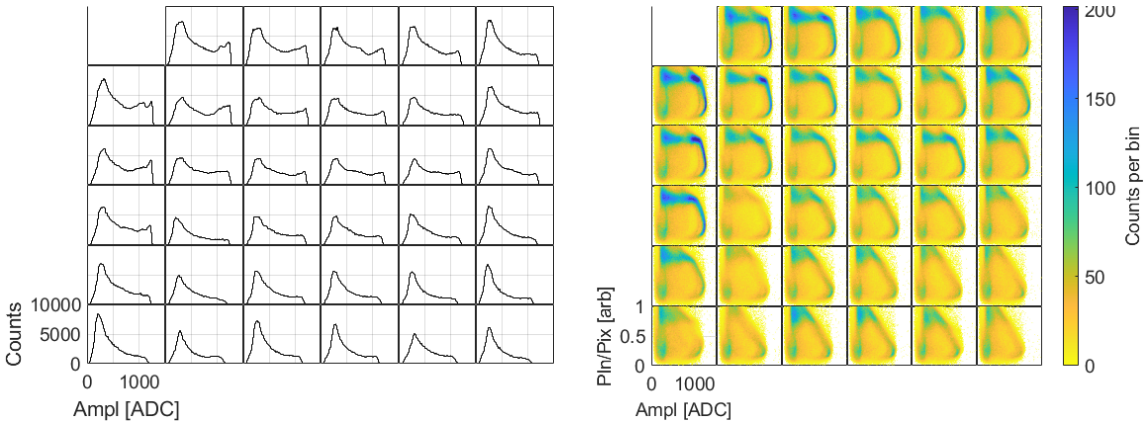

(a) Raw energy spectra **(b) Depth-gain curves**

Figure 6.33: Detector 185DS3 pixel results at -1000 V with a Cs-137 check source. Depth by cathode-to-anode ratio.

6.4.6 168CS2

This was the only other detector that never developed a pixel-like pattern on the planar cathode, as seen in Fig. 6.34c. However, it had a similar electrode configuration to many other tested detectors. It also had a temporary physical change occur along the

outer edge of the planar cathode during the course of the measurements, as seen in Fig. 6.34b. Additionally, a dark impurity was visible inside the bulk after it arrived at UM, as seen in Fig. 6.34a. This impurity did not appear to have an effect on event readout, although performance was not good enough to make a confident assessment, as seen in Fig. 6.35. The impurity was in or near Pixel D6. It is possible that a piece of dark material on the cathode in Fig. 6.34c was the result of part of that impurity migrating out to the cathode during operation, but it needs further investigation.

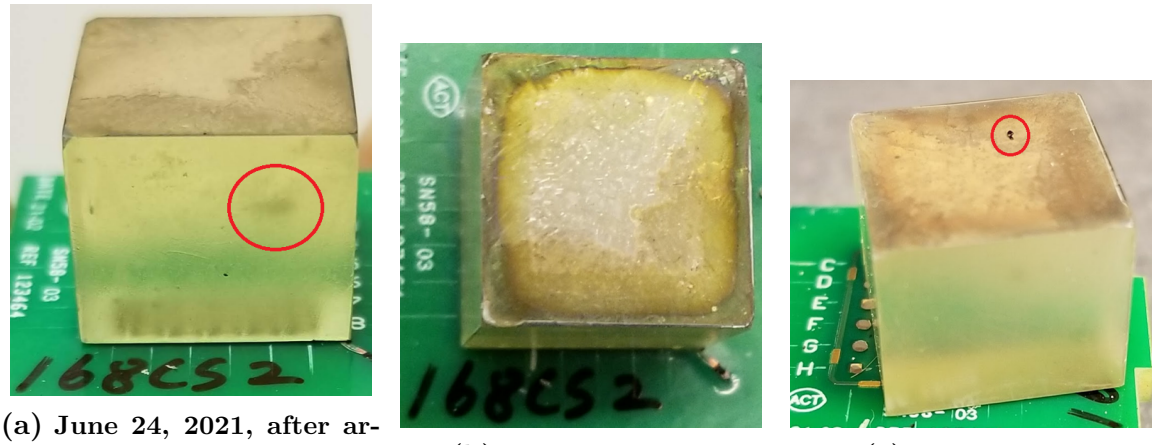

(a) June 24, 2021, after arrival.

(b) March 28, 2022

(c) May 9, 2022

Figure 6.34: Detector 168CS2

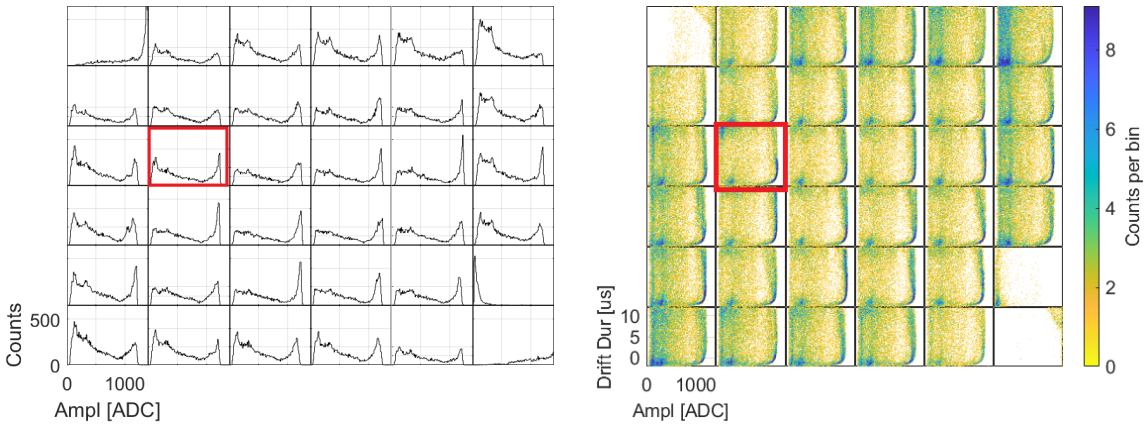

(a) Raw energy spectra

(b) Depth-gain curves

Figure 6.35: Detector 168CS2 pixel results at -2500 V with a Cs-137 check source. Pixel D6 is highlighted red.

6.5 H3DD-UM ASIC

This ASIC was better suited to thick TlBr with its eight user-selectable gain settings, its longer 256-cell sampling pipeline, and its four user-selectable trigger shaping times from 0.5 to 2 μs. Each version had a fixed preamplifier time constant, but that signal decay could be deconvolved before further signal processing. The H3DD-UM's slowest sampling rate of 1.5625 MHz functioned reliably, but 3.125 MHz was typically used since the sampling pipeline was longer.

6.5.1 212CS2

This detector was the first to be tested with the H3DD-UMv4 ASIC. It had its best performance on the first day, as seen in Fig. 6.36. The sampling rate was too fast at 6.25 MHz, so complete near-cathode event waveforms could not be recorded. Since those events could not be reconstructed with an accurate depth, they were omitted from the top of the depth-gain curves in Fig. 6.36b

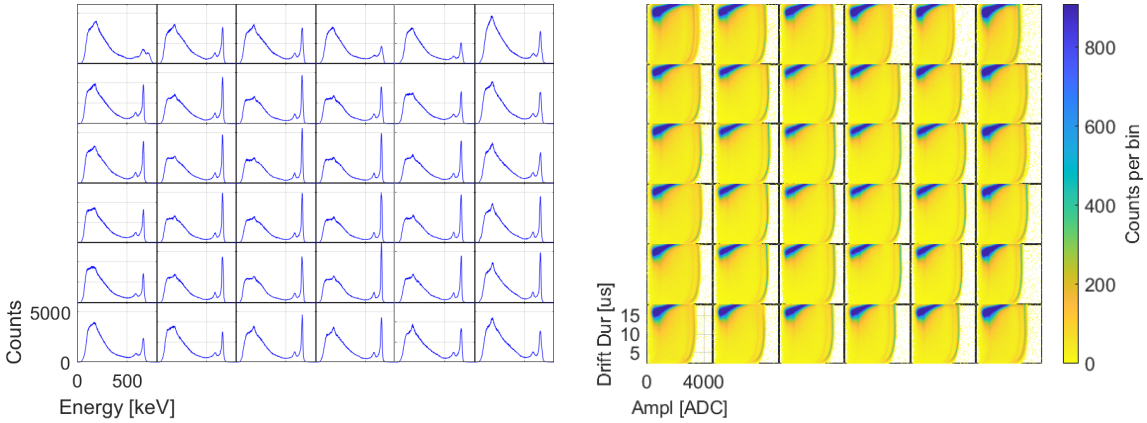

(a) Depth-corrected spectra **(b) Depth-gain curves**

Figure 6.36: Detector 212CS2 results at -1000 V with a Cs-137 check source

All the trigger shaper shaping times were tested on this new ASIC since the trigger shaper seems to be a problem on the VAD-UMv2.2 ASIC. Photopeak events were recorded at all available depths at all four shaping times, as seen in Fig. 6.37. The difference between shaping times was that longer shaping times recorded more low-energy events. Longer shaping times should improve photopeak resolution. At a longer shap-

ing time, a multi-pixel event with a low-energy component is more likely to be correctly categorized as a multi-pixel event. At a shorter shaping time, that low-energy component of a multi-pixel event may fail to meet trigger threshold, causing the event to be incorrectly categorized with one less pixel than is correct. The other finding is that no trigger problems were observed at the 0.5 μs setting, which is similar to the trigger shaping time in the VAD-UMv2.2 ASIC. However, this is not a strong finding since the detector did not have much bulk trapping.

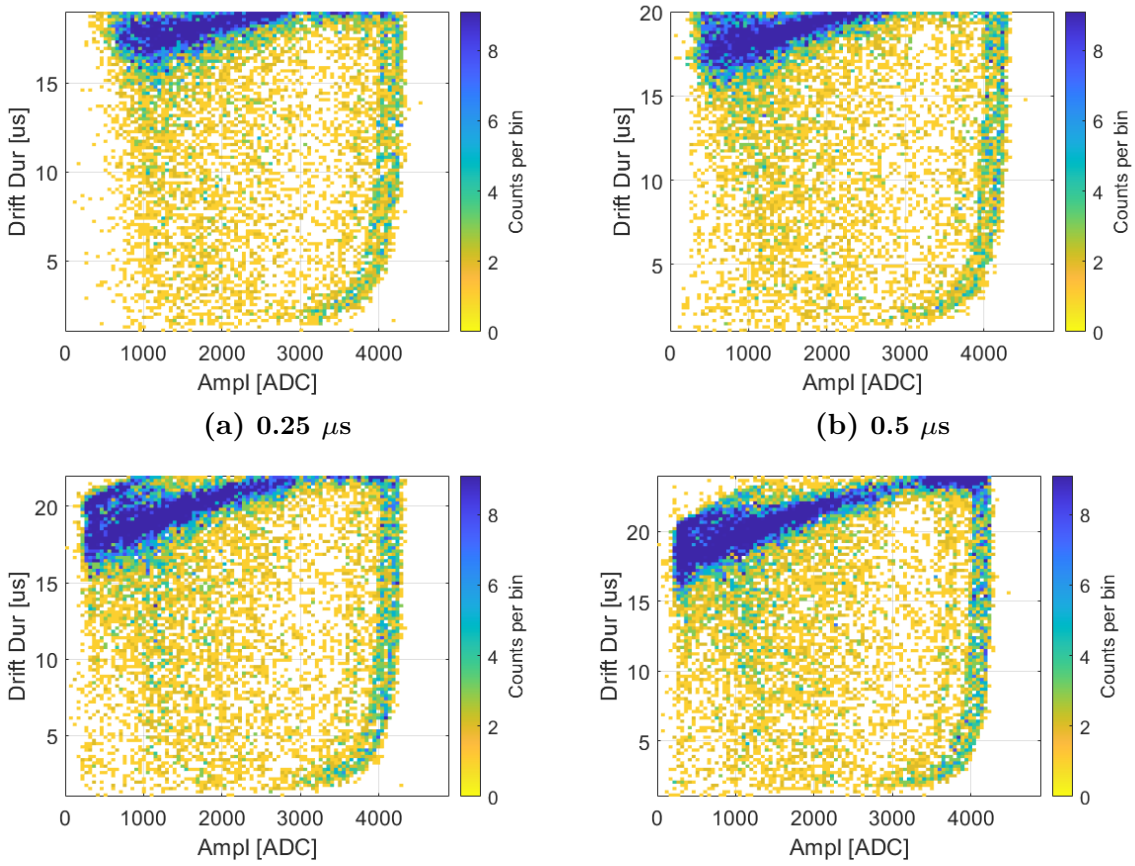

(a) 0.25 μs **(b) 0.5 μs**

(c) 1 μs **(d) 2 μs**

Figure 6.37: Depth-gain curve with each H3DD-UMv4 trigger shaper setting, using an inner channel (Ch 28) of Detector 212CS2 and a Cs-137 check source. Amplitude by simple subtraction.

This detector developed "double-peaking" in many pixels by the fourth day of operation, as seen in Fig. 6.38. Similar to other detectors, the higher-energy peak was due

to event waveforms that had a slowly rising tail rather than a flat tail. It has not yet been operated long enough to observe a cathode "pixel" pattern.

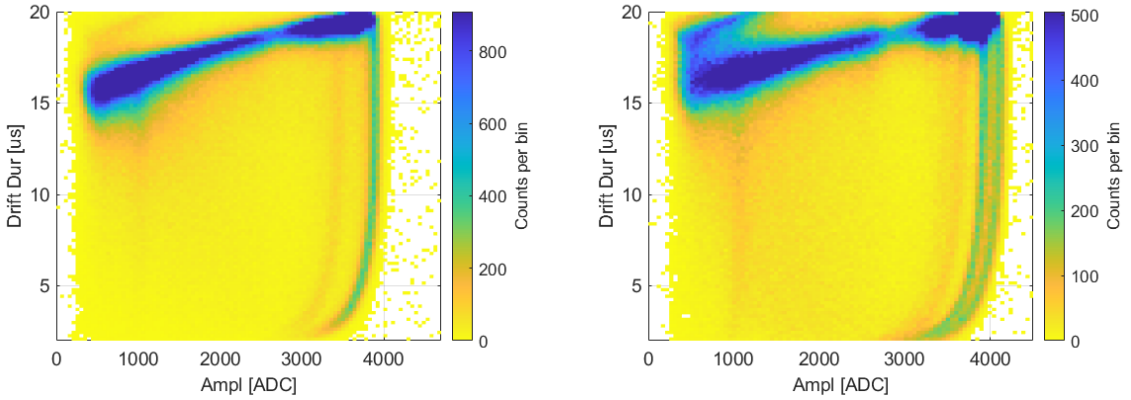

(a) First day (Mar 9) **(b) Fourth day (Mar 12)**

Figure 6.38: Detector 212CS2 depth-gain curves of an inner pixel at -1000 V with a Cs-137 check source. Amplitude by simple subtraction.

Fig. 6.39 shows that events from the lower energy peak occur mainly in the center of the pixel, whereas events from the higher energy peak occur mainly around the edge of the pixel.

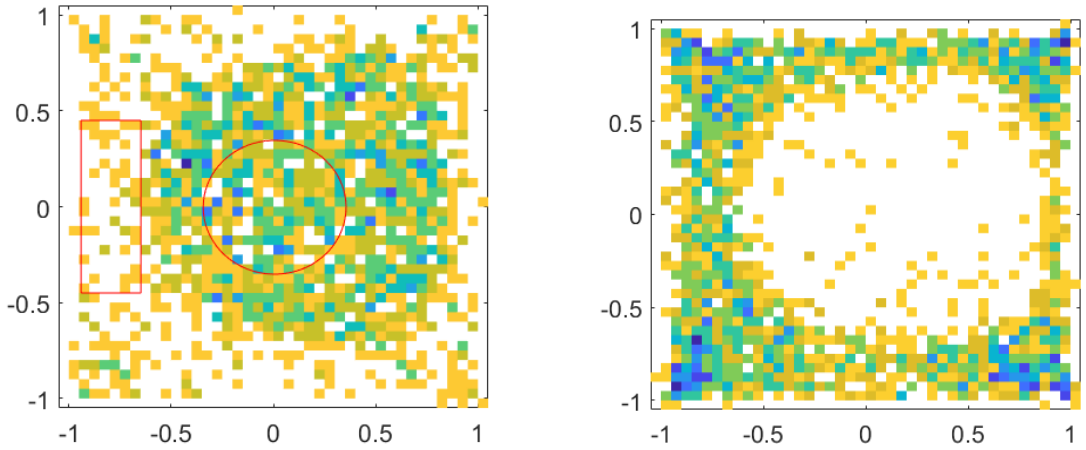

(a) Lower-energy peak events **(b) Higher-energy peak events**

Figure 6.39: Detector 212CS2 near-cathode photopeak event subpixel position in an inner pixel (Ch 76)

When looking at the average waveforms from a certain voxel and comparing the first day to the sixth day, as in Fig. 6.40, events from the subpixel center seem unchanged over time. However, by the sixth day, edge events had a faster rise during electron cloud drift and a rising waveform tail. This implies that events occurring near the pixel edges are subjected to less trapping, or more de-trapping. In other words, events occurring near the pixel edges have some extra electrons drifting through the bulk and contributing to the recorded signal, both during and after the electron cloud from the interaction has stopped moving. This seems consistent with Dr. William Koehler's findings on Auger recombination.[52] Holes from interaction events may be recombining with one double-trapped electron and releasing the other double-trapped electron into the valance band. These de-trapped electrons contribute extra signal to pixel waveforms, which lead to a second photopeak or high-energy tailing in energy spectra.

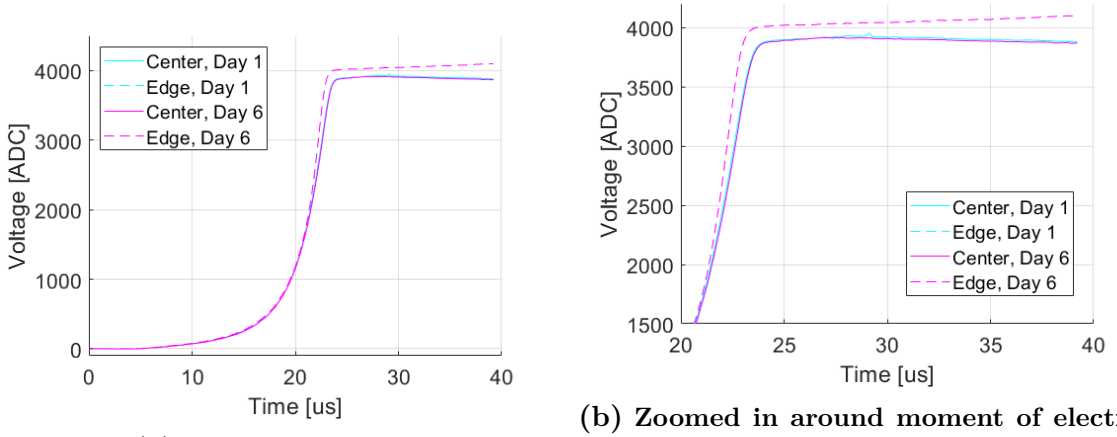

(a) Whole waveforms

(b) Zoomed in around moment of electron cloud collection

Figure 6.40: Detector 212CS2 average waveforms from a mid-depth voxel of Ch 76

6.5.2 Bonded with Carbon Nanotube Paste: 212AB2

In the silver-epoxy-bonded detectors, the silver is suspected to be diffusing into the crystal bulk and degrading event readout. Detector 212AB2 was bonded with carbon nanotube paste to attempt to counteract this effect. This detector did have relatively stable performance over a month of operation, as seen in Fig. 6.41.

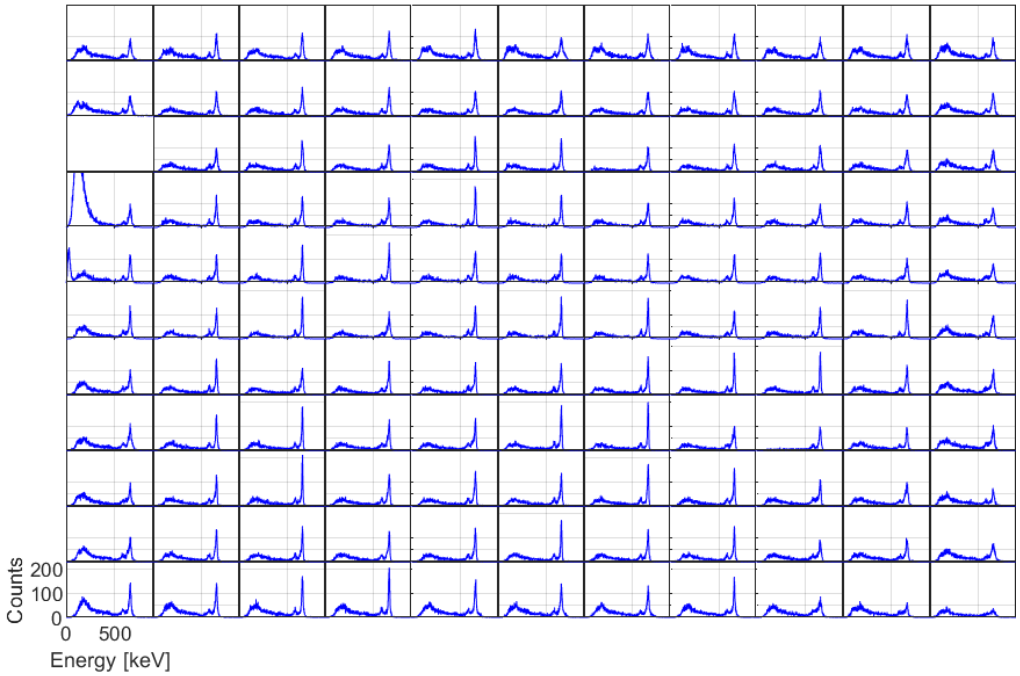

(a) Depth-corrected energy spectra

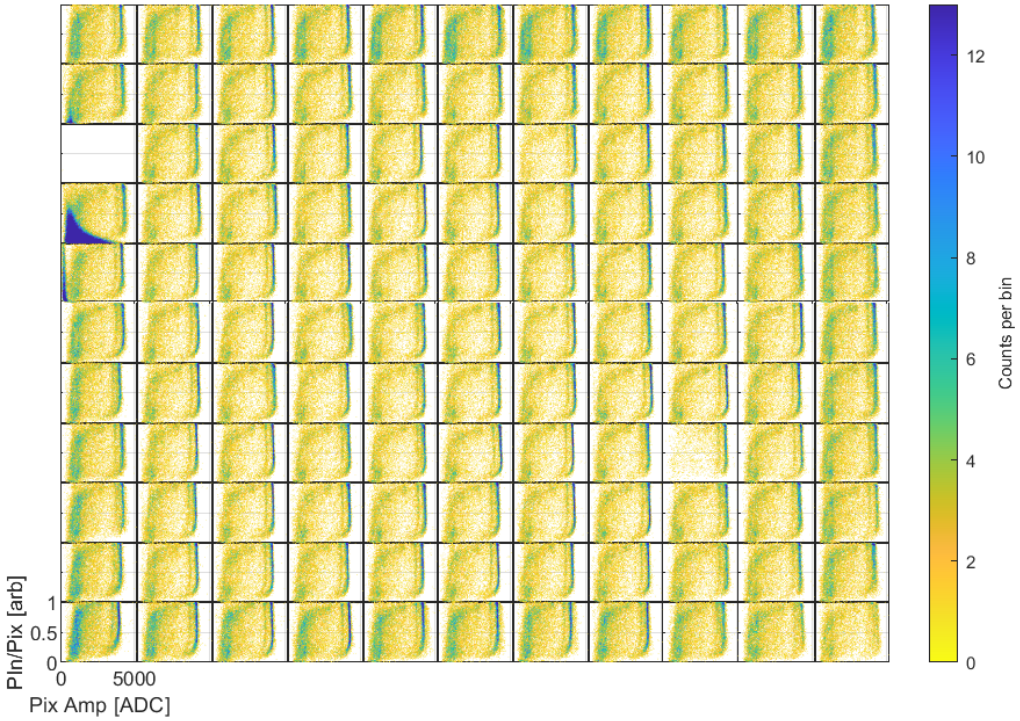

(b) Depth-gain curves

Figure 6.41: Detector 212AB2 results at -1000 V with a Cs-137 check source. Depth by cathode-to-anode ratio.

This detector did not develop "double-peaking" during its month of operation, but it may have started to develop a cathode "pixel pattern", as seen in Fig. 6.42. It developed a light black residue on the exposed portion of the cathode, but that may have just been dust from the lab air, since the readout system is not airtight. Lastly, "dot" shapes are visible between the bulk and the pixels, implying that some material is diffusing through the pixel anodes.

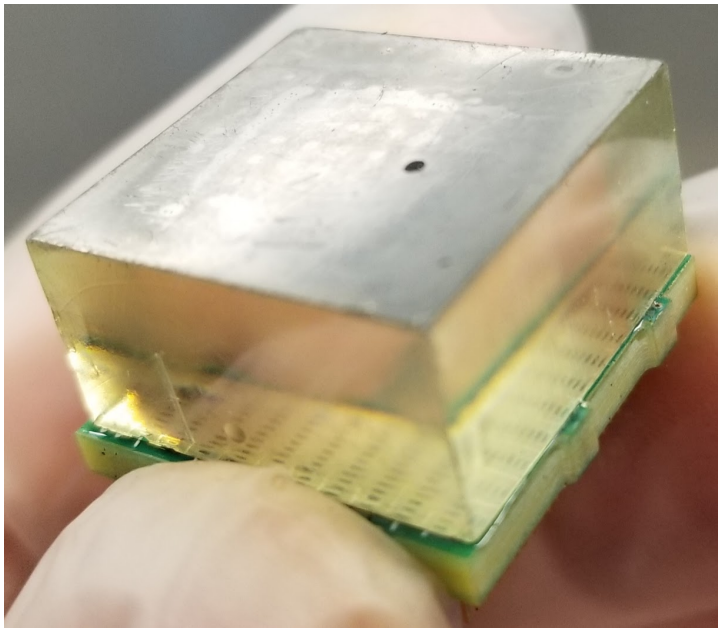

Figure 6.42: Detector 212AB2 cathode

6.6 Temperature Study

As stated earlier, thallium bromide's wider bandgap should enable it to work effectively at higher ambient temperatures than semiconductors with narrower bandgaps. This wider bandgap further prevents thermally excited electrons from reaching the conduction band and contributing to electronic noise during readout. This reduces the need for onboard cooling in a handheld detector system and thus reduces power consumption. The detector used in this study, 168CS2(R), showed a downward-shifting photopeak centroid when operating temperature increased above +20°C. It also showed repeatable performance when returned to +20°C or below.

Previous experiments have shown that increased operating temperature hindered readout of electron drift due to radiation interaction. Shoji et al. found that increasing the operating temperature from -60°C to +30°C increased the electron transit time through a TlBr sample.[53] Kostamo et al. found that increasing the operating temperature from -63°C to +32°C decreased TlBr resistivity from around 10^{14} Ω·cm to around 10^{10} Ω·cm.[54] Eduardo et al. found that temperatures above +3°C to +30°C proportionally induced random noise pulses sooner due to polarization and ambient humidity.[55] They also found with their colloidal carbon electrodes that capacitive-coupling the central readout anode significantly prevented greater carbon migration from central anode into the detector bulk compared to the ring anode that was directly-coupled to ground. Donmez et al. found no significant change from -15°C to 5°C, but that increasing the operating temperature to 10°C or 15°C significantly reduced single-pixel-event photopeak counts and induced a slight downward centroid shift to a 662-keV photopeak.[56] The decrease in peak counts and appearance of peaks at unexpected pulse heights in one pixel's raw spectra at 10°C and 15°C also imply that there may have been a non-uniform gain change with temperature across the pixel column.

In this experiment, Detector 168CS2(R) was tested from 0°C to +40°C, in both directions. The Cs-137 photopeak centroid experienced a downward shift with increasing temperature and vice versa, as seen in Fig. 6.43. This implies that there may have been fewer electrons drifting after each radiation interaction as the temperature rose. The downward shift from 0°C to +30°C was expected due to the ASIC's behavior at various temperatures, as found by Xia et al.[57]. However, the extra downward shift at +40°C must have been due to internal changes in the detector. This experiment also showed generally consistent and repeatable results when operating throughout the tested temperature range, as seen in Fig. 6.43, but more research is needed to determine long-term trends. One exception is the first two or three days of operation, where the detector was likely undergoing "conditioning" due to ionic movement. This detector had been resting in storage for over three weeks prior to this experiment. The photopeak shifted similarly at all depths with each temperature change, as seen in Fig. 6.44, so a change in bulk trapping is not a major cause of the photopeak shift. This further supports that there must be fewer electrons from a radiation interaction drifting at higher temperatures.

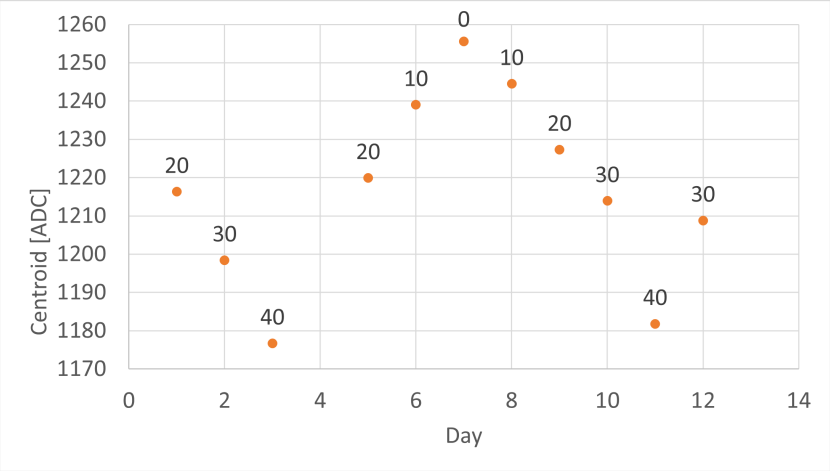

Figure 6.43: Detector 168CS2(R) photopeak centroid of an inner pixel (Ch 26) at various temperatures with a Cs-137 source. Data labels are environmental chamber temperatures in Celsius.

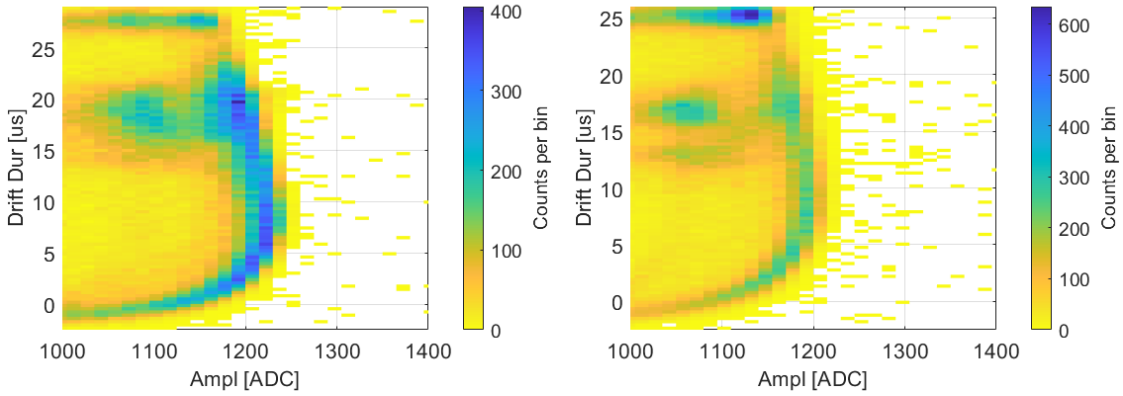

(a) 20°C **(b) 40°C**

Figure 6.44: Detector 168CS2(R) depth-gain photopeak curves from an inner pixel (Ch 66) at -1000 V with a Cs-137 check source.

Another notable finding is that preamplifier feedback time constant seemed to decrease noticeably at 40°C. The user feedback setting was the same across all temperatures, but Fig. 6.45b shows pixel waveforms tail with a quicker decay than at lower temperatures. The VAD-UMv2.2 ASIC was thermoelectrically cooled, but was left at the same setting across all temperatures. Extra cooling was not provided at higher temperatures. Various decay time constants from 150 to 400 μs were deconvolved from the waveforms, but no

single time constant was able to bring the photopeak centroids for each pixel and all pixels together on trend with their centroids from 0°C to +30°C. Changing preamplifier feedback seemed to have a role in the waveform decay, but it was not the only reason for the photopeak centroid shift with temperature.

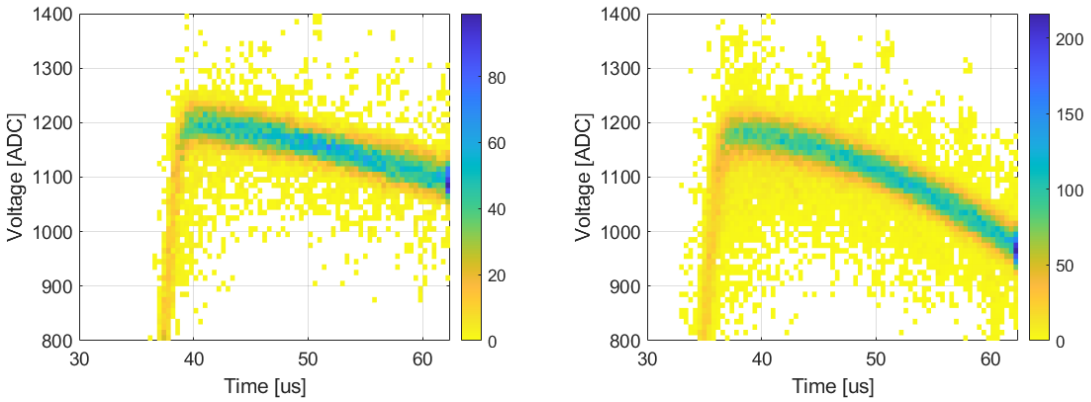

(a) 20°C **(b) 40°C**

Figure 6.45: Detector 168CS2(R) pixel waveform tails from an inner pixel (Ch 66) at -1000 V with a Cs-137 check source.

6.7 Conclusions

In many detectors, the "700 keV" dynamic range of the VAD-UMv2.2 ASIC can fail to record bulk events when the electron cloud-induced pixel signal is rising too slowly. Increasing the preamplifier feedback resistance increased the trigger shaping time and enabled more bulk events to meet the trigger threshold, but not at all depths of interaction, particularly near the planar cathode. The "3 MeV" dynamic range did not have a similar trigger problem with bulk events, so this ASIC was still usable in these experiments. However, the "700 keV" dynamic range may be preferred in the future when measuring spectra of low-energy photons. This ASIC is also limited in use with TlBr by its sampling window length and its loss of function with a 10 MHz master clock input, which is necessary for a 1.25 MHz sampling rate. A sampling rate of 1.25 MHz on the VAD-UMv2.2 ASIC is necessary to work with 1-cm-thick TlBr operating at a -1000 V bias.

The H3D S Series System is an effective commercial solution that can accommodate

TlBr detectors. Since they use the same VAD-UMv2.2 ASIC, but with an updated ASIC carrier board, they did not introduce any new problems to interaction event readout. Their spectroscopic ability and efficiency performed as expected.

The "double-peaking" phenomenon is due to the movement of extra electrons from events occurring in the pixel edges. Holes from those events are releasing trapped electrons. These electrons are contributing extra signal to pixel waveforms, which leads to the second photopeak or high-energy tailing in the energy spectra.

The cathode "pixel" pattern phenomenon is likely due to the migration of electrode material, pixel-bonding material, or bulk ions through the detector and then their reaction with the electrodes. This reaction is disintegrating "dot" shapes of the cathode that correlate with the anode pixel array. Different materials or electrode fabrication methods must be studied to prevent this migration. Carbon nanotube bonding appears to have longer stability but did not provide energy performance as good as another detector from the same section of the same ingot that was bonded with silver epoxy.

The H3DD-UM ASIC is currently better suited for use with TlBr than the VAD-UMv2.2 ASIC, due to it's longer sampling window and slower available sampling rate. It's slower trigger shaper setting also records more low-amplitude events, which helps to improve photopeak resolution.

Detector 168CS2(R) showed consistent performance across 0°C to +30°C, with an expected loss of signal due to temperature effects on the readout electronics. However, the detector showed an extra loss of signal and energy resolution at +40°C. These results were repeated twice over 11 days. Faster preamplifier decay at +40°C seems to have played some role in the signal loss.

Chapter 7

Conclusion

Thallium bromide continues to show potential as a room-temperature semiconductor gamma-ray and X-ray detector. Detectors with gold, chromium, and platinum electrodes showed the best energy resolution, but performance consistency was always a problem. The next critical step is to discover electrode and pixel bonding materials that will not react with or diffuse through the bulk. Both thallium electrodes and carbon nanotube paste bonding show promise in that area.

In addition to device fabrication, TlBr also needs readout electronics that are able to readout radiation interaction signals from the detector. The VAD-UMv2.2 ASIC is barely able to meet that need due to its narrow trigger shaping time adjustability and fast sampling clock. The H3DD-UMv4 ASIC with its slower trigger shaping time setting and longer sampling window make it better suited for lower-mobility materials like TlBr.

7.1 Future Work

Dr. Will Koehler's method to de-trap electrons and prevent high-energy tailing in TlBr by shining 3.1 eV photons on the detector should be repeated with the larger detectors used in this study.[52] He showed that this technique was somewhat repeatable so it would be beneficial to determine how much this could extend the good spectroscopic performance of a detector. This would also make transition to commercial readout systems simpler because it would make the shape of event waveforms more consistent.

As a part of discovering stable electrodes and bonding materials, it would be beneficial to apply for beam time at a synchrotron in order to determine if electrode materials

or other impurities are moving through the detectors to the opposite electrode. With thallium electrodes, I only tested after one device failure, but those electrodes should be tested for performance recovery through repeated failures.

The VAD-UMv2.2 ASIC should be investigated to enable its slowest designed sampling clock of 1.25 MHz if this ASIC is to continue to be used with lower-mobility materials like TlBr. It would also be helpful to investigate why its "700 keV" dynamic range had so many triggering issues, especially if TlBr is to be used to detect lower-energy photons like X rays. Specifically, the time between pulser injection and trigger threshold being exceeded should be measured at various threshold levels for both the "700 keV" and "3 MeV" dynamic ranges. This should produce enough data to reconstruct the shaped waveform and characterize the trigger shaper. The calculated time constant will confirm whether or not slower-rising waveforms can meet the trigger threshold. Alternatively, an external pulser that more closely matches a gamma-ray interaction waveform could be injected to the ASIC. Assuming the trigger shaper feedback setting is kept constant, the time constant should be the same at any dynamic range. If the time constant is found to vary with dynamic range or operating temperature, that would indicate a deeper issue in the ASIC. Solving these issues would make the current H3D S Series System a well-suited readout system to populate with large pixelated TlBr detectors. Additionally, the H3DD ASIC should also be tested at higher temperatures such as +40°C to see if it is affected.

Lastly, only single-pixel events were processed during this research. There is still a wealth of information to be mined from the multi-pixel event data. The low peak counts from higher energy gamma rays over 1 MeV would probably be bolstered by counts from multi-pixel events. At the very least, there is plenty of efficiency to be recovered from the multi-pixel event data, particularly at higher energies above 1 MeV.

Bibliography

[1] "Gamma-ray spectrometry catalog", Idaho National Laboratory. (1999), [Online]. Available: https://gammaray.inl.gov/SitePages/catalog_ge.aspx (visited on 06/24/2023).

[2] A. Gimelli, R. Liga, A. Giorgetti, D. Genovesi, and P. Marzullo, "Assessment of myocardial adrenergic innervation with a solid-state dedicated cardiac cadmium–zinc–telluride camera: First clinical experience", *European Heart Journal - Cardiovascular Imaging*, vol. 15, no. 5, pp. 575–585, Dec. 2013, ISSN: 2047-2404. DOI: 10.1093/ehjci/jet258.

[3] I. M. Szöghy and L. Kish, "Determination of radioactive disequilibrium in uranium-bearing rocks", *Canadian Journal of Earth Sciences*, vol. 15, no. 1, pp. 33–44, Jan. 1978, ISSN: 0008-4077. DOI: 10.1139/e78-003. [Online]. Available: https://cdnsciencepub-com.proxy.lib.umich.edu/doi/abs/10.1139/e78-003 (visited on 05/13/2023).

[4] R. Kouzes, J. Ely, B. Milbrath, J. Schweppe, E. Siciliano, and D. Stromswold, "Spectroscopic and non-spectroscopic radiation portal applications to border security", in *IEEE Nuclear Science Symposium Conference Record*, vol. 1, 2005, pp. 321–325. DOI: 10.1109/NSSMIC.2005.1596262.

[5] R. D. Evans, "The atomic nucleus", International series in pure and applied physics, 1955.

[6] NIST, *X-ray transition energies database: Thallium*, https://physics.nist.gov/cgi-bin/XrayTrans/search.html, 2005. (visited on 04/01/2024).

[7] R. Nurgalejev, S. Pohuliai, A. Sokolov, V. Gostilo, and J. Vanpaemel, "Spectrometric performance of a hpge semi-planar detector with large diameter", *Nuclear Instruments and Methods in Physics Research Section A: Accelerators, Spectrometers, Detectors and Associated Equipment*, vol. 985, p. 164 712, 2021, ISSN: 0168-9002. DOI: https://doi.org/10.1016/j.nima.2020.164712.

[8] G. F. Knoll, *Radiation detection and measurement*, 4th ed. John Wiley, 2010.

[9] E. Sakai, "Present status of room temperature semiconductor detectors", *Nuclear Instruments and Methods in Physics Research*, vol. 196, no. 1, pp. 121–130, 1982, ISSN: 0167-5087. DOI: 10.1016/0029-554X(82)90626-7.

[10] "H3d products", H3D, Inc. (2023), [Online]. Available: https://h3dgamma.com/home.php (visited on 07/11/2023).

[11] Y. Zhu and Z. He, "Performance of larger-volume 40 × 40 × 10- and 40 × 40 × 15-mm^3 cdznte detectors", *IEEE transactions on nuclear science*, vol. 68, no. 2, pp. 250–255, 2021. DOI: 10.1109/TNS.2021.3052133.

[12] D. McGregor and H. Hermon, "Room-temperature compound semiconductor radiation detectors", *Nuclear instruments & methods in physics research. Section A, Accelerators, spectrometers, detectors and associated equipment*, vol. 395, no. 1, pp. 101–124, 1997. DOI: 10.1016/S0168-9002(97)00620-7.

[13] M. Schieber, J. Lund, R. Olsen, D. McGregor, J. Van Scyoc, R. James, E. Soria, and E. Bauser, "Material properties and room-temperature nuclear detector response of wide bandgap semiconductors", *Nuclear instruments & methods in physics research. Section A, Accelerators, spectrometers, detectors and associated equipment*, vol. 377, no. 2, pp. 492–495, 1996. DOI: 10.1016/0168-9002(96)00030-7.

[14] K. Kim, J. Suh, A. Bolotnikov, P. Fochuk, O. Kopach, G. Camarda, Y. Cui, A. Hossain, G. Yang, J. Hong, and R. James, "Temperature-gradient annealing of cdznte under te overpressure", *Journal of Crystal Growth*, vol. 354, no. 1, pp. 62–66, 2012. DOI: 10.1016/j.jcrysgro.2012.03.058.

[15] P. Luke, "Unipolar charge sensing with coplanar electrodes-application to semiconductor detectors", *IEEE Transactions on Nuclear Science*, vol. 42, no. 4, pp. 207–213, 1995. DOI: 10.1109/23.467848.

[16] H. Kim, A. Churilov, G. Ciampi, L. Cirignano, W. Higgins, S. Kim, P. O'Dougherty, F. Olschner, and K. Shah, "Continued development of thallium bromide and related compounds for gamma-ray spectrometers", *Nuclear instruments & methods in physics research. Section A, Accelerators, spectrometers, detectors and associated equipment*, vol. 629, no. 1, pp. 192–196, 2011. DOI: 10.1016/j.nima.2010.10.097.

[17] H. Kim, L. Cirignano, J. F. Christian, A. Kargar, Y. Ogorodnik, S. Kim, M. Breen, M. R. Squillante, and K. Shah, "Improved performance and longevity of large volume thallium bromide devices", in *Proceedings in SPIE, Hard X-Ray, Gamma-Ray, and Neutron Detector Physics XXIV*, vol. 12241, SPIE, 2022, pp. 1224106-1224106–8. DOI: 10.1117/12.2635925.

[18] K. Hitomi, T. Murayama, T. Shoji, T. Suehiro, and Y. Hiratate, "Improved spectrometric characteristics of thallium bromide nuclear radiation detectors", *Nuclear instruments & methods in physics research. Section A, Accelerators, spectrometers, detectors and associated equipment*, vol. 428, no. 2, pp. 372–378, 1999. DOI: 10.1016/S0168-9002(99)00141-2.

[19] K. Shah, J. Lund, F. Olschner, L. Moy, and M. Squillante, "Thallium bromide radiation detectors", *IEEE transactions on nuclear science*, vol. 36, no. 1, pp. 199–202, 1989. DOI: 10.1109/23.34434.

[20] "X-ray mass attenuation coefficients", National Institute of Standards and Technology. (2004), [Online]. Available: https://www.nist.gov/pml/x-ray-mass-attenuation-coefficients (visited on 08/22/2023).

[21] A. V. Churilov, G. Ciampi, H. Kim, W. M. Higgins, L. J. Cirignano, F. Olschner, V. Biteman, M. Minchello, and K. S. Shah, "Tlbr and $\mathrm{tlbr}_x\mathrm{i}_{1-x}$ crystals for γ-ray detectors", *Journal of Crystal Growth*, vol. 312, no. 8, pp. 1221–1227, 2010. DOI: 10.1016/j.jcrysgro.2009.10.055.

[22] K. Suzuki, M. Shorohov, T. Sawada, and S. Seto, "Time-of-flight measurements on tlbr detectors", *IEEE transactions on nuclear science*, vol. 62, no. 2, pp. 433–436, DOI: 10.1109/TNS.2015.2403279.

[23] K. Hitomi, M. Matsumoto, O. Muroi, T. Shoji, and Y. Hiratate, "Characterization of thallium bromide crystals for radiation detector applications", *Journal of crystal growth*, vol. 225, no. 2–4, pp. 129–133, 2001. DOI: 10.1016/S0022-0248(01)00834-X.

[24] J. Christian and H. Kim, Personal communication, Dec. 2023.

[25] C. C. Stoumpos and M. G. Kanatzidis, "The renaissance of halide perovskites and their evolution as emerging semiconductors", *Accounts of chemical research*, vol. 48, no. 10, pp. 2791–2802, 2015. DOI: 10.1021/acs.accounts.5b00229.

[26] C. C. Stoumpos, C. D. Malliakas, J. A. Peters, Z. Liu, M. Sebastian, J. Im, T. C. Chasapis, A. C. Wibowo, D. Y. Chung, A. J. Freeman, B. W. Wessels, and M. G. Kanatzidis, "Crystal growth of the perovskite semiconductor cspbbr3: A new material for high-energy radiation detection", *Crystal Growth & Design*, vol. 13, no. 7, pp. 2722–2727, 2013. DOI: 10.1021/cg400645t.

[27] Y. He, M. Petryk, Z. Liu, D. G. Chica, I. Hadar, C. Leak, W. Ke, I. Spanopoulos, W. Lin, D. Y. Chung, B. W. Wessels, Z. He, and M. G. Kanatzidis, "Cspbbr_3 perovskite detectors with 1.4% energy resolution for high-energy γ-rays", *Nature photonics*, vol. 15, no. 1, pp. 36–42, 2021. DOI: 10.1038/s41566-020-00727-1.

[28] Z. Liu, J. A. Peters, C. C. Stoumpos, M. Sebastian, B. W. Wessels, J. Im, A. J. Freeman, and M. G. Kanatzidis, "Heavy metal ternary halides for room-temperature x-ray and gamma-ray detection", in *Proceedings in SPIE, Hard X-Ray, Gamma-Ray, and Neutron Detector Physics XV*, vol. 8852, SPIE, 2013, 88520A-88520A–7. DOI: 10.1117/12.2022877.

[29] Y. He, Z. Liu, K. M. McCall, W. Lin, D. Y. Chung, B. W. Wessels, and M. G. Kanatzidis, "Perovskite cspbbr$_3$ single crystal detector for alpha-particle spectroscopy", *Nuclear instruments & methods in physics research. Section A, Accelerators, spectrometers, detectors and associated equipment*, vol. 922, pp. 217–221, 2019. DOI: 10.1016/j.nima.2019.01.008.

[30] M. Streicher, Personal communication, Dec. 2023.

[31] L. Pan, Y. Feng, P. Kandlakunta, J. Huang, and L. R. Cao, "Performance of perovskite cspbbr3 single crystal detector for gamma-ray detection", *IEEE transactions on nuclear science*, vol. 67, no. 2, pp. 443–449, 2020. DOI: 10.1109/TNS.2020.2964306.

[32] R. Hofstadter, "Thallium halide crystal counter", *Physical review*, vol. 72, no. 11, pp. 1120–1121, 1947. DOI: 10.1103/PhysRev.72.1120.

[33] Ijaz-ur-Rahman and R. Hofstadter, "Thallium halide radiation detectors", *Physical review. B, Condensed matter*, vol. 29, no. 6, pp. 3500–3507, 1984. DOI: 10.1103/PhysRevB.29.3500.

[34] K. Takagi, K. Toyoda, H. Kase, T. Takagi, K. Tabata, T. Terao, H. Morii, A. Koike, T. Aoki, M. Nogami, and K. Hitomi, "Bias polarity switching-type tlbr x-ray imager", *IEEE Transactions on Nuclear Science*, vol. 68, no. 9, pp. 2435–2439, 2021. DOI: 10.1109/TNS.2021.3078448.

[35] E. Vernon, G. De Geronimo, A. Bolotnikov, M. Stanacevic, J. Fried, L. O. Giraldo, G. Smith, K. Wolniewicz, K. Ackley, C. Salwen, J. Triolo, D. Pinelli, and K. Luong, "Front-end asic for spectroscopic readout of virtual frisch-grid czt bar sensors", *Nuclear instruments & methods in physics research. Section A, Accelerators, spectrometers, detectors and associated equipment*, vol. 940, no. C, pp. 1–11, 2019. DOI: 10.1016/j.nima.2019.05.047.

[36] Y. Zhu and Z. He, "Performance of a 2-kev digitizer asic for 3-d position-sensitive pixellated semiconductor detectors", in *2012 IEEE Nuclear Science Symposium and Medical Imaging Conference Record (NSS/MIC)*, 2012, pp. 4109–4112. DOI: 10.1109/NSSMIC.2012.6551939.

[37] G. De Geronimo, E. Vernon, K. Ackley, A. Dragone, J. Fried, P. O'Connor, Z. He, C. Herman, and F. Zhang, "Readout asic for 3d position-sensitive detectors", *IEEE transactions on nuclear science*, vol. 55, no. 3, pp. 1593–1603, 2008. DOI: 10.1109/TNS.2008.922217.

[38] Z. He, "Review of the shockley–ramo theorem and its application in semiconductor gamma-ray detectors", *Nuclear instruments & methods in physics research. Section A, Accelerators, spectrometers, detectors and associated equipment*, vol. 463, no. 1, pp. 250–267, 2001. DOI: 10.1016/S0168-9002(01)00223-6.

[39] Z. He, G. Knoll, and D. Wehe, "Direct measurement of electron drift parameters of wide band gap semiconductors", *Nuclear instruments & methods in physics research. Section A, Accelerators, spectrometers, detectors and associated equipment*, vol. 411, no. 1, pp. 114–120, 1998. DOI: 10.1016/S0168-9002(98)00299-X.

[40] V. M. Gerrish, "Chapter 13 - characterization and quantification of detector performance", in *Semiconductors and Semimetals*, ser. Semiconductors and Semimetals, T. Schlesinger and R. B. James, Eds., vol. 43, Elsevier, 1995, pp. 493–530. DOI: 10.1016/S0080-8784(08)62752-0.

[41] "Ev-509x preamplifiers", Kromek. (2018), [Online]. Available: https://www.kromek.com/filedownload/2128/ (visited on 07/26/2023).

[42] F. Zhang, Z. He, D. Xu, G. Knoll, D. Wehe, and J. Berry, "Improved resolution for 3d position sensitive cdznte spectrometers", in *2003 IEEE Nuclear Science Symposium. Conference Record (IEEE Cat. No.03CH37515)*, vol. 5, IEEE, 2003, 3356–3360 Vol.5. DOI: 10.1109/NSSMIC.2003.1352625.

[43] Y. Zhu, "Digital signal processing methods for pixelated 3-d position sensitive room-temperature semiconductor detectors", Ph.D. dissertation, University of Michigan, 2012.

[44] Z. He, W. Li, G. Knoll, D. Wehe, J. Berry, and C. Stahle, "3-d position sensitive cdznte gamma-ray spectrometers", *Nuclear instruments & methods in physics research. Section A, Accelerators, spectrometers, detectors and associated equipment*, vol. 422, no. 1, pp. 173–178, 1999. DOI: 10.1016/S0168-9002(98)00950-4.

[45] Y. Zhu, S. E. Anderson, and Z. He, "Sub-pixel position sensing for pixelated, 3-d position sensitive, wide band-gap, semiconductor, gamma-ray detectors", *IEEE transactions on nuclear science*, vol. 58, no. 3, pp. 1400–1409, 2011. DOI: 10.1109/TNS.2011.2132738.

[46] K. Hitomi, Y. Kikuchi, T. Shoji, and K. Ishii, "Improvement of energy resolutions in tlbr detectors", *Nuclear instruments & methods in physics research. Section A, Accelerators, spectrometers, detectors and associated equipment*, vol. 607, no. 1, pp. 112–115, 2009. DOI: 10.1016/j.nima.2009.03.129.

[47] C. Leak, "Techniques for pixelated ambipolar-sensitive semiconductor gamma-ray spectrometers", Ph.D. dissertation, University of Michigan, 2021.

[48] K. Hitomi, T. Shoji, and Y. Niizeki, "A method for suppressing polarization phenomena in tlbr detectors", *Nuclear instruments & methods in physics research. Section A, Accelerators, spectrometers, detectors and associated equipment*, vol. 585, no. 1, pp. 102–104, 2008. DOI: 10.1016/j.nima.2007.11.012.

[49] A. Datta, J. Fiala, P. Becla, and S. Motakef, "Stable room-temperature thallium bromide semiconductor radiation detectors", *APL materials*, vol. 5, no. 10, pp. 106109-106109–7, 2017. DOI: 10.1063/1.5001181.

[50] K. H. Kim, E. Kim, H. Kim, R. Tappero, A. E. Bolotnikov, G. S. Camarda, A. Hossain, L. Cirignano, and R. B. James, "Electro-migration of impurities in TlBr", *Journal of Applied Physics*, vol. 114, no. 13, p. 133 701, Oct. 2013, ISSN: 0021-8979. DOI: 10.1063/1.4823781. eprint: https://pubs.aip.org/aip/jap/article-pdf/doi/10.1063/1.4823781/13354562/133701_1_online.pdf. [Online]. Available: https://doi.org/10.1063/1.4823781.

[51] R. Hussain, S. Mirza, and N. Mirza, "The study of response of wide band gap semiconductor detectors using the geant4", *Nuclear technology & radiation protection*, vol. 29, no. 3, pp. 242–248, 2014. DOI: 10.2298/NTRP1403242H.

[52] W. Koehler, "Thallium bromide as an alternative material for room-temperature gamma-ray spectroscopy and imaging", Ph.D. dissertation, University of Michigan, 2016.

[53] T. Shoji, K. Hitomi, O. Muroi, T. Suehiro, and Y. Hiratate, "Temperature characteristics of the radiation detector using the tlbr crystals", *IEEE transactions on nuclear science*, vol. 46, no. 6, pp. 1934–1937, 1999. DOI: 10.1109/23.819257.

[54] P. Kostamo, M. Shorohov, V. Gostilo, H. Sipilä, V. Kozlov, I. Lisitsky, M. Kuznetsov, A. Lankinen, A. Danilewsky, H. Lipsanen, and M. Leskelä, *Characterization of tlbr for x-ray and -ray detector applications*, 2009. DOI: 10.1016/j.nima.2009.03.125.

[55] F. Eduardo da Costa, C. Henrique de Mesquita, and M. M. Hamada, "Temperature dependence in the long-term stability of the tlbr detector", *IEEE Transactions on Nuclear Science*, vol. 56, no. 4, pp. 1817–1822, 2009. DOI: 10.1109/TNS.2009.2024678.

[56] B. Dönmez, C. L. Thrall, Z. He, L. J. Cirignano, H. Kim, and K. S. Shah, "Investigation of polarization effect with tlbr detectors at different operating temperatures", in *IEEE Nuclear Science Symposuim & Medical Imaging Conference*, 2010, pp. 3773–3775. DOI: 10.1109/NSSMIC.2010.5874517.

[57] J. Xia, Y. Zhu, and Z. He, "Efficient temperature corrections for gamma-ray energy reconstruction in 3-d position-sensitive cdznte detectors", *Nuclear instruments & methods in physics research. Section A, Accelerators, spectrometers, detectors and associated equipment*, vol. 954, pp. 161 340–, 2020. DOI: 10.1016/j.nima.2018.10.018.